To the Graduate Council:

I am submitting herewith a dissertation written by Samuel A. Lowry entitled "A Numerical Model of Convective Effects in Diffusion Dominated Directional Solidification of a Metal Analogue (NH_4Cl-H_2O) at One Gravity and Microgravity." I have examined the final copy of this dissertation for form and content and recommend that it be accepted in partial fulfillment of the requirements for the degree of Doctor of Philosophy, with a major in Engineering Science.

T. Dwayne McCay, Major Professor

We have read this dissertation
and recommend its acceptance:

Accepted for the Council:

Vice Provost
and Dean of the Graduate School

A NUMERICAL MODEL OF CONVECTIVE EFFECTS IN DIFFUSION DOMINATED DIRECTIONAL SOLIDIFICATION OF A METAL ANALOGUE (NH_4Cl-H_2O) AT ONE GRAVITY AND MICROGRAVITY

A Dissertation

Presented for the

Doctor of Philosophy

Degree

The University of Tennessee, Knoxville

SAMUEL A. LOWRY

May 1991

ACKNOWLEDGEMENTS

I would like to thank those who helped in one way or another in the preparation of this dissertation. They include Dr. Laurence Keeton, Dr. Andrzej Przekwas, and Dr. Ashok Singhal for my introduction to Computational Fluid Dynamics and for their friendly advice over the years; Linda Williams for making the typed results look professional; and my coworkers Perry Gray, John Hopkins, and Mary Yesko for their camaraderie and technical support. In particular, I would like to thank John for access to his experimental data and for numerous helpful discussions.

I would like to express special appreciation to Dr. T. Dwayne McCay and Dr. Mary Helen McCay for encouraging me to pursue a doctoral degree, for providing the opportunity to be associated with the CAST project, and for their guidance in my research.

Finally, I would like to thank my wife, Kay, for her patience and understanding while I was in graduate school.

ABSTRACT

A numerical model is developed to simulate the directional solidification of a dendritic metal analogue material, ammonium chloride and water, in support of a planned series of microgravity experiments. The model is first validated by comparison with ground-based data. Undercooling (non-equilibrium) effects are shown to be significant. The one-gravity computations correlate well with the ground-based data for the initial diffusion limited growth and the transition to dominant convective flows at a critical solutal and thermal Rayleigh number. The model is then used to predict the directional dendritic solidification for a sample low gravity run and the results are compared with one-gravity data.

TABLE OF CONTENTS

LIST OF FIGURES

LIST OF TABLES

NOMENCLATURE

A	one of two components in a binary alloy
A_E	east link coefficient
A_N	north link coefficient
A_P	cell coefficient
A_S	south link coefficient
A_W	west link coefficient
b	collective source term
B	one of two components in a binary alloy
B_x	body force in the x direction
C	composition (wt%)
CR	cooling rate $\left(\frac{^\circ C}{min}\right)$
C_e	composition at the eutectic point (wt%)
C_l	liquid concentration (wt%)
C_0	reference composition (wt%)
C_p	specific heat $\left(\frac{erg}{gm \cdot ^\circ C}\right)$
C_s	solid concentration (wt%)
d	velocity correction coefficient $\left(\frac{cm^3}{dynes-sec}\right)$
D	diffusive flux coefficient
D	solutal diffusion coefficient $\left(\frac{cm^2}{sec}\right)$
F	modified mass flux
Flux	mass flux $\left(\frac{gm}{sec}\right)$
G	temperature gradient (°C/cm)
g	acceleration of gravity $\left(\frac{cm}{sec^2}\right)$
g_l	liquid volume fraction

h	enthalpy $\left(\frac{\text{ergs}}{\text{gm}}\right)$
J	net flux (e.g., of energy or solute)
K	permeability (cm^2)
k_p	partition coefficient
k	thermal conductivity $\left(\frac{\text{erg}}{\text{cm}\cdot\text{sec}\cdot^\circ\text{C}}\right)$
k_q	thermal conductivity of quartz $\left(\frac{\text{erg}}{\text{cm}\cdot\text{sec}\cdot^\circ\text{C}}\right)$
L	latent heat $\left(\frac{\text{ergs}}{\text{gm}}\right)$
P	pressure $\left(\frac{\text{dyne}}{\text{cm}^2}\right)$
P^*	pressure estimate $\left(\frac{\text{dyne}}{\text{cm}^2}\right)$
P'	pressure correction $\left(\frac{\text{dyne}}{\text{cm}^2}\right)$
Pe	local Peclet number $\left(\frac{u\cdot\Delta x}{\Gamma}\right)$
P_r	Prandtl number $\left(\frac{\nu}{\alpha_T}\right)$
q	thermal flux $\left(\frac{\text{cal}}{\text{cm}\cdot\text{sec}}\right)$
q_l	thermal flux in liquid $\left(\frac{\text{cal}}{\text{cm}\cdot\text{sec}}\right)$
q_q	thermal flux in quartz $\left(\frac{\text{cal}}{\text{cm}\cdot\text{sec}}\right)$
Ra	combined Rayleigh number ($Ra_S + Ra_T$)
Ra_S	solutal Rayleigh number
Ra_T	thermal Rayleigh number
S	source of ϕ per volume
S_c	constant source of ϕ per control cell
S_c	Schmidt number $\left(\frac{\nu}{\alpha_S}\right)$
S_p	source term coefficient for $S_\phi = S_p\phi + S_c$
T	temperature (°C)
T_0	reference temperature (°C)
T_e	eutectic temperature (°C)
T_m	melting temperature (°C)

t	time (sec)
u_l	liquid velocity in the horizontal (x) direction (cm/sec)
u_s	solid velocity in the horizontal (x) direction (cm/sec)
u	effective liquid velocity ($u = u_l \cdot g_l$) in the horizontal (x) direction (cm/sec)
$\bar{u}$	average velocity $\left(\bar{u} = \frac{1}{\rho}\left(\bar{\rho}_l u_l + \bar{\rho}_s u_s\right)\right)$ in the horizontal (x) direction (cm/sec)
$\widehat{u}$	psuedo-velocity in the horizontal (x) direction (cm/sec)
v_l	liquid velocity in the vertical (y) direction (cm/sec)
v_s	solid velocity in the vertical (y) direction (cm/sec)
v	effective liquid velocity ($v = v_l \cdot g_l$) in the vertical (y) direction (cm/sec)
$\bar{v}$	average velocity $\left(\bar{v} = \frac{1}{\rho}\left(\bar{\rho}_l v_l + \bar{\rho}_s v_s\right)\right)$ in the vertical (y) direction (cm/sec)
$\widehat{v}$	psuedo-velocity in the vertical (y) direction (cm/sec)
$\vec{V}_l$	liquid velocity vector (cm/sec)
$\vec{V}_s$	solid velocity vector (cm/sec)
$\bar{V}$	average velocity vector $\left(\bar{V} = \frac{1}{\rho}\left(\bar{\rho}_l \vec{V}_l + \bar{\rho}_s \vec{V}_s\right)\right)$ (cm/sec)

Greek Symbols

α	denotes the A rich phase in a phase diagram
α_S	solutal diffusivity $\left(\frac{\text{cm}^2}{\text{sec}}\right)$
α_T	thermal diffusivity $\left(\frac{\text{cm}^2}{\text{sec}}\right)$
β	denotes the B rich phase in a phase diagram
β_S	solutal coefficient of volumetric expansion $\left(\frac{1}{\text{wt\%}}\right)$
β_T	thermal coefficient of volumetric expansion $\left(\frac{1}{^\circ\text{C}}\right)$
δx	horizontal distance between cell nodes (cm)

δy	vertical distance between cell nodes (cm)
Δx	horizontal distance between cell faces (cm)
Δy	vertical distance between cell faces (cm)
Δt	numerical time step interval (sec)
ϕ	generalized conserved quantity
Γ	generalized diffusion coefficient
ρ	average mass density of the mixture $\left(\frac{\text{gm}}{\text{cm}^3}\right)$
ρ_k	mass density of the k phase $\left(\frac{\text{gm}}{\text{cm}^3}\right)$
$\bar{\rho}_k$	partial mass density of the k phase $\left(\frac{\text{gm}}{\text{cm}^3}\right)$
ρ_o	mass density of reference bulk fluid $\left(\frac{\text{gm}}{\text{cm}^3}\right)$
ν	kinematic viscosity $\left(\frac{\text{cm}^2}{\text{sec}}\right)$

Subscripts

e	pertaining to the control volume east face
E	pertaining to the node of the control volume to the east
j	horizontal (x) index for the control cells
k	vertical (y) index for the control cells
l	liquid
n	pertaining to the control volume north face
N	pertaining to the node of the control volume to the north
P	pertaining to the node of current control volume
s	solid
s	pertaining to the control volume south face
S	pertaining to the node of the control volume to the south
0	reference value
q	quartz
w	pertaining to the control volume west face

W	pertaining to the node of the control volume to the west
o	previous time step value
$*$	latest estimate
$*-1$	previous estimate
$'$	correction

SECTION I

INTRODUCTION

At a recent international symposium on heat and mass transfer in manufacturing and materials processing, a number of authors stressed the need for close cooperation between experimentalists and numerical modelers in the effort to investigate and understand the complex phenomena involved in the science of materials processing.[1] The objective of this dissertation research is to develop an advanced numerical fluids and thermal model (FTM) to provide that degree of close support for a series of experiments on the unidirectional dendritic solidification of binary alloys.

The experiments being supported are a series of space and ground-based studies being conducted under the Casting and Solidification Technology (CAST) project.[2-9] The experiments are designed to study the development of the solutal distribution in a solidifying binary dendritic system. The solidification of binary systems is of interest because it is integral to a wide range of important processes such as casting. The need to understand and control solutal distribution during the solidification of a binary or multicomponent system is vital because of its direct effect on segregation of solute and the quality of the final product.[10]

The fluids and thermal model (FTM) developed here combines recent advances in computational techniques and multicomponent conservation equations to model the CAST unidirectional ground-based and space experiments. The purpose of the FTM is to accurately model the existing ground-based studies during the stages of growth for which diffusion is the dominant transport mechanism, and to provide predictions for the planned microgravity experiments.

The basic configuration of the simulated experiments is shown in Fig. I–1. The experiments use a binary solution, the metal analogue ammonium chloride and water. In a typical ground-based run, a 28 wt% NH_4Cl - 72 wt% H_2O solution is solidified vertically by imposing a positive thermal gradient on the quartz cuvette and then lowering the cuvette temperature at a controlled rate. As the solidification progresses, solute, less dense than the bulk liquid for this solution, is rejected by the newly formed dendritic solid and a density inversion develops in and above the solid-liquid (dendritic) region at the bottom of the cuvette. Under one-gravity conditions, this inversion leads to the onset of disruptive convective flows.

In this research, the FTM was developed and then validated using three selected ground-based unidirectional solidification experiments. For either one-gravity or microgravity conditions, the FTM calculates the flow field, the growth of the two-phase dendritic region, the temperature distribution, the solutal distribution, and the corresponding density field. In addition, for the ground run comparisons, the model determines the conditions pertinent to convective breakdown, in particular the time and critical Rayleigh number associated with the transition from diffusion to convection dominated solidification. The ground-based runs, complicated by the effects of one-gravity convection, are more difficult to numerically simulate than the microgravity spaceflight experiments and provide a strenuous validation test for the model.

Once the FTM is validated by comparison with ground-based results, it is then used to predict run conditions for the CAST microgravity experiment. The one-gravity and microgravity cases are compared and the differences discussed.

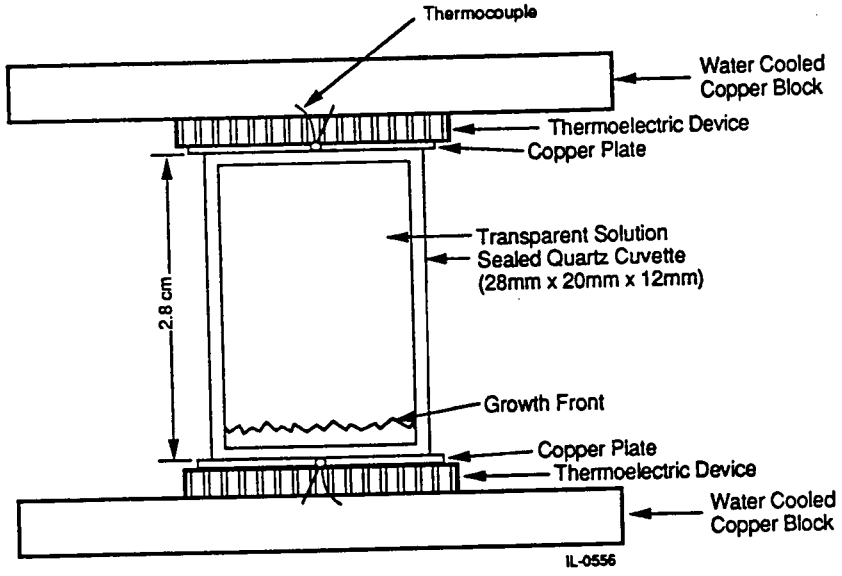

Figure I–1. Schematic of CAST cuvette and solidification assembly

SECTION II

BACKGROUND

The purpose of this section is to provide an introduction to the dendritic solidification of binary materials including the mechanisms of heat and mass transport inherent in the solidification process. This is followed by a limited review of previous solidification experiments on binary dendritic materials and past analytical and numerical modeling efforts.

Fundamentals of Binary Dendritic Solidification

Binary Alloy Solidification

A binary material is composed of two components, A and B, such as Pb-Sn, Al-Cu, and NH_4Cl-H_2O. Each component may contain multiple elements but must maintain its integrity when combined with the other component. A sample binary phase diagram is shown in Fig. II–1.

The solutal concentrations of the solid and liquid in equilibrium at a given temperature are denoted by the intersection of a constant temperature line with the solidus and liquidus lines. Between the liquidus and solidus, solid and liquid coexist over a range of temperatures creating a two-phase region. The liquidus indicates the temperature at which solidification begins for a given liquid concentration. Variation in the liquid concentration during solidification produces variation in the solid. This solutal variation can be either on the scale of the growth structure, referred to as microsegregation, or on a larger scale referred to as macrosegregation.[10]

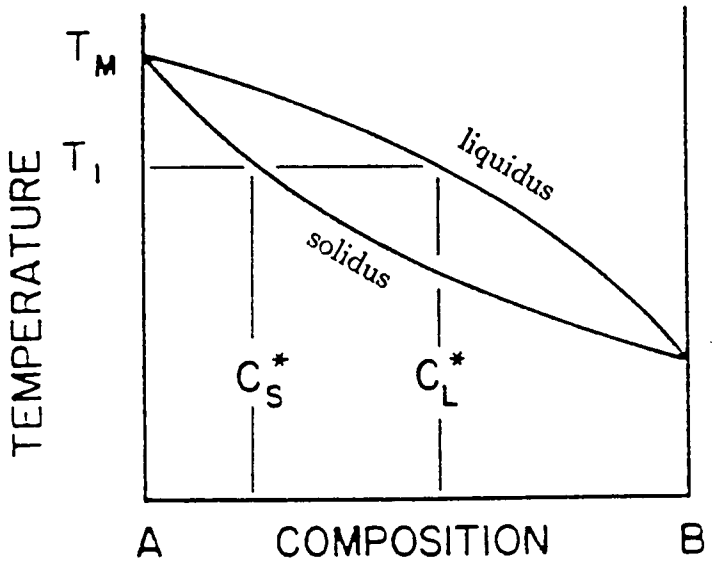

Figure II–1. Sample binary phase diagram (From Flemings[10])

Morphology

A binary material solidifies with either a faceted or non-faceted interface. The parameter that indicates whether or not the interface will be faceted is the dimensionless entropy of fusion,[11] $\alpha = \frac{\Delta S_f}{R}$ where R is the universal gas constant and ΔS_f is the entropy of fusion. Materials with an α less than two tend to be non-faceted. Metals typically fall into this category.[12]

A non-faceted interface can be planar or non-planar depending on the material properties and the growth conditions. A simplified condition for planar stability of binary materials is the constitutional supercooling criterion,[13] i.e. the temperature

gradient at the interface must be sufficiently large to prevent undercooling due to concentration effects. This criterion can be expanded to include the effects of surface energy using linear stability analysis,[14] giving the following condition for planar stability,

$$G \geq \frac{V \cdot \Delta T_0}{D} - \frac{\Gamma \cdot k \cdot V^2}{D^2},$$

where G is the temperature gradient at the interface, V is the interface growth velocity, ΔT_0 the temperature difference between the solidus and liquidus, k the partition coefficient, D the diffusivity, and Γ the specific interface energy divided by the entropy of fusion.[12] Inspection of the above equation reveals that at low growth rates the solutal, (V/D), term is reduced, tending to stabilize the interface for a given temperature gradient. At the other extreme of high growth velocities, (on the order of 1 cm/sec for typical metals),[10] the surface energy term becomes sufficient to stabilize the interface. The category of solidification addressed in this study is for those materials and growth rates, e.g., the casting of metals, that typically fall between these two extremes with the result that the solid-liquid interface is dendritic. The NH_4Cl-H_2O analogue material used in the CAST studies solidifies dendritically as shown in Fig. II–2.

Metal Model NH_4Cl-H_2O

The use of transparent compounds to model the freezing of metals was first suggested by Jackson and Hunt[15] based on the dimensionless entropy of formation $\alpha = \Delta S/R$. One such compound, aqueous ammonium chloride, was used by Jackson and coworkers[16] in studying the equiaxed zone in castings. It has since been used extensively, including the current CAST studies. The ammonium chloride and water phase diagram is provided in Fig. II–3.

Figure II–2. Ammonium chloride and water dendrites (Courtesy McCay)

Transparent metal analogue compounds, such as NH_4Cl-H_2O, offer several advantages and some limitations in the investigation of metallic solidification. The primary advantage of these compounds is that they are transparent and thus lend themselves to flow visualization. Ammonium chloride and water has the particular advantage that it can be used to mimic the density characteristics of several important alloys. This is accomplished by using a bulk fluid water concentration that is less than the eutectic value (80.4 wt% water), such that the solute rejected during solidification is lighter than the bulk liquid.[17] Since buoyancy driven flows depend directly on the density distribution, this similarity to an actual alloy is critical.

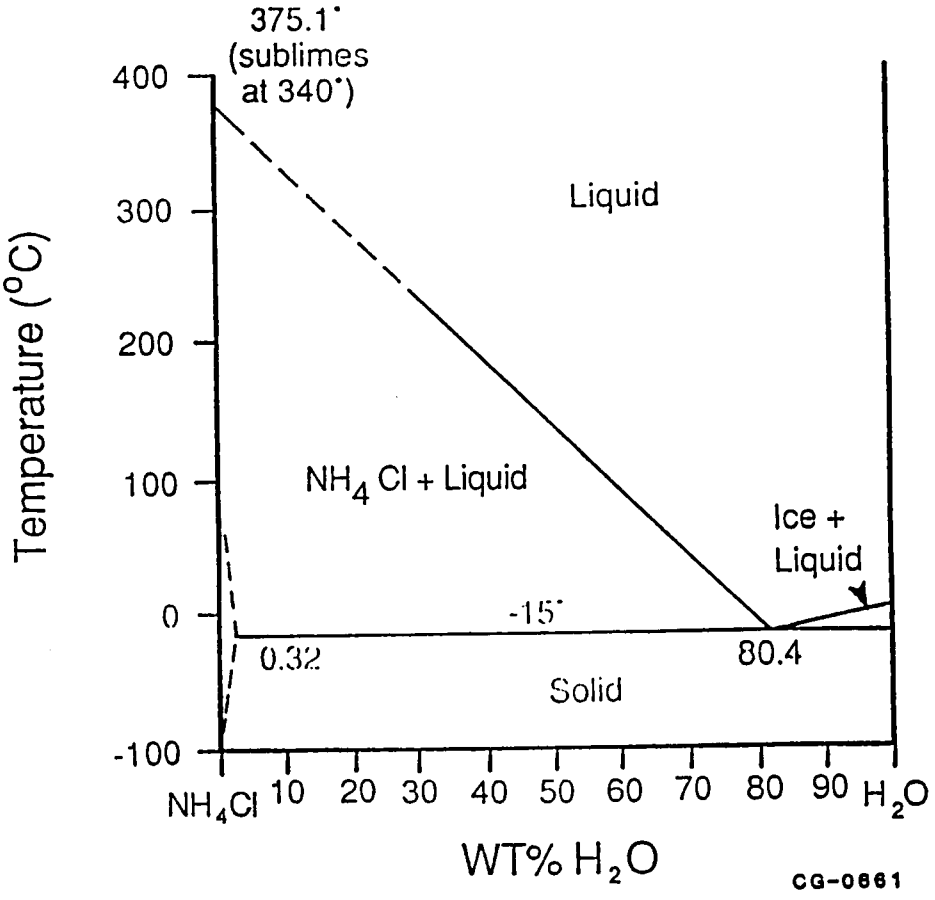

Figure II-3. Ammonium chloride and water phase diagram

Ammonium chloride and water also has the advantages that it is non-toxic, solidifies near room temperature, and its properties are relatively well known. Gray[4] has compiled many of these properties for aqueous ammonium chloride from available sources. In addition, McCay and colleagues have measured the surface tension variation with temperature and concentration,[19] the partition coefficient,[5] and the index of refraction variation with temperature and concentration.[20] How these properties are incorporated into the numerical model will be discussed in the section on modeling.

One limitation of ammonium chloride and water as a metal analogue is that, relative to metals, it has a low conductivity. Its Lewis number, the ratio of solutal diffusivity to the thermal diffusivity, is 0.015 which is an order of magnitude larger than for a typical metal.[18] This means that solutal effects are more important in ammonium chloride and water than in metals, and direct extrapolations to metal systems must be made carefully.

Thermal Diffusion

The solidification of any material necessarily involves extracting the heat of fusion released during the process. This extraction can either be in the direction of growth, i.e. through the liquid ahead of the growth front, or opposite to the direction of growth, i.e. through the solid or mushy zone behind the growth front. Heat extraction through the liquid implies the liquid is undercooled. This occurs, for example, when isolated nuclei grow in undercooled regions produced at the walls of a casting.[10] Heat extraction through the solid or mushy zone implies that the solid material is being cooled below the local freezing point. The liquid ahead of the solidification front may or may not be undercooled. The extraction of heat through the solid or mushy zone exists in a number of processes such as Czochralski growth, Bridgman growth, float zone solidification, directional solidification of turbine blades, and in the columnar region of a casting.[12] In the CAST experiments, the latent heat is extracted through the two-phase region in the direction opposite to that of the solidification. Hence, the CAST experiments model the type of heat flow found in the unidirectional solidification of turbine blades and the columnar dendritic growth region of castings.

Solutal Diffusion

In addition to thermal diffusion, the solidification process for most binary materials involves diffusion of solute. Except in special cases, such as eutectic solidification and congruent transformations where the solid has the same concentration as the liquid, the transition from liquid to solid results in either a buildup or depletion of solute at the growth front. The resulting solutal gradients drive diffusive fluxes. Over short distances or in the case of minimal convection, these diffusive fluxes can be the dominant means of solute transport.

Convective Flow

Fluid motion or convection during dendritic solidification is often a major means of heat and mass transport and has been shown to influence the structure and quality of the final product in a number of ways. For example, convection in the form of rising columns of solute enriched fluid has been shown to be the cause of an undesirable type of macrosegregation phenomenon known as 'freckles.'[21] Convective flow has also been found to affect the shape of individual dendrites.[22] Fluid motion can also effect the structure of a material by convecting nucleation sites during solidification. Jackson et al.[16] have postulated that the equiaxed structure in the central regions of a casting develop from fragments of dendrite arms that have been convected into the undercooled region. As another example of the importance of convection, McDonald and Hunt[24,25] have demonstrated that 'A' type segregation found in steel castings can be eliminated by using dopants to alter the density characteristics of the material, thereby suppressing buoyancy driven convection.

In general, convection during solidification influences both the solutal and thermal distributions. The possible causes of convection are numerous. Even in

a relatively simple growth configuration, such as the unidirectional CAST experiment, there are six distinct mechanisms for generating flows during solidification. Each is discussed briefly in the following, with emphasis on flows significant to microgravity solidification.

Residual Flow Any flows that were created in the liquid due to a previous event such as stirring, sloshing, pouring, rotation, etc., may persist and still be present at the onset of solidification. Such residual flows are always of concern in the laboratory, and are of particular concern, for example, for short duration microgravity experiments flown on aircraft[6] and sounding rockets.[26]

Surface Tension Driven Flow Another type of flow that may dominate in the microgravity environment is surface tension driven flow. This flow originates at fluid-fluid interfaces (free surfaces) due to gradients in the surface tension caused by solutal or thermal variations. The dimensionless parameter that indicates the magnitude of the surface tension effects relative to the viscous forces is the Marangoni number, defined here for the thermal case as

$$Ma = \frac{\sigma(\delta\sigma/\delta T)L}{\rho\nu^2}\Delta T$$

where σ is the surface tension, $\delta\sigma/\delta T$ the variation of surface tension with temperature, L the characteristic length scale, ρ the density, ν the kinematic viscosity, and ΔT the temperature difference acting over L. Similarly, the modified Bond number, indicates the magnitude of surface tension effects relative to buoyancy effects, i.e.:

$$Bo = \frac{\rho g \beta_T L^2}{(\delta\sigma/\delta T)}$$

where g is the local gravity and β_T the thermal coefficient of expansion.[27] These parameters express the relative importance of surface tension flows in a given

process. In any case, on either the ground or in a low gravity environment, surface tension driven flows can be prevented by either eliminating or isolating free surfaces.

Contraction Flow Another category of flow that can occur, either with or without gravity, is contraction flow. Density changes of either the solid or liquid due to temperature or concentration variations generate contraction flows. Similarly, if the density of the solid is different than the density of liquid, then any phase change generates pressure differences that drive flow. If the fluid is obstructed, such as by a dense mushy zone, then extremes of pressures can ensue with the result that hot tears or vapor pockets may form in the material.[10]

Buoyancy Driven Flow: Lateral Density Gradients In the presence of gravity (or any acceleration), flow will arise when there is a density gradient that is not precisely aligned with the gravity vector. In a binary solidifying system, density variations occur due to both thermal and solutal gradients. When the density gradients are perpendicular to the gravity vector, convective flow develops, regardless of the magnitude of the gradient.[28] Even the superposition of a vertically stabilizing density gradient (light on the top) has been shown insufficient to prevent natural convection in the presence of a lateral density gradient.[29]

Buoyancy Driven Flow: Vertical Density Gradients When the density gradient is precisely aligned with the gravity vector, then the system is in a state of static equilibrium, even if the density variation is such that the lighter fluid is on the 'bottom.' Unperturbed, the later case remains stratified. For a single component system, in which the density depends only on temperature, the stability of such a density inversion in response to a perturbation is measured by the thermal Rayleigh number. The Rayleigh number is a ratio of the buoyancy

forces to the viscous forces and, for a thermal driving force, is defined as

$$Ra_T = \frac{\rho g \beta_T \Delta T L^3}{\nu \alpha}$$

where ρ is the density, g the acceleration, β_T the thermal coefficient of expansion, ΔT the temperature change across the density inversion layer, L the height of the inversion, ν the kinematic viscosity, and α the thermal diffusivity. For a density inversion due to solutal effects alone, a similar situation exists, governed by a solutal Rayleigh number:

$$Ra_S = \frac{\rho g \beta_S \Delta C_l L^3}{\nu D}$$

where β_S is the solutal coefficient of expansion, ΔC_l the solutal change across the density inversion layer, and D the solutal diffusivity.

Thermosolutal Flow If both solutal and thermal gradients are present in the liquid, then an additional mechanism known as thermosolutal convection may result. This is a dynamic effect cause by the disparity between the rates of thermal and solutal diffusion. One of the best known examples of thermosolutal convection is 'salt-fountains' found in the ocean.[30] Even with a statically stable density gradient due to a positive temperature gradient, a parcel of fresh water rising from the bottom will continue to rise because it gains heat much faster than salt and becomes lighter than the surrounding fluid. Salt fountains thus occur when the component with the higher diffusion coefficient, e.g., temperature, creates a statically stable density profile and is opposed by the gradient of the component with the lower diffusion coefficient. The stability criterion proposed by Stern[30] for this phenomena is a critical combined Rayleigh number equal to the sum of the vertical thermal and solutal Rayleigh numbers.

A second, related, type of thermosolutal convection, known as diffusive convection, occurs when the component with the lower diffusion coefficient creates a

stable density gradient while the component with the higher diffusion coefficient is statically destabilizing. An example is fresh water over salt water, with temperature increasing with depth. In this case, an upwardly displaced fluid element is cooled, increasing its density and returning it to its original position with a density higher than that of the surrounding fluid. As a result, the fluid element drops below its original position and an oscillatory, overstable condition results. Linden provided a discussion of both types of thermosolutal convection for vertical temperature and solutal gradients and used linear stability theory to map the stability boundaries of those systems for a range of conditions.[31]

Thorpe, Hutt, and Soulsby have pointed out that thermosolutal mechanisms also apply to horizontal gradients of temperature and solute.[32] This is not to be confused with horizontal gradients of density, which as stated earlier, always result in convection. Horizontal gradients of temperature and solute may combine to produce flow. Thorpe et al. developed a stability criterion for such systems based on thermal and solutal Rayleigh numbers that includes both lateral and vertical length scales and gradients. Chen[33] has experimentally and analytically investigated the interaction of lateral and vertical, thermal and solutal gradients for a stratified salt solution in a wide container with lateral heating. From his observations, Chen proposed a critical Rayleigh number[33] based on lateral temperature changes (ΔT) and a length scale equal to the distance a parcel of fluid heated by ΔT would rise in the given density field.[34]

From these and other stability studies, it may be concluded that the task of predicting convective breakdown for even a relatively simple thermosolutal system is not straightforward. The question of stability for these systems becomes even more difficult with the inclusion of a non-uniform, transient mushy zone. The formation of a solid-liquid zone not only influences the solutal and thermal fields

but increases frictional influences in the mushy zone, providing an additional stabilizing effect.[7] Further consideration of container wall effects, complex thermal and solutal fields, and the transient nature of dendritic solidification indicates the difficulty of predicting thermosolutal convection for a real system.

Flows in the CAST Experiments The flow mechanisms listed above exist in the CAST unidirectional solidification experiments modeled here, with the exception (by design) of surface tension and residual flows. What remains are contraction effects, lateral density gradients, vertical density gradients, and thermosolutal interactions. Contraction flows are driven by density changes caused by cooling and solidification. In one-gravity, buoyancy flows may result from the density inversion that develops in the dendritic region due to solute rejected during solidification. In addition, opposing temperature and solutal gradients create the potential for thermosolutal flow in the statically stable layer above this density inversion. Buoyancy driven convection can also arise because of lateral gradients of both temperature and solute due to side wall effects. These natural convection flows are not limited to the ground studies, since the space flight experiment is expected to have some buoyancy flow driven by gravity gradients, crew movement, and other sources of acceleration.

The flow mechanism that dominates for a given set of run parameters depends largely on the gravity level. Whenever the combined effects of the mass flow is small, the primary mechanism of the transport of energy and solute will be diffusion. Under such conditions the process is termed diffusion dominated. The effect of convection relative to diffusion is conventionally measured using the Peclet number, which for energy is defined as $Pe_T = \frac{U \cdot L}{\alpha}$ and for solute as $Pe_S = \frac{U \cdot L}{D}$ where U is the velocity, L a characteristic length, and α and D are the thermal and solutal diffusivities respectively. As for stability, it is very difficult to define

appropriate length scales and a single set of dimensionless parameters that can be used to characterize such a complex process. It is because solidification of binary materials is such a complicated process that detailed experimentation and non-linear models are required.

Experimental Database

Experiments: Overview

The experimental investigation of dendritic solidification has covered a wide and varied range of systems and configurations but can be loosely classified according to the growth direction relative to the gravity vector. The first of these classifications is multidirectional solidification where the growth direction may assume any number of orientations relative to gravity. This configuration is representative of most castings, where freezing propagates inward from the walls of a three dimensional mold. Accordingly, this general configuration has been used in a number of qualitative studies, using ammonium chloride and water and other transparent metal models to investigate segregation phenomena in castings.[35,16,24,25] This general form of solidification is perhaps the most difficult to model because of the complicated boundary conditions and multidimensional flows inherent in the experimental configuration.

The next category of growth orientation is horizontal solidification where the temperatures gradients are imposed such that the solidification direction is perpendicular to the gravity vector. This configuration is less complicated than the first; but buoyancy driven flows remain an important feature due to the lateral density gradients. Mehrabian et al.[36] used this orientation to study macrosegregation and freckle formation in Al-Cu. The authors horizontally solidified an ingot in an insulated mold, with one end water cooled. They analyzed the macrosegregation using

wet chemistry and X-ray fluorescence. The results confirmed that interdendritic natural convection causes segregation. Stewart and Weinberg[37] also examined horizontal solidification and provided a direct observation of interdendritic flow in a metal using autoradiography to provide flow visualization for the interdendritic flows in Sn-Pb alloys. Szekely and Jassal[38] conducted perhaps the most meticulous early experiments investigating the lateral solidification of a binary system. The authors used dye tracing, Schlieren, thermocouples, still photography, and motion pictures to record the horizontal solidification of ammonium chloride and water in a 40 cm by 6 cm by 15 cm tank. The observed buoyancy driven flows were strong enough to shear dendrite arms and the velocity field in the bulk was observed to have a strong influence on the flow in the two-phase region. The authors also saw evidence of salt fingers, eruptions of interdendritic fluids, and intensive circulations in the dendritic region. This experiment has since been repeated by other investigators with the added sophistication of solutal measurements. In one of the subsequent studies,[39] the solutal distribution was determined using a miniature refractometer probe and, in another,[40] by withdrawing fluid and measuring the solutal concentration outside the test cell. In all of the horizontal growth experiments above, convection played a dominant role.

In a third orientation, the solidification is parallel to gravity, i.e., vertical. In this orientation, natural convection can theoretically be avoided if the critical Rayleigh number for the system is not exceeded. A number of processes, such as the growth of single crystal turbine blades, use vertical growth to control convection. Caldwell et al.[41] used this technique to reduce convection during the solidification of Al-4.5 pct Cu in a study on the refinement of dendrite arm spacings. Flemings et al.,[42,43] also solidified Al-Cu vertically in order to measure solutal redistribution in directional solidification. Verhoeven et al.[44] solidified

both with and opposite to gravity, using light and heavy solute, to investigate the effects of convection on the dendritic to eutectic transition. Similarly, the CAST experiments[2-9] use vertical growth to suppress convection below a critical Rayleigh number, allowing the study of the diffusion dominated solidification in a one-gravity environment.

When convection does occur in a vertical growth process, it can be significant, as demonstrated by Copley et al. in their study[21] on the origin of freckles in unidirectionally solidified castings, such as found in vertically solidified castings and electrode ingots. Ammonium chloride and water was solidified as a model material and the freckling phenomenon was shown to be due to convective jets of low density solute. Streat and Weinberg[45] showed the same freckling effect in unidirectionally solidified Pb-20 wt pct Sn using radioactive tracer techniques. Hellawell has subsequently investigated the mechanisms of the formation of these jets using aqueous ammonium chloride and lead-tin systems.[46,47] Thus vertical solidification can either be diffusion dominated below a critical transition point or convection dominated above that critical point.

The general conclusion from the above discussion is that either non-uniform or localized natural convection can lead to undesirable non-uniformities in the material being processed. The hope of producing improved materials has led, therefore, to a fourth solidification 'orientation': i.e., reduce the gravity vector as much as possible. This is possible using drop tubes, low-gravity parabolic flights on aircraft, sounding rockets, and spacecraft. The objective of the CAST program is to take advantage of these low-gravity environments to investigation dendritic solidification in the absence of gravity driven flows.

Casting and Solidification Technology (CAST)

The Casting and Solidification Technology (CAST) program has evolved from a number of early low-gravity dendritic solidification experiments on sounding rockets and the NASA KC-135 low-gravity aircraft. Johnston (McCay) et al.[26] solidified NH_4Cl-H_2O in a suborbital rocket at $10^{-5}g$ and compared the results with $1g$. The microgravity solidification was observed to be diffusion limited and the microgravity dendrite arm spacings were larger and more uniform. A similar experiment[20] was conducted during low-gravity and level flight maneuvers on board the NASA KC-135 aircraft where Mach-Zender interferometry was used to observe the solidification under low-gravity and one-gravity conditions. Comparison of the two showed the dynamic effects of acceleration on the solutal and thermal distributions. The restricted times of low-gravity in these experiments (20 seconds) limited their quantitative value. This limitation has led to the CAST proposal to unidirectionally solidify NH_4Cl-H_2O in the extended microgravity environment of the Fluids Experiment System (FES) on board the Space Shuttle.[48]

Preliminary ground-based studies have been and are being conducted in support of this proposed space mission using the basic configuration shown in Fig. I–1. In order to suppress convection, the experimental apparatus is oriented so that growth is vertical. As a result, the initial solidification in the ground-based experiments is diffusion dominated and is expected to be very similar to the initial phase of the microgravity experiments. However, once development of the solutal field causes the critical Rayleigh number to be exceeded, the ground-based experiments transition to convective dominated growth.

In support of CAST, the initial development of the diffusion layer ahead of the dendritic field has been recorded[4] using a confocal optical system. Particle tracking techniques[5] were also used to record the flow patterns associated with

the transition to convection dominated growth. These experiments demonstrated that this transition was due to a Rayleigh instability and exhibited a cellular flow structure at breakdown. After this set of investigations, a ruggedized version of the basic experiment (similar to Fig. I–1), along with optics for flow visualization was flows on the NASA KC-135 aircraft.[6] The objective was to use the low-gravity environment to extend the diffusion dominated growth time for the higher cooling rates (12°C/min) and compare the results with theory. Unfortunately, the results were inconclusive due to background lateral accelerations of the aircraft.

A ground-based Mach-Zender interferometer system was also constructed[8] in support of CAST and used to take data on the density field during solidification. This permitted the analysis of the transient solutal and thermal distributions above the interface and the determination of the combined thermal and solutal Rayleigh number associated with convective breakdown. These data serve as the foundation for the numerical comparisons made here. Details of the specific procedure and apparatus for these experiments can be found elsewhere[8,9] and only a brief overview is provided here.

The test section of the experiment consists of a 2.8 cm tall by 2.0 cm wide by 1.2 cm deep quartz cuvette, with inside dimensions of 2.5 cm tall by 1.6 cm wide by 0.8 cm deep, shown schematically in Fig. I–1. The cuvette is typically filled with a 28% ammonium chloride - 72% water solution. The top and bottom temperatures of the cuvette are monitored with thermocouples and regulated by computer controlled thermoelectric devices. The walls are uninsulated to allow for observation. In a typical experimental run, dendrites are first located on the bottom of the cuvette, either by supercooling the solution until nucleation occurs or with solid remaining from a previous run. In either case, the experiment is then brought to its initial condition by imposing and holding a predetermined

top and bottom temperature until conditions stabilize. The specific choice of those temperatures depends on the desired thermal gradient and thickness of the dendritic layer (mushy zone). This preparation phase of the experiment is referred to as the gradient hold. The resultant thermal, solutal, velocity, and two-phase distribution are referred to as the initial condition for the run. For all three sample solidification runs used for model validation, the top and bottom temperature were 58.5°C and 21°C, respectively. Once the initial conditions for a given run have stabilized and the mushy zone has reached its equilibrium height, the temperatures of the top and bottom of the cuvette are reduced at controlled rates. This phase of the experiment is referred to as either the thermal ramp or cooling phase. For the validation cases, the top and bottom temperatures are lowered at three different rates, 1°C/min, 2°C/min, and 3°C/min.

In the one gravity environment of the ground-based experiments, the cooling phase consists of three stages of growth. In the first stage, a conditionally stable stratified density inversion develops at the bottom of the cuvette, formed by the solute rejected during freezing. This stage is accordingly diffusion dominated. In the second stage, the density inversion reaches a critical height and the density inversion layer breaks apart into a series of cells resembling Rayleigh–Benard cells.[5] This is the transition stage of the experiment. After the inversion layer breakdown, the process rapidly becomes dominated by convective growth as large currents develop, transporting species and energy to the mushy zone and greatly influencing the growth pattern. For all three stages of growth, interferometric data are collected in order to determine the index of refraction distribution which is directly related to the solutal and thermal distributions.[20] Additional experimental data is obtained by seeding the solution with neutrally buoyant Plexiglas spheres and using time-lapse photography for flow visualization.[5] For both the interfer-

ometry and particle tracking, the plane of data acquisition is parallel to the front and back faces of the cuvette relative to the view in Fig. I–1. Particle tracking photographs, interferometric images, and ambient light photographs taken during a run are used for direct comparison with the FTM numerical results.

Modeling Efforts

Early models of dendritic solidification were typically one-dimensional. In 1953, Tiller et al.[13] derived a one-dimensional analytical expression for the solutal distribution ahead of a planar growth front in the absence of convection. The authors investigated the effects of transient growth rate and briefly discussed the effects of dendritic materials. Tien and Geiger[49] subsequently calculated an exact, one-dimensional solution for dendritic solidification. The analysis provided the transient temperature distribution and the thickness of both the solid region and mushy zone for a semi-infinite binary material chilled from the boundary. Exact solutions for the solidification of a binary material in a semi-infinite region have also been provided by Cho and Sunderland[50] and more recently by Lipton et al.[51] These analytical solutions are idealizations of the actual process, neglecting a number of effects and often relying on ad-hoc boundary conditions such as estimates of the solutal concentration at the dendrite tips.

The one-dimensional models can provide useful results for certain situations. Brody and Flemings,[52] for example, used an essentially one-dimensional numerical model which included assumptions about the two-dimensional structure of dendrites to study microsegregation during unidirectional solidification. The model was primarily a thermal analysis that related the solutal concentration and fraction of solid to local temperatures using conservation principles, subject to a number of assumptions. These assumptions included no mass flow, a fixed rate of growth,

planar isotherms and fixed plate-like dendrite geometries. The authors used the model to investigate the effects of solid solutal diffusion on the final segregation in unidirectionally solidified Al-Cu alloys.

Caldwell and coworkers[41] also constructed a one-dimensional numerical heat flow model and used it successfully to predict the local solidification times for Al-4.5 wt pct Cu alloys in a study on the refinement of dendrite arm spacings. Their model used empirical formulations to incorporate a number of effects including the heat of fusion, heat transfer at the chill face, side wall heat loss, and even convective effects by using an effective thermal conductivity. This work was also one of the first to include undercooling effects in a numerical model by assuming that the dendrite tips were undercooled by an amount sufficient to freeze .05 volume fraction of solid.

While these one-dimensional models provided quantitative information concerning unidirectional solidification, they were fundamentally limited in their capability to model basic effects such as irregular interfaces, two-dimensional convection, and other multi-dimensional phenomena. These early models were also limited by such simplifying assumptions as specified growth rates, prescribed flow and thermal fields, and simplified models for the solutal concentration. Although the solidification process depends strongly on the interaction between the temperature, solutal, and flow fields, early models decoupled these relationships in order to make the problems tractable.

Subsequent models extended the domain to two-dimensions and included the interrelated effects of energy, momentum, and solutal concentration. Flemings and colleagues[53,54] extended the one-dimensional Brody and Flemings microsegregation model[52] to two-dimensions and included the effects of interdendritic contraction flow on the solutal distribution in the mushy zone. This new model was

confined to the mushy zone, however, and neglected bulk flow effects. It also assumed a flat interface, no diffusion in the solid and a fraction of liquid in the mushy zone that varied linearly with temperature. Additional assumptions included specification of the solidus and liquidus temperature translation speeds and independence of the thermal field and solidification rates with respect to the flow velocities. Thus the model did not include many of the effects of convection.

The above interdendritic flow model was extended[55] to include buoyancy driven convection in the mushy region, using Darcy's porous flow equation to account for the flow resistance in the two phase region. The analysis still retained the earlier assumptions, including that the thermal field and flow field were decoupled. This shortcoming was rectified in a subsequent model,[56] in which the heat and momentum were linked and solved simultaneously in the interdendritic zone. Even that version still included many of the limitations of its predecessors such as specified growth rates and no bulk flow effects.

The first general coupling of the energy field with the momentum equations for a solidifying system was done by Szekely and Jassal[38] in support of their NH_4Cl-H_2O solidification experiments. Their model predicted temperature, fraction of solid, and velocity for the entire ammonium chloride-water domain, not just the mushy zone. The effects of the bulk flow were included and the translation rate of the growth front was calculated rather than specified. The model domain was divided into three regions: the solid region, the mushy zone, and the fully liquid region; each separated by planar boundaries. The conservation of energy and momentum equations were written separately for each region and then linked at the boundaries, i.e., between regions. The density was assumed to be a function of the temperature and the fraction of solid. The authors were able to obtain qualitative correlation between the observed and computed flow patterns for both

the mushy zone and the bulk flow region. The temperature distribution across the test cell and growth rates were also shown to correlate with the experimental data. The main elements missing in the model by Szekely and Jassel were the solutal transport equations.

The solutal transport equations were not incorporated into comprehensive models similar to Szekely and Jassal's for approximately a decade. In the interim, solutal effects on dendritic solidification, in particular for vertical unidirectional solidification, were investigated using linear and non-linear thermosolutal stability models. The first stability analyses of vertical directional binary solidification were linear,[57] followed by non-linear analyses such as the study of thermosolutal convection by McFadden et al.[58] In that work, the authors solved for the flow, concentration, and temperature above a vertically solidifying planar interface. The interface growth rate was set to a constant and an artificial upper boundary was imposed at which the temperature, concentration, and velocity perturbations from the steady state solution were fixed to zero. The solution was assumed periodic in the horizontal direction so that, in effect, the domain had frictionless side walls. The model was used to investigate thermosolutal flow patterns at various thermal and solutal Rayleigh numbers. McFadden and Coriell[59] later employed this same model to investigate multiple flow solutions for a given set of boundary conditions. Heinrich[60] also analyzed the same idealized configuration using a different numerical approach (finite element vs. finite difference) to solve the non-linear equations. He also made the problem more realistic by including solid side walls in his model to determine their effect on the flow pattern. The model did not include a mushy zone, however. This feature was added in later linear[61] and non-linear[62] analyses. The conclusion of these later studies, was that simplified models which did not include the mushy zone were inadequate for the analysis of convective stability of

binary systems. In addition to predictions on the stability of the system, the non-linear model predicted a qualitative flow pattern at convective breakdown that consisted of an organized system of cells similar to those observed in the CAST system.[5] Another conclusion from this model was for the Pb-Sn alloys under consideration, the majority of the convection was predicted to be in the all-liquid region with flow penetrating into the mushy zone no more than 20% of the zone height. These later models provided new information about a solidifying binary system, but applied only to an ideal system. The unperturbed state was assumed to be steady state growth with flat isotherms, flat isoconcentrates, and a constant mushy zone porosity. Thus certain aspects of a real system were neglected, such as lateral gradients of temperature and concentration and the transient nature of the mushy zone.

Voller and Prakash[63] proposed a model for computing convection and diffusion in phase change problems with mushy zones that was similar to the generalized approach of Szekely and Jassal,[38] but with a number of improvements. They used a conservative control volume technique in which one equation set is applied over the entire domain, eliminating the need for artificially prescribed internal boundaries found in the Szekely and Jassal model. In addition, the code solved for all the conserved quantities, including solute. The authors demonstrated the feasibility of the technique using a hypothetical material for which the fraction of solid, f_s, in the two-phase region was linearly proportional to the temperature in the region between the liquidus and solidus. They used the model to compute the evolution of the thermal, solutal, velocity, and dendrite distribution for this hypothetical system subjected to cooling from the side.

Beckermann and Viskanta[40] developed a control volume technique similar to that of Voller and Prakash in support of their own experiments on the horizontal

solidification of the ammonium chloride and water system. This combination of experiment and numerical model resembled the earlier work of Szekely and Jassal[38] but with the added sophistication of measuring and calculating the solutal distribution. Beckermann and Viskanta improved on the model proposed by Voller and Prakash[63] by including a realistic specification of the fraction of solid in the two-phase region as a function of both the temperature and the solutal concentration. As with the Voller and Prakash model, the heat, solute, and mass transfer were calculated over the entire domain using one set of conservation equations. The model assumes Newtonian and laminar flow and incorporates a Darcy friction factor in the two-phase region. Beckermann and Viskanta also incorporated other common assumptions such as the Boussinesq approximation and the assumption of equilibrium within each numerical control volume. In applying their model for the case of ammonium chloride and water being chilled at a side wall, the authors were unable to produce quantitative agreement between the numerical model and the experimental data, but the model did provide qualitative agreement and further established the feasibility of using control volume techniques to model a solidifying binary system.

In order to address some of the shortcomings of the Beckermann and Viskanta model,[40] Beckermann and Ni[64] developed a model based upon separate conservation equations for the solid and liquid phases, permitting the interactions between the two to be explicitly included. This class of models is referred to as two-phase average models, as opposed to one-phase models in which the solid and liquid are treated as a continuum. One advantage to this approach is it enables the calculation of solid motion as well as fluid flow. This dual momentum equation approach is essential for any system with either convected or settling solid fragments. (Such a capability is not required for the CAST experiment where the dendrites are

observed to remain fixed.) In general, the model[64] provides an excellent format for the explicit incorporation of solid-liquid interactions such as non-equilibrium and kinetic effects. The ability to include non-equilibrium and kinetic effects is not unique to two-phase averaged models, however, but can also be included in one-phase models,[65] such as the FTM.

In parallel with the work of Voller and Prakash[63] and Beckermann,[40] Bennon and Incropera[66] formulated a set of continuum equations for momentum, heat, and species transport in binary solid-liquid phase change systems. This set of equations is predicated on the assumption that all the properties of the medium are continuous. Given this premise, the equations were rigorously derived for a general two-phase system. It is this equation set which was used to generate the conservation equations of the FTM.

Bennon and Incropera also used the continuum equation set to develop a model which was subsequently applied to to the NH_4Cl-H_2O binary system.[39,67,68] The authors made a number of assumptions to simplify the computations. They incorporated the Boussinesq approximation and equated the solid and liquid densities, thus neglecting all contraction flows. A Darcy term was used to account for the momentum exchange between the solid and the liquid in the two-phase region. The solid itself was assumed to be stationary and thermodynamic equilibrium was enforced for each control cell within the domain. The model was applied to the rapid, horizontal solidification of ammonium chloride and water in a rectangular cavity with imposed lateral temperature gradients and the results showed qualitative but not quantitative agreement. More recently,[69] the model has been applied to other configurations (solidification at the center of a cylinder) and other binary materials (Na_2CO_3-H_2O), again with good qualitative agreement but limited quantitative correlation.

The above models demonstrate the feasibility of using conservation equations coupled with numerical control volumes technique to model the solidification of binary systems. However, many improvements are still needed. In addition to gross flow effects and qualitative features, subtle effects must also be incorporated if model predictions are to match experimental data. This is particularly true for the CAST experiments to be modeled by the FTM, since they involve the development of thermal and solutal boundary layers on a very fine scale.

SECTION III

NUMERICAL MODEL

Overview

The CAST Fluids and Thermal Model (FTM) developed here is based on the control volume approach outlined by Patankar[70] using the continuum conservation equations as given by Bennon and Incropera.[66] It is a transient, two-dimensional, single fluid, computational fluid dynamics code which calculates the temperature, solutal concentration, flow field, and fraction of solid for a solidifying binary material, in particular NH_4CL-H_2O. An overview of the code features and capabilities are listed in Fig. III–1.

MODEL FEATURES AND CAPABILITIES	
Domain:	Quartz Cuvette and Ammonium Chloride/Water Solution
Type:	Transient, 2-Dimensional, Single Fluid, Two-Phase
Output:	Temperature, Concentration, Velocity
	Fraction of Solid, Other Properties
	Relevant Dimensionless Parameters

Figure III–1. Model features and capabilities

The model is specifically configured to mimic the CAST vertical directional solidification experiments[2–9] for the binary material NH_4Cl-H_2O, including the boundary conditions. For example, the temperatures in the experiments are computer controlled via thermoelectric devices on the top and bottom of the quartz

cuvette. Accordingly, the top and bottom temperatures in the code are specified on the outside of the quartz and the model solves for the temperature throughout the field, including the solution and the quartz container. As with the experiments, these controlling temperatures are specified as polynomial functions of time. The heat exchange with the environment for the exposed front, back, and side walls is included via a Newton cooling model.

In the experiment, the density changes due to solidification and due to thermal contraction require that fluid be added to the cuvette via a supply tube in order to avoid bubble formation and container breakage. This physical complication caused by the density variation is often avoided numerically by assuming that the density of the liquid varies only in the body force term (the Boussinesq approximation), and by also assuming that the density of the solid and liquid are equal. In the FTM, the densities of the solid and liquid are each treated as functions of temperature and solutal concentration. Thus, the expansion flows due to cooling and solidification are fully modeled. In order to account for the influx of fluid into the domain, the code provides for a source of the fluid at the numerical control volume corresponding to the physical location of the fluid resupply tube attached to the cuvette.

The distribution of phases of the NH_4Cl-H_2O in a given control volume is dictated by the net energy in the cell, the solutal concentration, and the equilibrium phase diagram coupled with nucleation conditions. If the nucleation criteria (to be discussed in the section on phase transformation), are not satisfied in a particular control volume, then the fluid is allowed to undercool and a non-equilibrium condition results. This situation is known to exist in nature and is necessary to achieve good correlation between model predictions and experimental results. When solidification does occur, the dendritic solid is assumed to be stationary.

The solid-liquid mixture which constitutes the mushy zone is treated as a continuum and the momentum exchange between solid and liquid in the region is modeled using Darcy's law. These and other assumptions of the model are listed in Fig. III–2.

MODEL ASSUMPTIONS AND LIMITATIONS

Two-Dimensional

Laminar Flow

Zero Velocity Solid

Newton Cooling for Environmental Heat Transfer

Zero Diffusion in the Solid

Negligible Solute in the Solid

Darcy's Law in the Mushy Zone

Nucleation a Function of Undercooling and Pre-existing Solid

Local Thermodynamic Equilibrium once Nucleated

Figure III–2. Model assumptions and limitations

The assumptions listed in Fig. III–2 have the following significance. In modeling the CAST ground system, the most significant model limitation is that of two-dimensionality. Even though the CAST experiment is designed as a primarily one-dimensional, unidirectional solidification study, it has inherent three-dimensional aspects. This is particularly true during and immediately after the transition to convection dominated growth. Prior to that transition, however, the two-dimensional assumption will be shown to be a reasonable approximation. Experimental observations indicate that the assumption of laminar flow is another

model feature that is valid for the diffusion dominated growth phase, but inadequate for the fully convective growth stage. The third assumption in Fig. III–2, zero velocity solid, is valid for the stages of growth modeled here since the convection is not vigorous enough to break and transport dendrite arms. The simplification of no diffusion in the solid is based on the low diffusivity of the solute (water) in solid NH_4Cl-H_2O. Similarly, neglecting the water in the solid is based on the small partition ratio ($k = .004$) for the material.[5]

A result of the above boundary conditions, assumptions, and limitations is that three empirical terms must be defined in the model. These are the heat transfer coefficient for the Newton cooling at the walls, the geometrical parameter for the nucleation criteria, and the resistance coefficient used in the Darcy term. All other input parameters for a given run are dictated by experimental boundary conditions. Given these boundary conditions and empirical coefficients, the FTM applies the basic principles of conservation of energy, solute, momentum, and mass, coupled with the properties of the material to compute the properties of the medium. Details of how these conservation equations and equations of state are solved are provided in the following sub-sections.

Conservation of Energy

Conservation of Energy: Basic Equation

Based on the Bennon and Incropera continuum model,[66] the energy equation for the binary solution is

$$\frac{\partial}{\partial t}(g_l\rho_l h_l + g_s\rho_s h_s) + \nabla\cdot(g_l\rho_l\vec{V}_l h_l + g_s\rho_s\vec{V}_s h_s) = \nabla\cdot[(g_s k_s + g_l k_l)\nabla T]. \quad (1)$$

In the above, T is the temperature of the solid or liquid, and g_s and g_l are the volume fractions of the solid and liquid, respectively. The solid and liquid densities

are given by ρ_s and ρ_l, and $\vec{V}_s$ and $\vec{V}_l$ are the corresponding velocities. The solid and liquid conductivities are k_s and k_l, and the solid and liquid enthalpies are h_s and h_l. The enthalpies are related to temperature using two-dimensional truncated Taylor series,

$$h_l \approx \frac{\partial h_l}{\partial T}(T - T_0) + \frac{\partial h_l}{\partial C_l}(C_l - C_0) + h_{l_0}(T_0, C_0) \tag{2a}$$

$$h_s \approx \frac{\partial h_s}{\partial T}(T - T_0) + \frac{\partial h_s}{\partial C_s}(C_s - C_0) + h_{s_0}(T_0, C_0)\ . \tag{2b}$$

The temperature, T_0, and the concentration, C_0, are the reference temperature and concentration. Since the conservation equations deal only with relative enthalpy, the liquid enthalpy at the reference point, $h_{l_0}(T_0, C_0)$, can be arbitrarily set to zero and the solid enthalpy at the same point, $h_{s_0}(T_0, C_0)$, becomes equal to the negative of the latent heat. In addition, for ammonium chloride and water, the change of enthalpy with a change in liquid concentration $\dfrac{\partial h_l}{\partial C_l}$ is negligible. With these simplifications for the enthalpy and the assumption that the solid is rigid, $(\vec{V}_s = 0)$, the conservation of energy can be rewritten in terms of temperature:

$$\begin{aligned}\frac{\partial}{\partial t}\left[g_l\rho_l\left(\frac{\partial h_l}{\partial T}(T - T_0)\right) + g_s\rho_s\left(\frac{\partial h_s}{\partial T}(T - T_0) + \frac{\partial h_s}{\partial C_s}(C_s - C_0) + h_{s_0}\right)\right] \\ + \nabla\cdot\left[g_l\rho_l\vec{V}_l\left(\frac{\partial h_l}{\partial T}(T - T_0)\right)\right] = \nabla\cdot[(g_sk_s + g_lk_l)\nabla T]\ .\end{aligned} \tag{3}$$

Regrouping gives the energy equation used in the numerical model:

$$\frac{\partial}{\partial t}\left[\left(g_l\rho_l\frac{\partial h_l}{\partial T} + g_s\rho_s\frac{\partial h_s}{\partial T}\right)T\right] + \nabla\cdot\left[g_l\rho_l\vec{V}_l\frac{\partial h_l}{\partial T}T\right] = \nabla\cdot[(g_sk_s + g_lk_l)\nabla T] + S \tag{4a}$$

where

$$\begin{aligned}S = \frac{\partial}{\partial t}\left[g_l\rho_l\frac{\partial h_l}{\partial T}T_0 + g_s\rho_s\left(\frac{\partial h_s}{\partial T}T_0 - \frac{\partial h_s}{\partial C_s}(C_s - C_0) - h_{s_0}\right)\right] \\ + \nabla\cdot\left[g_l\rho_l\vec{V}_l\left(\frac{\partial h_l}{\partial T}T_0\right)\right]\ .\end{aligned} \tag{4b}$$

Conservation of Energy: Control Volume Expression

The partial differential equation from above is integrated over a control volume using the implicit method outlined by Patankar.[70] A sample energy control volume is provided in Fig. III–1. Integrating the conservation of energy over the control volume gives:

$$\frac{\Delta x \Delta y}{\Delta t}\left[\left(g_l\rho_l\frac{\partial h_l}{\partial T}T + g_s\rho_s\frac{\partial h_s}{\partial T}T\right) - \left(g_l^0\rho_l^0\frac{\partial h_l^0}{\partial T}T^0 + g_s^0\rho_s^0\frac{\partial h_s^0}{\partial T}T^0\right)\right] + J_e - J_w + J_n - J_s = S\Delta x\Delta y \tag{5}$$

where the J's are the net energy fluxes across the control cell faces. These fluxes include convection in the liquid and diffusion in both the solid and the liquid. As an example, the flux at the east face is:

$$J_e = F_eT_e - \Delta y \cdot g_{l_e}k_{l_e}\left(\frac{\partial T}{\partial x}\right)_{l_e} - \Delta y \cdot g_{s_e}k_{s_e}\left(\frac{\partial T}{\partial x}\right)_{s_e} \tag{6}$$

where F_e is a modified mass flux defined as the actual mass flux, Flux_e, times the specific heat:

$$F_e = \text{Flux}_e \cdot C_{p_l}, \quad \text{where} \quad \text{Flux}_e = \Delta y \cdot g_{l_e}\rho_{l_e}u_{l_e} \tag{7}$$

The source term, $S\Delta x\Delta y$, for the cell is:

$$\begin{aligned} S\Delta x\Delta y = {} & \frac{\Delta x\Delta y}{\Delta t}\left[g_l\rho_l\frac{\partial h_l}{\partial T}T_0 + g_s\rho_s\left(\frac{\partial h_s}{\partial T}T_0 - \frac{\partial h_s}{\partial C_s}(C_s - C_0) - h_{s_0}\right)\right]_P^{\text{new}} \\ & - \frac{\Delta x\Delta y}{\Delta t}\left[g_l\rho_l\frac{\partial h_l}{\partial T}T_0 + g_s\rho_s\left(\frac{\partial h_s}{\partial T}T_0 - \frac{\partial h_s}{\partial C_s}(C_s - C_0) - h_{s_0}\right)\right]_P^{\text{old}} \\ & + (F_e - F_w + F_n - F_s)\cdot T_0 + S_pT + S_c \end{aligned} \tag{8}$$

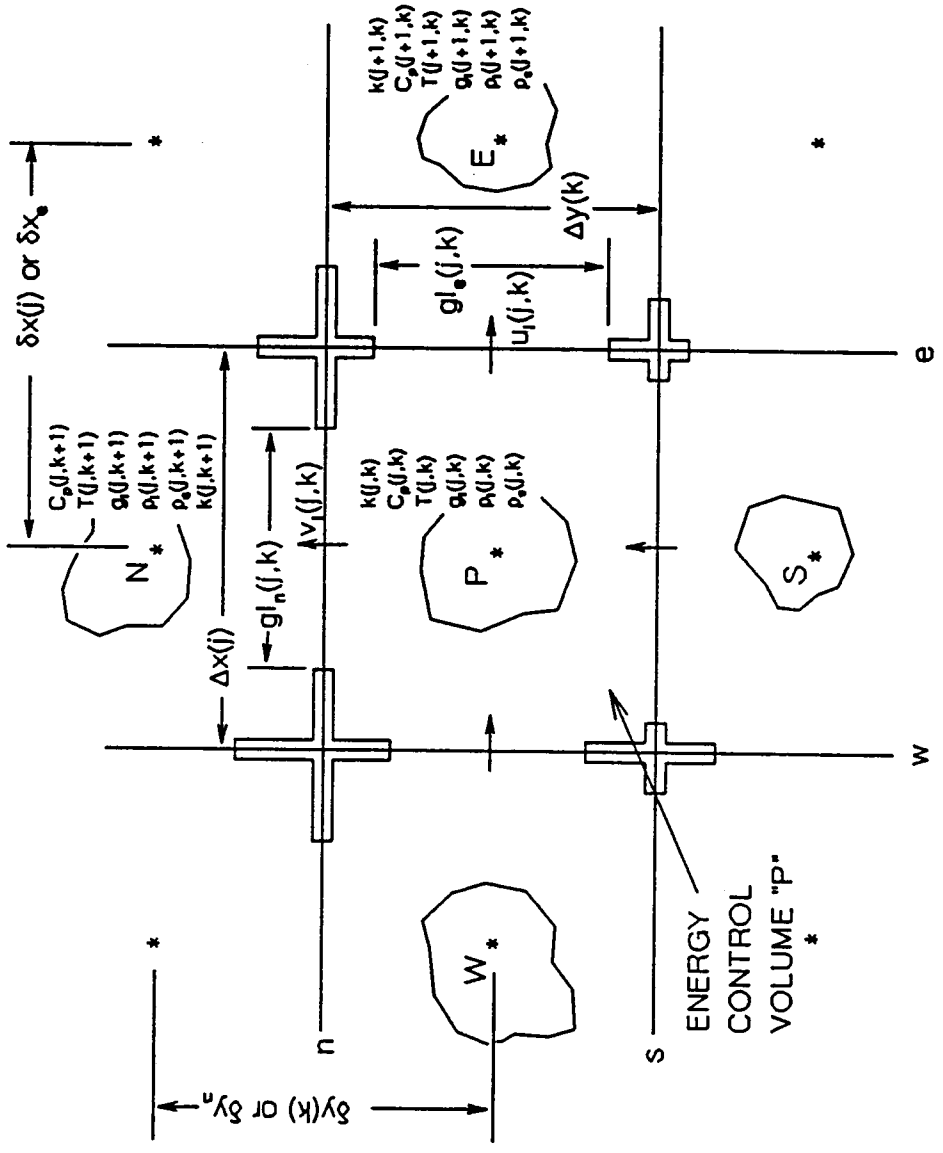

Figure III-3. Energy control volume

The 'new' and 'old' notations in Eq. (8) refer to the current and previous time step values for the bracketed variables. The terms, S_pT and S_c, have been added in Eq. (8) to account for external energy sources. For example, S_pT and S_c can be used to introduce a Newton cooling term. The S_c term is also used in the domain to account for the energy influx which results from mass addition at the supply tube. In addition, the source term, S_c, may be used as a means of introducing error corrections, as will be explained later. (Note that in the following discretization, the S_pT term will be moved to the left-hand side of the above equation since it depends directly on the control volume temperature.)

Conservation of Energy: Assumptions

Equations (5)–(8) represents the conservation of energy in the control volume centered on point 'P'. This equation states that the change in energy in a cell over time must equal the net flow of energy across the cell boundaries plus any internal additions of energy over the same time interval. The principle difficulty in applying the above equation is expressing the cell boundary terms as functions of parameters stored at the cell centers. Since most of the parameters associated with the energy control cell, such as pressure, temperature, concentration and the physical properties, are either calculated or specified at the cell centers, a number of assumptions must be made in order to determine the gradients and other values at the cell faces. This 'spatial' offset of parameters requires that values be extrapolated either from node to face or from face to node. This necessary extrapolation leads to significant complication of the linearized equations. More importantly, the choice of the interpolation method may affect the solution convergence rate and could even influence the final solution.

The velocities, u_l's and v_l's, and the fraction of liquids, g_l's, are directly calculated in the conservation of momentum and phase change subroutines and stored at the cell faces, but the remaining parameters, T, ρ_l, k_l, k_s, C_{p_l}, C_{p_s}, $\left(\frac{\partial T}{\partial x}\right)_l$, and $\left(\frac{\partial T}{\partial x}\right)_s$, must be interpolated or calculated based on nodal values. To accomplish this, several assumptions are made. The solid and liquid thermal conductivities, k_s and k_l, at a cell face are assumed to be the harmonic average of the values at the adjacent cell nodes. The advantage of a harmonic average for the conductivity, as opposed to an arithmetic average, is that harmonic averaging ensures that the energy fluxes across the cell face are consistent.[70] The gradient of the solid temperature at the interface, $\left(\frac{\partial T}{\partial x}\right)_s$, is based on a linear temperature profile between the adjacent nodes. For the liquid conduction and convection, the temperature, T, and the gradient in the liquid, $\left(\frac{\partial T}{\partial x}\right)_l$ at the control volume cell face, are based on the exact 1-D solution for the temperature distribution between two points with fixed velocity, u, fixed density, ρ_l, fixed conductivity, k, and fixed specific heat, Cp_l. The values of ρ_l and Cp_l incorporated in this one dimensional approximation are the upwind values. A summary of the assumptions discussed thus far are listed in Fig. III–4.

Conservation of Energy: Discretized Fluxes

The above assumptions do not provide a direct means of computing the flux terms, J_e, J_w, J_n, and J_s, in Eqs. (5)–(8). The discretized expressions for those flux terms are derived in this sub-section. The terminology and basic approach used are consistent with that used in Patankar's text.[70] The first step is to move the S_pT source term to the left-hand side, and define the following diffusive flux coefficients,

1) Enthalpy is approximated as a function of temperature,

$$h_l \approx Cp_l \cdot (T - T_0)$$
$$h_s \approx Cp_s \cdot (T - T_0) + \frac{\partial h_s}{\partial C_s} \cdot (C_s - C_0) - L.$$

The above is the Taylor series given in Eq. (2) with h_{l_0} set to zero, $\frac{\partial h_l}{\partial C_l} \cdot (C_l - C_0)$ assumed negligible, and h_{ref_s} set to the negative of the latent heat $-L$ at T_0, C_0. The term $\frac{\partial h_s}{\partial C_s} \cdot (C_s - C_0)$ is retained and used to ensure the correct latent heat for pure water or pure NH_4Cl.

2) The solid and liquid temperature are equal in a cell:

$$T_{s_P} = T_{l_P}$$

3) The conductivities at the cell faces, k_s and k_l, are evaluated by harmonic averaging:

$$k_{l_e} = \frac{k_{l_P} k_{l_E}}{k_{l_P} + k_{l_E}} \qquad \text{(uniform grid)}$$

$$k_{s_e} = \frac{k_{s_P} k_{s_E}}{k_{s_P} + k_{s_E}} \qquad \text{(uniform grid)}$$

4) The density and specific heat at the faces are upwinded:

$$\rho_{l_e} = \rho_{l_{\text{up}}}$$
$$Cp_{l_e} = Cp_{l_{\text{up}}}$$

5) The temperature gradient between nodes in the solid is assumed linear:

$$\left(\frac{\partial T}{\partial x}\right)_{s_e} = \frac{T_E - T_P}{\delta x_e}$$

Figure III–4. Discretized energy equation assumptions

$$
\begin{aligned}
D_{l_e} &= \frac{\Delta y \cdot g_{l_e} \cdot k_{l_e}}{\delta x_e}, & D_{s_e} &= \frac{\Delta y \cdot (1 - g_{l_e}) \cdot k_{s_e}}{\delta x_e} \\
D_{l_w} &= \frac{\Delta y \cdot g_{l_w} \cdot k_{l_w}}{\delta x_w}, & D_{s_w} &= \frac{\Delta y \cdot (1 - g_{l_w}) \cdot k_{s_w}}{\delta x_w} \\
D_{l_n} &= \frac{\Delta x \cdot g_{l_n} \cdot k_{l_n}}{\delta y_n}, & D_{s_n} &= \frac{\Delta x \cdot (1 - g_{l_n}) \cdot k_{s_n}}{\delta y_n} \\
D_{l_s} &= \frac{\Delta x \cdot g_{l_s} \cdot k_{l_s}}{\delta y_s}, & D_{s_s} &= \frac{\Delta x \cdot (1 - g_{l_s}) \cdot k_{s_s}}{\delta y_s}
\end{aligned}
\tag{9}
$$

so that the energy conservation Eq. (5) can be rewritten as,

$$
\begin{aligned}
\frac{\Delta x \Delta y}{\Delta t} \left[(\rho_l C p_l T_P g_l + \rho_s C p_s T_P g_s) - (\rho_l^0 C p_l^0 T_P^0 g_l^0 + \rho_s^0 C p_s^0 T_P^0 g_s^0) \right] \\
+ J_e - J_w + J_n - J_s - S_P T_P = b
\end{aligned}
\tag{10}
$$

where now, a sample flux term such as Eq. (6) is as follows:

$$
J_e = F_e T_e - D_{l_e} \cdot \delta x_e \cdot \left(\frac{\partial T}{\partial x} \right)_{l_e} - D_{s_e} \cdot \delta x_e \cdot \left(\frac{\partial T}{\partial x} \right)_{s_e} \tag{11}
$$

and the right-hand side of the energy equation has been regrouped to give:

$$
\begin{aligned}
b = S_c + T_0 \cdot \left[(\rho_l C p_l g_l + \rho_s C p_s g_s) - (\rho_l^0 C p_l^0 g_l^0 + \rho_s^0 C p_s^0 g_s^0) \right] \frac{\Delta x \Delta y}{\Delta t} \\
+ T_0 \cdot (F_e - F_w + F_n - F_s) + \frac{\Delta x \Delta y}{\Delta t} \cdot \left(L - \frac{\partial h_s}{\partial C_s} \cdot (C_s - C_0) \right) \cdot (\rho_s g_s - \rho_s^0 g_s^0).
\end{aligned}
\tag{12}
$$

The 'b' in this formulation of the conservation of energy equations is similar to the source term $S \Delta x \Delta y$ in Eqs. (5)–(8) except that $S_p T$ term has been moved to the left-hand side of the energy equation and the specific heat, $\frac{\partial h}{\partial T}$, has been relabeled as C_p.

As mentioned at the beginning of this section, before the conservation of energy equation can be solved, the unknown energy fluxes at the cell faces, J_e, J_w, J_n, and J_s, must be expressed in terms of known values stored at the cell centers. The approach[70] adopted here is to compute the fluxes at the cell faces

based on the exact solution for one-dimensional steady state flow between nodes. For example, consider the east face flux. If the density, velocity, and specific heat between nodes 'P' and 'E' (see Fig. III–1) are considered constant, then the flux through the liquid at the east face as given in Eq. (12) has the form

$$J_l(x) = K_1 T(x) - K_2 \left(\frac{\partial T}{\partial x}\right) \tag{13}$$

where, $K_1 = F_e$ and $K_2 = D_{l_e}\delta x_e$. Since $J_l(x)$ in the above equation is constant over the interval (the assumed profile is steady-state), the equation for $J_l(x)$ can be differentiated to give:

$$0 = \left(\frac{\partial T}{\partial x}\right) - \frac{K_2}{K_1}\left(\frac{\partial^2 T}{\partial x^2}\right). \tag{14}$$

The temperature distribution which satisfies this equation is

$$T(x) = C_1 e^{K_1/K_2} + C_2, \tag{15}$$

where, in order to satisfy the boundary conditions of $T = T_P$ at $x = 0$ and $T = T_E$ at $x = \delta x_e$, the constants C_1 and C_2 must be

$$\begin{aligned} C_1 &= \frac{T_E - T_P}{e^{(K_1/K_2)\cdot\delta x_e} - 1} \\ C_2 &= T_P - \frac{T_E - T_P}{e^{(K_1/K_2)\cdot\delta x_e} - 1}. \end{aligned} \tag{16}$$

When this temperature distribution is substituted into the equation for the flux in the liquid, J_l, and evaluated at the convenient location of $x = 0$ (remembering that for this one-dimensional steady state approximation the energy flux is constant between $x = 0$ and $x = \delta x_e$, so that it can be evaluated anywhere in the interval), the flux of energy through the fluid at the east face, J_{l_e}, is determined explicitly as,

$$J_{l_e} = K_1 \left[T_P - \frac{T_E - T_P}{e^{(K_1/K_2)\times\delta x_e} - 1}\right] \tag{17}$$

or, substituting for K_1 and K_2,

$$J_{l_e} = F_e \left[T_P - \frac{T_E - T_P}{e^{(F_e/D_{l_e})} - 1} \right]. \tag{18}$$

When this expression for the energy flux through the liquid at the east face of the control volume is combined with the energy flux through the solid the resulting total east face energy flux [Eq. (11)] becomes

$$J_e = F_e T_P + \left[\frac{F_e}{e^{(F_e/D_{l_e})} - 1} \right] T_P - \left[\frac{F_e}{e^{(F_e/D_{l_e})} - 1} \right] T_E - D_{s_e} T_E + D_{s_e} T_P. \tag{19}$$

By analogy, substituting W for P, P for E, and w for e, gives an expression for the total energy flux through the west cell face

$$J_w = F_w T_W + \left[\frac{F_w}{e^{(F_w/D_{l_w})} - 1} \right] T_W - \left[\frac{F_w}{e^{(F_e/D_{l_w})} - 1} \right] T_P - D_{s_w} T_P + D_{s_w} T_W. \tag{20}$$

When the above expression for the energy flux across the east and west face of the control cell is substituted into a one-dimensional version of the energy equation [Eq. (10)], it can be arranged in the form,

$$a_P T_P = a_E T_E + a_W T_W + a_P^0 T_P^0 + b \tag{21a}$$

where

$$\begin{aligned}
a_P &= a_E + a_W + (F_e - F_w) + \frac{\Delta x \Delta y}{\Delta t} \left[\rho_l C p_l g_l + \rho_s C p_s (1 - g_l) \right] - S_P \\
a_E &= \frac{F_e}{e^{(F_e/D_{l_e})} - 1} + D_{s_e} \\
a_W &= \frac{F_w}{e^{(F_w/D_{l_w})} - 1} + D_{s_w} + F_w \\
a_P^0 &= \frac{\Delta x \Delta y}{\Delta t} \left[\rho_l^0 C p_l^0 g_l^0 + \rho_s^0 C p_s^0 (1 - g_l^0) \right]
\end{aligned} \tag{21b}$$

and

$$\begin{aligned}
b = S_c + T_0 \cdot \left[(\rho_l C p_l g_l + \rho_s C p_s g_s) - (\rho_l^0 C p_l^0 g_l^0 + \rho_s^0 C p_s^0 g_s^0) \right] \frac{\Delta x \Delta y}{\Delta t} \\
+ T_0 \cdot (F_e - F_w) + \frac{\Delta x \Delta y}{\Delta t} \cdot \left(L - \frac{\partial h_s}{\partial C_s} \cdot (C_s - C_0) \right) \cdot (\rho_s g_s - \rho_s^0 g_s^0).
\end{aligned} \tag{21c}$$

Paralleling the development in Patankar,[70] but including the extra terms due to the solid, the exponentials in the east and west coefficients, (a_e and a_w), are approximated as follows.

The east influence coefficient a_E is first divided by D_{l_e} giving,

$$\frac{a_E}{D_{l_e}} = \frac{(F_e/D_{l_e})}{e^{(F_e/D_{l_e})} - 1} + \frac{D_{s_e}}{D_{l_e}}. \tag{22}$$

Next, a local Peclet number is defined for the east face,

$$Pe_e = \frac{u_{l_e} \cdot \delta x_e \cdot (Cp_l\rho_l)_e}{k_{l_e}} = \frac{F_e}{D_{l_e}}, \tag{23a}$$

and is substituted into Eq. (22) giving:

$$\frac{a_E}{D_{l_e}} = \frac{Pe_e}{e^{Pe_e} - 1} + \frac{D_{s_e}}{D_{l_e}}. \tag{23b}$$

A power-law approximation [70] for $\frac{Pe_e}{e^{Pe_e} - 1}$ is:

$$\begin{aligned}
&\frac{Pe_e}{e^{Pe_e} - 1} \approx Pe_e && Pe_e < -10 \\
&\frac{P_e}{e^{Pe_e} - 1} \approx (1 + 0.1Pe_e)^5 - Pe_e && -10 \le Pe_e < 0 \\
&\frac{Pe_e}{e^{Pe_e} - 1} \approx (1 - 0.1Pe_e)^5 && 0 \le Pe_e \le 10 \\
&\frac{Pe_e}{e^{Pe_e} - 1} \approx 0 && Pe_e > 10.
\end{aligned} \tag{24}$$

The above four equations can be condensed to the form

$$\frac{Pe_e}{e^{Pe_e} - 1} \approx [\![0, (1 - 0.1 \mid Pe_e \mid)^5]\!] + [\![0, -Pe_e]\!] \tag{25}$$

where the brackets imply that the maximum value inside should be used.

Substituting into the expression for $\frac{a_E}{D_{l_e}}$ and multiplying by D_{l_e} gives the desired equation for the east influence coefficient,

$$a_E = D_{l_e}[\![0, (1 - 0.1 \mid Pe_e \mid)^5]\!] + [\![0, -F_e]\!] + D_{s_e}. \tag{26}$$

For the west influence coefficient, a_W, a similar substitution yields,

$$a_W = D_{l_w}[\![0,(1-0.1\mid Pe_w\mid)^5]\!] + [\![0,+F_w]\!] + D_{s_w}. \tag{27}$$

Conservation of Energy: Final 2-D Discretization Equation

With the power-law expressions for the fluxes, the conservation equation can be written in the final two-dimensional form used in the code:

$$a_P T_P = a_E T_E + a_W T_W + a_N T_N + a_S T_S + a_P^0 T_P^0 + b \tag{28a}$$

where the influence coefficients are

$$\begin{aligned}
a_E &= D_{l_e}[\![0,(1-0.1\mid Pe_e\mid)^5]\!] + [\![0,-F_e]\!] + D_{s_e} \\
a_W &= D_{l_w}[\![0,(1-0.1\mid Pe_w\mid)^5]\!] + [\![0,+F_w]\!] + D_{s_w} \\
a_N &= D_{l_n}[\![0,(1-0.1\mid Pe_n\mid)^5]\!] + [\![0,-F_n]\!] + D_{s_n} \\
a_S &= D_{l_s}[\![0,(1-0.1\mid Pe_s\mid)^5]\!] + [\![0,+F_s]\!] + D_{s_s} \\
a_P &= a_E + a_W + a_N + a_S + (F_e - F_w + F_n - F_s)) \\
&\quad + \frac{\Delta x \Delta y}{\Delta t}\left[\rho_l C p_l g_l + \rho_s C p_s (1-g_l)\right] - S_p \\
a_P^0 &= \frac{\Delta x \Delta y}{\Delta t}\left[\rho_l^0 C p_l^0 g_l^0 + \rho_s^0 C p_s^0 (1-g_l^0)\right].
\end{aligned} \tag{28b}$$

The source term is

$$\begin{aligned}
b &= S_c + T_0 \cdot \left[(\rho_l C p_l g_l + \rho_s C p_s g_s) - (\rho_l^0 C p_l^0 g_l^0 + \rho_s^0 C p_s^0 g_s^0)\right] \frac{\Delta x \Delta y}{\Delta t} \\
&\quad + T_0 \cdot (F_e - F_w + F_n - F_s) \\
&\quad + \frac{\Delta x \Delta y}{\Delta t} \cdot \left(L - \frac{\partial h_s}{\partial C_s} \cdot (C_s - C_{\text{ref}})\right) \cdot (\rho_s g_s - \rho_s^0 g_s^0).
\end{aligned} \tag{28c}$$

The modified Peclet numbers are

$$\begin{aligned}
Pe_e &= F_e / D_{l_e} \\
Pe_w &= F_w / D_{l_w} \\
Pe_n &= F_n / D_{l_n} \\
Pe_s &= F_s / D_{l_s}.
\end{aligned} \tag{28d}$$

The modified mass fluxes are

$$\begin{aligned} F_e &= (\Delta y \cdot g_{l_e} \cdot u_e \cdot \rho_{l_{\text{up}}}) \cdot Cp_{l_{\text{up}}} \\ F_w &= (\Delta y \cdot g_{l_w} \cdot u_w \cdot \rho_{l_{\text{up}}}) \cdot Cp_{l_{\text{up}}} \\ F_n &= (\Delta x \cdot g_{l_n} \cdot v_n \cdot \rho_{l_{\text{up}}}) \cdot Cp_{l_{\text{up}}} \\ F_w &= (\Delta x \cdot g_{l_w} \cdot v_s \cdot \rho_{l_{\text{up}}}) \cdot Cp_{l_{\text{up}}}, \end{aligned} \tag{28e}$$

and the diffusive flux coefficients are

$$\begin{aligned} D_{l_e} &= \frac{\Delta y \cdot g_{l_e} \cdot k_{l_e}}{\delta x_e}, & D_{s_e} &= \frac{\Delta y \cdot (1 - g_{l_e}) \cdot k_{s_e}}{\delta x_e} \\ D_{l_w} &= \frac{\Delta y \cdot g_{l_w} \cdot k_{l_w}}{\delta x_w}, & D_{s_w} &= \frac{\Delta y \cdot (1 - g_{l_w}) \cdot k_{s_w}}{\delta x_w} \\ D_{l_n} &= \frac{\Delta x \cdot g_{l_n} \cdot k_{l_n}}{\delta y_n}, & D_{s_n} &= \frac{\Delta x \cdot (1 - g_{l_n}) \cdot k_{s_n}}{\delta y_n} \\ D_{l_s} &= \frac{\Delta x \cdot g_{l_s} \cdot k_{l_s}}{\delta y_s}, & D_{s_s} &= \frac{\Delta x \cdot (1 - g_{l_s}) \cdot k_{s_s}}{\delta y_s}. \end{aligned} \tag{28f}$$

Conservation of Energy: Additional Sources

The above equation set is the final form used in the model. The presence of the source terms, S_c and S_p, allows one to include additional effects.

Mass Addition: One capability provided by the source term is the ability to account for energy supplied by mass addition. This is critical in the current application since mass is added to the computational region. This mass addition is necessitated by the density changes inherent in the physical experiment. In the laboratory, mass is added via a supply tube. In the model, the mass and corresponding energy addition are accounted for via the S_c source term. The mass entering the domain is assumed to carry an enthalpy approximately equal to the cell enthalpy of the previous time step. Accordingly, the source term, S_c, in Eq. (28) is supplemented as follows:

$$S_c = S_c + h^\circ \cdot \dot{m}, \tag{29}$$

where h° is the previous time step cell enthalpy and $\dot{m}$ is the mass gain per second.

Newton Cooling: The source terms S_c and S_p can also be used to approximate the effect of heat loss to the external environment. In this case, the energy lost from a control cell is based on its exposed surface area, the temperature difference between its own temperature, T, and the ambient, T_{room}, and a heat loss coefficient, h_{coef}. This newton cooling effect is applied on all external cell faces. The specific term is as follows:

$$S_p T + S_c = -h_{\text{coef}} \cdot \text{area} \cdot T + h_{\text{coef}} \cdot \text{area} \cdot T_{\text{room}}. \tag{30}$$

Error Correction: The source term can also be used as a convenient means of correcting the false energy source introduced by continuity errors. Since the velocity field is also part of the iterative solution, continuity errors necessarily occur. The effect on the energy equation can be illustrated by the following example. Given a constant temperature flow field without any phase change, the temperature should remain constant throughout the field. However, if there is a perceived mass influx due to a continuity error, that mass error carries enthalpy with it and the conservation of energy will respond to the corresponding influx of energy by raising the average cell temperature, compounding a continuity error into an energy error. The conventional solution[70] to this problem is to subtract the continuity equation multiplied by the temperature from the energy equation during the derivation of the discretization equations; thus, eliminating the flux terms from the discretized equations. For a two-phase problem, the inclusion of a continuity error correction term is not as straightforward. The main difficulty is that the average enthalpy term is not a simple function of the temperature but also depends on the amount of solidification. The approach adopted here was to include this error correction term in the S_c source term.

The first step is to determine the continuity error for the cell,

$$\frac{\Delta x \Delta y}{\Delta t}\left[(\rho_l^0 g_l^0 + \rho_s^0 g_s^0) - (\rho_l g_l + \rho_s g_s)\right] - \text{Flux}_e + \text{Flux}_w - \text{Flux}_n + \text{Flux}_s + S_{\text{mass}} = \text{Mass}_{\text{error}} \tag{31}$$

where S_{mass} is a legitimate mass source for the cell (e.g., at the supply tube) but $\text{Mass}_{\text{error}}$ represents an unaccounted gain of mass. As a first approximation, this mass error is assumed to be gained at the previous time step liquid enthalpy. In order to compensate for this error, the erroneous source is subtracted via the source term:

$$S_c = S_c - h_l^0 \cdot \text{Mass}_{\text{error}} \tag{32}$$

Conservation of Solute

Conservation of Solute: Basic Equation

The conservation of solute (water) for the binary solution[66] is expressed as:

$$\frac{\partial}{\partial t}(g_l \rho_l C_l + g_s \rho_s C_s) + \nabla \cdot \left[g_l \rho_l \vec{V}_l C_l + g_s \rho_s \vec{V}_s C_s\right] = \nabla \cdot \left[g_s \rho_s D_s \nabla C_s + g_l \rho_l D_l \nabla C_l\right]. \tag{33}$$

Assuming that the solid is rigid, ($\vec{V}_s = 0$), and rearranging terms gives the solutal equation used in the numerical code,

$$\frac{\partial}{\partial t}(g_l \rho_l C_l) + \nabla \cdot \left[g_l \rho_l \vec{V}_l C_l\right] = \nabla \cdot \left[g_l \rho_l D_l \nabla C_l\right] + \nabla \cdot \left[g_s \rho_s D_s \nabla C_s\right] - \frac{\partial}{\partial t}(g_s \rho_s C_s) \tag{34}$$

where C_l and C_s are the weight percent of water in the liquid and in the solid, respectively. The diffusivity of water in the liquid and in the solid are given by D_l and D_s.

Conservation of Solute: Control Volume Expression

The partial differential conservation equation for solute is integrated over the same control volume as the energy equation (Fig. III–1). The resulting equation for the volume centered around point 'P' is:

$$\frac{\Delta x \Delta y}{\Delta t}\left[(\rho_l C_l g_l + \rho_s C_s g_s) - (\rho_l^0 C_l^0 g_l^0 + \rho_s^0 C_s^0 g_s^0)\right] + J_e - J_w + J_n - J_s = S\Delta x \Delta y \tag{35}$$

where, for example, the solutal flux at the east face (having substituted the general diffusive coefficient Γ in for D) is,

$$J_e = F_e C_{l_e} - \Delta y \cdot g_{l_e} \rho_{l_e} \Gamma_{l_e} \left(\frac{\partial C_l}{\partial x}\right)_{l_e} - \Delta y \cdot g_{s_e} \rho_{s_e} \Gamma_{s_e} \left(\frac{\partial C_s}{\partial x}\right)_{s_e} \tag{36}$$

and F_e is the actual mass flux at the east face,

$$F_e = \text{Flux}_e = \Delta y \cdot g_{l_e} \rho_{l_e} u_{l_e} \tag{37}$$

and

$$S\Delta x \Delta y = S_p C_l + S_c. \tag{38}$$

At this stage in the derivation, the source term for the solutal equation is much simpler than that for the conservation of energy formulation and only includes the additional terms, $S_p C_l$ and S_c, which are added to account for external sources of solute. As with the energy equation, these external source terms are used to account for the mass source introduced by a supply tube, and also to compensate for continuity errors which occur during the iteration process. The source term does not remain this simple. Eventually, all of the terms which do not contain the dependent variable C_l are collected on the right-hand side of the equation and considered as an effective source term.

Conservation of Solute: Assumptions

As with the energy equation, some assumption must be made in order to express the conservation in terms of the 'known' values at the cell nodes. One assumption for this particular NH_4Cl and H_2O system is that diffusion in the solid is negligible, thereby eliminating the solid diffusion contribution to the flux terms in Eq. (35). The remaining parameters which need to be approximated at the cell faces are F, J, C_l, ρ_l, Γ_l, and $\left(\frac{\partial C_l}{\partial x}\right)$. The approximations used are the same as for temperature. The mass flux, F, is based on upwind values. The density and Γ pair in the diffusion term is computed using harmonic averaging, and the net liquid solutal flux at a cell face is based on the one-dimensional steady state solution for the solutal transport between two points with fixed velocity and a constant diffusion coefficient. A summary of these assumptions is given in Fig. III–5:

1) The diffusivity in the liquid is evaluated by harmonic averaging:

$$\Gamma_{l_e} = \frac{\Gamma_{l_P}\Gamma_{l_E}}{\Gamma_{l_P} + \Gamma_{l_E}} \qquad \text{(uniform grid)}$$

2) The solid solutal diffusivity is assumed to be negligible:

$$\Gamma_s = 0$$

3) The density in the diffusion term is evaluated by harmonic averaging:

$$\rho_{l_e} = \frac{\rho_{l_P}\rho_{l_E}}{\rho_{l_P} + \rho_{l_E}} \qquad \text{(uniform grid)}$$

4) The density in the mass flux term is upwinded:

$$\rho_{l_e} = \rho_{l_{up}}.$$

Figure III–5. Discretized solutal equation assumptions

Conservation of Solute: Discretized Fluxes

As with the energy equation, the flux terms in the solutal Eq. (35) are approximated based on a one-dimensional solution. The above assumptions are first incorporated into the definition of the diffusive flux coefficients:

$$\begin{aligned} D_{l_e} &= \frac{\Delta y \cdot g_{l_e} \cdot \rho_{l_e} \Gamma_{l_e}}{\delta x_e}, & D_{s_e} &= 0 \\ D_{l_w} &= \frac{\Delta y \cdot g_{l_w} \cdot \rho_{l_w} \Gamma_{l_w}}{\delta x_w}, & D_{s_w} &= 0 \\ D_{l_n} &= \frac{\Delta x \cdot g_{l_n} \cdot \rho_{l_n} \Gamma_{l_n}}{\delta y_n}, & D_{s_n} &= 0 \\ D_{l_s} &= \frac{\Delta x \cdot g_{l_s} \cdot \rho_{l_s} \Gamma_{l_s}}{\delta y_s}, & D_{s_s} &= 0. \end{aligned} \tag{39}$$

With these coefficients and some regrouping, the solutal conservation equation [Eq. (35)] can be simplified to,

$$\frac{\Delta x \Delta y}{\Delta t} \left[(\rho_l C_l g_l) - (\rho_l^0 C_l^0 f_l^0) \right]_P + J_e - J_w + J_n - J_s - C_{l_P} S_P = b \tag{40a}$$

where the flux terms no longer include diffusion in the solid, e.g.,

$$J_e = F_e C_{l_e} - D_{l_e} \cdot \delta x_e \cdot \left(\frac{\partial C_l}{\partial x} \right)_e \tag{40b}$$

and the right-hand side is:

$$b = S_c + \frac{\Delta x \Delta y}{\Delta t} \left[(\rho_s^0 C_s^0 f_s^0) - (\rho_s C_s f_s) \right]_P . \tag{40c}$$

The variable 'b' represents the collection of all those terms in the conservation equation that do not include the dependent variable (C_l). The flux terms in Eq. (40) are of the same form as those in the energy equation except there are no solid diffusion terms. By analogy, the flux of solute in the liquid at the east face of a numerical control volume in based on the steady state flow between two points:

$$J_{l_e} = F_e \left[C_{l_P} - \frac{C_{l_E} - C_{l_P}}{e^{(F_e / D_{l_e})} - 1} \right] . \tag{41}$$

Continuing the derivation gives a combined solutal flux at the east face,

$$J_e = J_{l_e} = F_e C_{l_P} + \left[\frac{F_e}{e^{(F_e/D_{l_e})} - 1}\right] C_{l_P} - \left[\frac{F_e}{e^{(F_e/D_{l_e})} - 1}\right] C_{l_E} \tag{42}$$

and a combined solutal flux at the west face,

$$J_w = J_{l_w} = F_w C_{l_W} + \left[\frac{F_w}{e^{(F_w/D_{l_w})} - 1}\right] C_{l_W} - \left[\frac{F_w}{e^{(F_e/D_{l_w})} - 1}\right] C_{l_P}. \tag{43}$$

Using these expressions for the fluxes, a one-dimensional discretized conservation of solute equation can be derived for a point P by substituting into Eq. (40) giving:

$$a_P C_{l_P} = a_E C_{l_E} + a_W C_{l_W} + a_P^0 C_{l_P}^0 + b \tag{44a}$$

where

$$\begin{aligned}
a_P &= a_E + a_W + (F_e - F_w) + \frac{\Delta x \Delta y}{\Delta t}(\rho_l g_l)_P - S_P \\
a_E &= \frac{F_e}{e^{(F_e/D_{l_e})} - 1} \\
a_W &= \frac{F_w}{e^{(F_w/D_{l_w})} - 1} + F_w \\
a_P^0 &= \frac{\Delta x \Delta y}{\Delta t}\left(\rho_l^0 g_l^0\right)_P \\
b &= S_C + \frac{\Delta x \Delta y}{\Delta t}\left[\rho_s^0 C_s^0 f_s^0 - \rho_s C_s f_s\right]_P .
\end{aligned} \tag{44b}$$

Again, the exponential terms in the link coefficients, a_e and a_w, are to be approximated by the power-law approximation. Using the east face as an example, coefficient a_E is first divided by D_{l_e} giving

$$\frac{a_E}{D_{l_e}} = \frac{(F_e/D_{l_e})}{e^{(F_e/D_{l_e})} - 1}. \tag{45}$$

Defining a Peclet number,

$$Pe_e = \frac{u_{l_e}\delta x_e}{\Gamma_{l_e}} = \frac{F_e}{D_{l_e}} \tag{46}$$

gives,

$$\frac{a_E}{D_{l_e}} = \frac{Pe_e}{e^{Pe_e} - 1}. \tag{47}$$

As with the energy equation, $\frac{Pe_e}{e^{Pe_e} - 1}$ can be approximated as,

$$\frac{Pe_e}{e^{Pe_e} - 1} \approx [\![0, (1 - 0.1 \mid Pe_e \mid)^5]\!] + [\![0, -Pe_e]\!], \tag{48}$$

where the brackets imply the the maximum value inside should be used. Substituting this expression into that for $\frac{a_E}{D_{l_e}}$ and multiplying by D_{l_e} gives,

$$a_E = D_{l_e}[\![0, (1 - 0.1 \mid Pe_e \mid)^5]\!] + [\![0, -F_e]\!]. \tag{49}$$

For the west influence coefficient, a_W, a similar substitution yields,

$$a_W = D_{l_w}[\![0, (1 - 0.1 \mid Pe_w \mid)^5]\!] + [\![0, +F_w]\!]. \tag{50}$$

Conservation of Solute: Final 2-D Discretization Equation

With the power-law approximation for the fluxes, the conservation equation for solute can be written in the final form used in the code:

$$a_P C_{l_P} = a_E C_{l_E} + a_W C_{l_W} + a_N C_{l_N} + a_S C_{l_S} + a_P^0 C_{l_P}^0 + b \tag{51a}$$

where the influence coefficients are

$$\begin{aligned}
a_E &= D_{l_e}[\![0, (1 - 0.1 \mid Pe_e \mid)^5]\!] + [\![0, -F_e]\!] \\
a_W &= D_{l_w}[\![0, (1 - 0.1 \mid Pe_w \mid)^5]\!] + [\![0, +F_w]\!] \\
a_N &= D_{l_n}[\![0, (1 - 0.1 \mid Pe_n \mid)^5]\!] + [\![0, -F_n]\!] \\
a_S &= D_{l_s}[\![0, (1 - 0.1 \mid Pe_s \mid)^5]\!] + [\![0, +F_s]\!] \\
a_P &= a_E + a_W + (F_e - F_w + F_n - F_s) + \frac{\Delta x \Delta y}{\Delta t}(\rho_l g_l)_P - S_P \\
a_P^0 &= \frac{\Delta x \Delta y}{\Delta t}(\rho_l^0 g_l^0)_P,
\end{aligned} \tag{51b}$$

the source term is

$$b = S_C + \frac{\Delta x \Delta y}{\Delta t} \left[\rho_s^0 C_s^0 g_s^0 - \rho_s C_s g_s\right]_P, \tag{51c}$$

the Peclet numbers are

$$\begin{aligned} Pe_e &= F_e / D_{l_e} \\ Pe_w &= F_w / D_{l_w} \\ Pe_n &= F_n / D_{l_n} \\ Pe_s &= F_s / D_{l_s}, \end{aligned} \tag{51d}$$

the mass fluxes are

$$\begin{aligned} F_e &= Flux_e = \Delta y \cdot g_{l_e} \rho_{l_e} u_{l_e} \\ F_w &= Flux_w = \Delta y \cdot g_{l_w} \rho_{l_w} u_{l_w} \\ F_n &= Flux_n = \Delta x \cdot g_{l_n} \rho_{l_n} v_{l_n} \\ F_s &= Flux_s = \Delta x \cdot g_{l_s} \rho_{l_s} v_{l_s}, \end{aligned} \tag{51e}$$

and the diffusive flux coefficients are

$$\begin{aligned} D_{l_e} &= \frac{\Delta y \cdot g_{l_e} \cdot \rho_{l_e} \Gamma_{l_e}}{\delta x_e} \\ D_{l_w} &= \frac{\Delta y \cdot g_{l_w} \cdot \rho_{l_w} \Gamma_{l_w}}{\delta x_w} \\ D_{l_n} &= \frac{\Delta x \cdot g_{l_n} \cdot \rho_{l_n} \Gamma_{l_n}}{\delta y_n} \\ D_{l_s} &= \frac{\Delta x \cdot g_{l_s} \cdot \rho_{l_s} \Gamma_{l_s}}{\delta y_s}. \end{aligned} \tag{51f}$$

Conservation of Solute: Additional Sources

Mass Addition: Mass, $\dot{m}$, is pulled into the physical domain via a supply tube and the associated solute is accounted for via the S_c source term. As an approximation, the mass gained is assumed to have the same solutal concentration as was contained in the supply tube control cell during the previous time step. Accordingly, the source term in Eq. (51) is supplemented at this specific cell using

$$S_c = S_c + C_l^0 \cdot \dot{m}. \tag{52}$$

Error Correction: As with the energy equation, a correction for the continuity error can be introduced via the S_c source term. The mass error for each cell is computed from the continuity equation and then a correction is made based on the assumption the solute has the previous time step value of the cell concentration:

$$S_c = S_c - C_l^0 \cdot \text{Mass}_{\text{error}}. \tag{53}$$

Conservation of Momentum

Conservation of Momentum: Basic Equation

The conservation of momentum equation for the 'u' component of velocity derived by Bennon and Incropera[66] is:

$$\begin{aligned}\frac{\partial}{\partial t}(\rho\overline{u}) + \nabla\cdot(\rho\vec{\overline{V}}\overline{u}) &= \nabla\cdot\left(\sum_k \mu_k \nabla(g_k u_k)\right) \\ &- \nabla\cdot\left(\sum_k \overline{\rho}_k(\vec{V}_k - \vec{\overline{V}})(u_k - \overline{u})\right) - \frac{\partial p}{\partial x} + \rho B_x - \frac{\mu_l}{K_x} g_l(u_l - u_s).\end{aligned} \tag{54}$$

In the above equation, ρ is the average density of the solid-liquid mixture defined by

$$\rho = g_l\rho_l + g_s\rho_s, \tag{55}$$

where g_l is the volume fraction of liquid and ρ_l is the density of the liquid phase isolated from the mixture. The variables, g_s and ρ_s, are the corresponding parameters for the solid. The partial density, $\overline{\rho}_k$, is the density of phase k relative to the mixture and is related to the k–phase density via the volume fraction:

$$\overline{\rho}_k = g_k\rho_k. \tag{56}$$

The 't' in Eq. (54) is time and '$\overline{u}$' is the x–coordinate component of the average velocity, $\vec{\overline{V}}$. This average velocity is defined in terms of the liquid and solid velocity

as:

$$\vec{\overline{V}} = \frac{1}{\rho}\left(\overline{\rho}_l \vec{V}_l + \overline{\rho}_s \vec{V}_s\right). \tag{57}$$

Of the remaining terms, 'μ' stands for the dynamic viscosity,'p', represents the pressure, and 'B_x' is any body force in the x–direction. The last term, $\frac{\mu_l}{K_x} g_l (u_l - u_s)$, is the approximation to the phase interaction force based on Darcy's law with the permeability given by:[66]

$$K_x = K_0 \left[\frac{g_l^3}{(1-g_l)^2}\right]. \tag{58}$$

In a slight deviation from Bennon and Incropera's derivation, the following relationship,

$$\sum_k \overline{\rho}_k \vec{V}_k u_k = (\rho \vec{\overline{V}} \overline{u}) + \left(\sum_k \overline{\rho}_k (\vec{V}_k - \vec{\overline{V}})(u_k - \overline{u})\right) \tag{59}$$

is substituted into Eq. (54) giving

$$\begin{aligned} \frac{\partial}{\partial t}(\rho u) + \nabla \cdot \left(\sum_k \overline{\rho}_k \vec{V}_k u_k\right) &= \nabla \cdot \left(\sum_k \mu_k \nabla (g_k u_k)\right) \\ &\quad - \frac{\partial p}{\partial x} + \rho B_x - \frac{\mu_l}{K_x} g_l (u_l - u_s). \end{aligned} \tag{60}$$

By using this form of the momentum conservation equation, some of Bennon and Incropera's assumptions, such as $\nabla(p/p_l) \approx 0$ and $\nabla \cdot (\rho f_s f_l \vec{V}_r u_r) \approx 0$, are avoided. Taking advantage of the assumption that the solid is rigid, $\vec{V}_s = 0$, the summations in the above equation reduce to single terms containing only the liquid velocity:

$$\frac{\partial}{\partial t}(\rho \overline{u}) + \nabla \cdot \left(\overline{\rho}_l \vec{V}_l u_l\right) = \nabla \cdot (\mu_l \nabla (g_l u_l)) - \frac{\partial p}{\partial x} + \rho B_x - \frac{\mu_l}{K_x} g_l u_l. \tag{61}$$

Using the same assumption of $\vec{V}_s = 0$, together with the definition of the velocity in Eq. (57), the $\rho \overline{u}$ term above can be expressed as $g_l \rho_l u_l$. In addition, $\overline{\rho}$ can be expressed as $\rho_l g_l$ using the definition for $\overline{\rho}_k$ given in Eq. (56). These substitutions

result in the formulation of the conservation of momentum used as the basis of the numerical code:

$$\frac{\partial}{\partial t}(\rho_l g_l u_l) + \nabla \cdot \left(\rho_l g_l \vec{V}_l u_l\right) = \nabla \cdot (\mu_l \nabla(g_l u_l)) - \frac{\partial p}{\partial x} + \rho B_x - \frac{\mu_l}{K_x} g_l u_l. \qquad (62)$$

The conserved variable that is sought in the solution of this equation is not simply u_l but the variable pair $g_l u_l$. This approach fits neatly into the general conservation equation solution scheme,[70] and makes physical sense because $g_l u_l$ represents the total fluid momentum per unit mass in a control volume.

Conservation of Momentum: Control Volume Expression

The differential form of the momentum equation [Eq. (58)] is integrated over a control volume and then discretized to generate a conservation of momentum equation. Unlike the control volumes for energy and solutal concentration, the momentum control volume, outlined by the dashed line, is offset from the main grid, as shown in Figure III–6.

Except for the complication of the offset position of the momentum cell, the conservation of momentum is treated essentially the same as the other conserved quantities and is similar in form to both the thermal and solutal discretized equations with the inclusion of additional source terms. The integrated conservation of momentum for the 'u' velocity is:

$$\frac{\delta x \Delta y}{\delta t}\left[\rho_l g_l u_l - \rho_l^0 g_l^0 u_l^0\right] + J_e - J_w + J_n - J_s = \Delta y(p_w - p_e) + S\delta x \Delta y. \qquad (63a)$$

The J's above are the net flow of momentum across the momentum cell control faces. The net flow of 'u' momentum across the east face is for example:

$$J_e = F_e \cdot (g_l u_l)_e - \Delta y \mu_e \left(\frac{\partial(g_l u_l)}{\partial x}\right)_e, \qquad (63b)$$

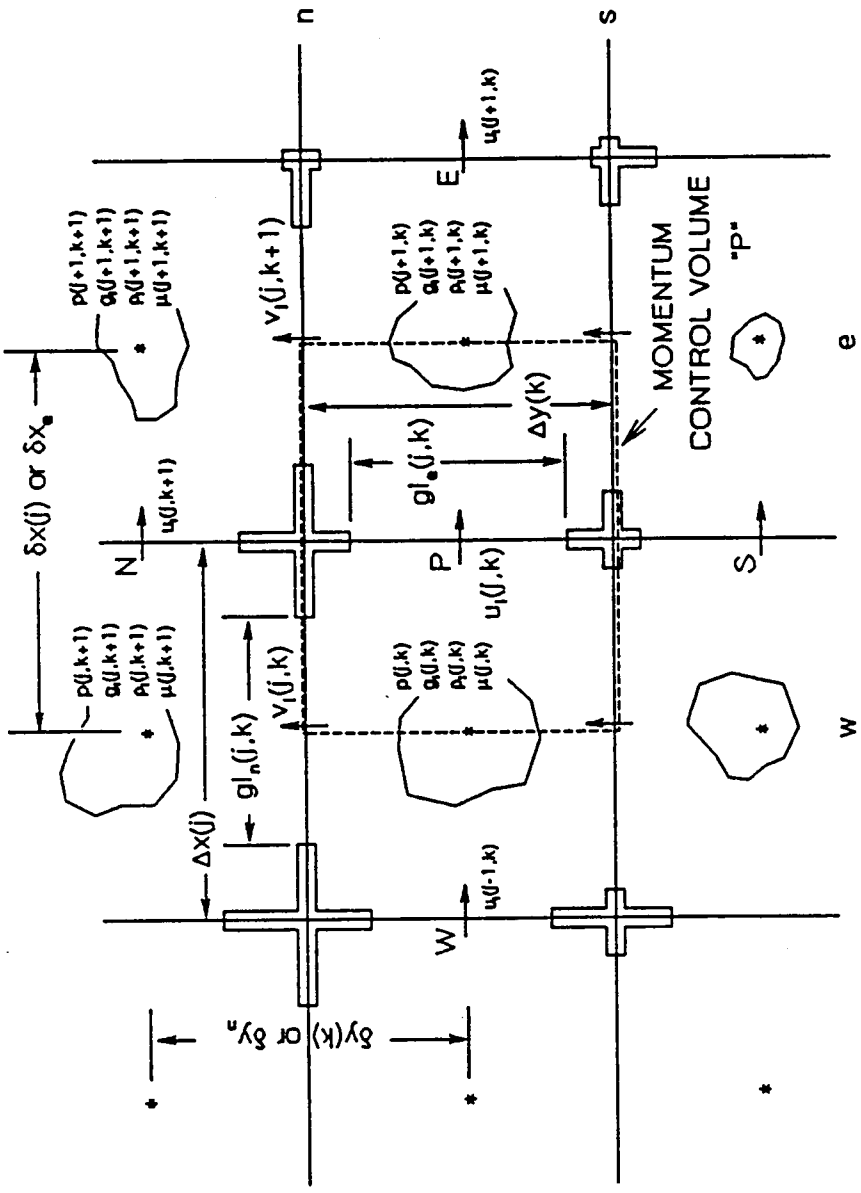

Figure III–6. Momentum control volume

where the term, F_e, is a modified mass flux. It is modified in the sense that it is the flux that would cross a fully open east face with velocity u_l. The actual mass flux would be less, due to the reduced flow area, g_{l_e}, caused by the solid blockage. For computational convenience, this g_{l_e} term is not included with the flux term but is grouped with the dependent variable so that $(g_l u_l)$ can be solved for as a pair. The motivation for this grouping is the presence of $(g_l u_l)$ in the gradient term in Eq. (62) and the desire to preserve the general solution form. With the actual mass flux across a face (east) defined as

$$\text{Flux}_e = \Delta y \rho_{l_e} g_{l_e} u_{l_e}, \tag{63c}$$

the resulting modified flux is:

$$F_e = \frac{\text{Flux}_e}{g_{l_e}} = \frac{\Delta y \rho_{l_e} g_{l_e} u_{l_e}}{g_{l_e}}. \tag{63d}$$

The source term, $S\delta x \Delta y$, in Eq. (63a) is:

$$S\delta x \Delta y = \rho B_x \delta x \Delta y - \frac{\mu_l}{K_x}(g_l u_l)\delta x \Delta y + S_p \cdot (g_l u_l) + S_c. \tag{63e}$$

In addition to the body force and Darcy friction, the source terms, $S_p \cdot (g_l u_l)$ and S_c, have been added to account for any other external sources of momentum for the cell. In the current version of the code, these extra source terms are not used, but are programmed for the sake of completeness.

Conservation of Momentum: Interpolations and Assumptions

Due to the offset grid, the interpolations needed before applying the above conservation of momentum equation are more complicated than those for the other conservation equations. Figure III–6 provides the grid notation. The rectangle outlined by the dotted line is the (j,k) u–momentum control volume. The main

grid, corresponding to the thermal and solutal control volumes is indicated by the solid lines.

The modified fluxes at the east and west faces of the u–momentum control cell (F_e and F_w, respectively) must be interplolated based on 'known' velocities corresponding to the centers of the momentum cells and 'known' densities corresponding to the center of the main grid cells. This interplotation is done using harmonic averaging[70] as follows:

$$F_e = \text{harmonic average of} \quad \left(\frac{\text{Flux}_{e_{(j,k)}}}{gl_{e_{(j,k)}}} \quad \text{and} \quad \frac{\text{Flux}_{e_{(j+1,k)}}}{gl_{e_{(j+1,k)}}} \right) \tag{64a}$$

$$F_w = F_{e_{(j-1,k)}},$$

where

$$\text{Flux}_{e_{(j,k)}} = \Delta y_{(k)} \cdot \rho_{l_{\text{up}}} \cdot (gl_{e_{(j,k)}} \cdot u_{l_{(j,k)}}). \tag{64b}$$

The modified flux at the north face of the u–momentum control cell must also be computed and is the sum of the appropriate flux from the north faces of the two main grid control volumes which overlay the momentum control volume:

$$F_n = \frac{1}{2}\left[\frac{\text{Flux}_{n_{(j,k)}}}{gl_{n_{(j,k)}}}\right] + \frac{1}{2}\left[\frac{\text{Flux}_{n_{(j+1,k)}}}{gl_{n_{(j+1,k)}}}\right] \tag{65a}$$

$$F_s = F_{n_{(j,k-1)}}$$

where

$$\text{Flux}_{n_{(j,k)}} = \Delta x_{(j)} \cdot \rho_{l_{\text{up}}} \cdot (gl_{n_{(j,k)}} \cdot v_{l_{(j,k)}}). \tag{65b}$$

The diffusion flux coefficients are similar to those defined for the other conservation equations, but require more algebra. For the east and west face of the u–momentum cell, the diffusion flux coefficients are directly related to the viscosities stored at the momentum cell faces. The north and south diffusion flux coefficients, however, must be averaged, based on the overlapping main grid cells

and interpolated viscosities, i.e.:

$$
\begin{aligned}
D_{l_e} &= \frac{\Delta y_{(k)} \Gamma_{l_{e(j+1,k)}}}{\Delta x_{(j+1)}} \\
D_{l_w} &= D_{l_{e(j-1,k)}} \\
D_{l_n} &= \frac{\frac{1}{2}\left[\Delta x_{(j)} \Gamma_{l_{n(j,k)}}\right] + \frac{1}{2}\left[\Delta x_{(j+1)} \cdot \Gamma_{l_{n(j+1,k)}}\right]}{\delta y_{(k)}} \\
D_{l_s} &= D_{l_{n(j,k-1)}}
\end{aligned}
\tag{66a}
$$

where

$$
\begin{aligned}
\Gamma_{l_{e(j+1,k)}} &= \mu_{(j+1,k)} \\
\Gamma_{l_{n(j,k)}} &= \text{harmonic average of} \quad \left(\mu_{(j,k)} \quad \text{and} \quad \mu_{(j,k+1)}\right).
\end{aligned}
\tag{66b}
$$

One implication of the above north/south harmonic average of the viscosity Γ_{l_n} at the north (south) face of the u–momentum cell face is that at a boundary the boundary cell viscosity has an influence on the effect of the boundary shear. With harmonic averaging, setting the boundary viscosity to zero (e.g., in the quartz), results in zero shear at the wall. The correct viscosity for a solid wall is, instead, an infinite solid viscosity in the boundary cell. Density interpolation involving the boundary cell are also required for the flux across the boundaries; but, these terms are inconsequential in this application since these boundary fluxes are explicitly set to zero. One remaining interpolation needed in Eq. (66*a*) is for the the density at the cell center, ρ_{l_P}, since it is not directly available. This u–momentum cell density is calculated as the arithmetic average of the density values to the east and west.

Conservation of Momentum: Discretized Fluxes

If the diffusion flux coefficients defined above [Eq. (66*a*)] are substituted into the definition of the net flux such as that for the flux across the east face of the

u–momentum cell [Eq. (63b)], the result is an equation of the form:

$$J_e = F_e \cdot (g_l u_l)_e - D_{l_e} \cdot \Delta x \left(\frac{\partial (g_l u_l)}{\partial x} \right)_e . \tag{67}$$

This equation has the basic form:

$$J_l(x) = K_1 \cdot (g_l u_l) - K_2 \left(\frac{\partial (g_l u_l)}{\partial x} \right). \tag{68}$$

This form is similar to the flux equations for the other conserved quantities [Eq. (13)], and the resulting discretized equations are also similar. This set of finalized two-dimensional discretized momentum equations is provided in the next section.

Conservation of Momentum: Final Discretized 2-d Equations

Defining an effective velocity component 'u' as:

$$u = g_l u_l, \tag{69}$$

and using the one-dimensional approximation for the fluxes referred to above, the x–direction momentum equation at a point, P, can be expressed in terms of a source term, a pressure term, and the influence of its four nearest neighbors as:

$$a_P u_P = a_E u_E + a_W u_W + a_N u_N + a_S u_S + b + \text{area} \cdot (p_w - p_e). \tag{70}$$

The coefficients a_{u_P}, a_{u_E}, a_{u_W}, a_{u_N}, and a_{u_S} are referred to as the u-momentum link coefficients since they link the velocity at point 'P' to the neighboring values of velocity. Using the code notation for the staggered grid and the additions of the subscript, u, to denote that these are the momentum link coefficients for the 'u' velocity component, the notation for this equation becomes:

$$\begin{aligned} a_{u_P} u_{(j,k)} = a_{u_E} u_{(j+1,k)} + a_{u_W} u_{(j-1,k)} + a_{u_N} u_{(j,k+1)} + a_{u_S} u_{(j,k-1)} \\ + b_{u_{(j,k)}} + \Delta y_{(k)} \cdot (p_{(j,k)} - p_{(j+1,k)}) \end{aligned} \tag{71}$$

where j, k are the indices for the two dimensional variable arrays. In the above equation, each $u_{(j,k)}$ has its own set of momentum link coefficients which, based on the power law scheme, are defined as follows:

$$\begin{aligned}
a_{u_P} &= a_{u_E} + a_{u_W} + a_{u_N} + a_{u_S} + (F_e - F_w + F_n - F_s) \\
&\quad + \frac{\delta x_{(j)} \Delta y_{(k)}}{\Delta t} \left[\rho_{l_p} \cdot g_{le_{(j,k)}}\right] - \left(S_{P_{(j,k)}} - \frac{\mu_l}{K_x} \delta x \Delta y\right) \\
a_{u_E} &= D_{l_e} [0, (1 - 0.1 \mid Pe_e \mid)^5] + [0, -F_e] \\
a_{u_W} &= D_{l_w} [0, (1 - 0.1 \mid Pe_w \mid)^5] + [0, +F_w] \\
a_{u_N} &= D_{l_n} [0, (1 - 0.1 \mid Pe_n \mid)^5] + [0, -F_n] \\
a_{u_S} &= D_{l_s} [0, (1 - 0.1 \mid Pe_s \mid)^5] + [0, +F_s] \\
a^0_{u_P} &= \frac{\delta x_{(j)} \Delta y_{(k)}}{\Delta t} \left[\rho^0_{l_p} \cdot g^0_{le_{(j,k)}}\right] \\
b &= a^0_{u_P} \cdot u_{old} + \left(S_{c_{(j,k)}} + \rho B_x \delta x \Delta y\right),
\end{aligned} \tag{72a}$$

and where the modified Peclet numbers are

$$\begin{aligned}
Pe_e &= F_e / D_{l_e} \\
Pe_w &= F_w / D_{l_w} \\
Pe_n &= F_n / D_{l_n} \\
Pe_s &= F_s / D_{l_s},
\end{aligned} \tag{72b}$$

based on the definitions of the modified fluxes, F's, and diffusion coefficients, D_l's, given in Eqs. (64), (65), and (66).

For the upwind scheme the above coefficients reduce to:

$$\begin{aligned}
a_{u_P} &= a_{u_E} + a_{u_W} + a_{u_N} + a_{u_S} + (F_e - F_w + F_n - F_s) \\
&\quad + \frac{\delta x_{(j)} \Delta y_{(k)}}{\Delta t} \left[\rho_{l_p} \cdot g_{le_{(j,k)}}\right] - \left(S_{P_{(j,k)}} - \frac{\mu_l}{K_x} \delta x \Delta y\right)
\end{aligned}$$

$$
\begin{aligned}
a_{u_E} &= D_{l_e} + [0, -F_e] \\
a_{u_W} &= D_{l_w} + [0, +F_w] \\
a_{u_N} &= D_{l_n} + [0, -F_n] \\
a_{u_S} &= D_{l_s} + [0, +F_s] \\
a^0_{u_P} &= \frac{\delta x_{(j)} \Delta y_{(k)}}{\Delta t} \left[\rho^0_{l_P} \cdot g l^0_{e_{(j,k)}} \right] \\
b &= a^0_{u_P} \cdot u^0 + \left(S_{c_{(j,k)}} + \rho B_x \delta x \Delta y \right).
\end{aligned}
\tag{73}
$$

Conservation of Momentum: Additional Sources

Two sources of momentum have already been included in the formulation of the discretization equations provided in Eqs. (72) and (73). These sources are the Darcy friction, $\frac{\mu_l}{K_0}(g_l u_l)\delta x \Delta y$, and the body force term, $\rho B_x \delta x \Delta y$. The value of the constant, K_0, used in this study[67] is 5.56×10^7 cm^2. One note concerning the body force term is that in the FTM the density in this term is assumed to be the liquid density, as opposed to the average density as derived in the Bennon and Incropera formulation,[66] [Eqs. (54) and (55)]. The use of an average density would be necessary if the solid moved with the fluid, but is not required in the current study.

An additional, potential source of momentum is the fluid entering the cuvette from the supply tube. However, since this flux is normal to the two-dimensional plane modeled by the FTM, it does not introduce any significant u or v momentum into the domain. Accordingly, the momentum source at the supply tube is set to zero. The result is that the mass from the tube enters the solution domain with no u or v velocity and is accelerated to the local velocity.

Conservation of Momentum: Velocity Corrections

The above derivation has provided a conservation of momentum equation that includes an additional unknown, the pressure field. Accordingly, a relationship between the pressure and velocity must be established before the system of equations can be solved.[70] Given the best estimate of the pressure field, p^*, an estimated velocity field, u^*, is calculated which satisfies Eq. (71) from:

$$a_{u_P} u^*_{(j,k)} = \sum a_{u_{nb}} u^*_{nb} + b_u + \Delta y \cdot (p^*_{(j,k)} - p^*_{(j+1,k)}), \tag{74}$$

where the subscript 'nb' is shorthand for the neighboring points. The solution to the above does not necessarily satisfy conservation of mass. The true pressure, p, that satisfies both conservation of momentum and mass can be expressed in terms of a pressure correction as $p = p^* + p'$ and the corresponding correct velocities, u's, can be expressed as $u = u^* + u'$, where p' and u' indicate the pressure and velocity corrections to the original estimates. Substituting the expressions for p and u into the momentum Eq. (71) and subtracting Eq. (74) for the starred quantities gives

$$a_{u_P} u'_{(j,k)} = \sum a_{u_{nb}} u'_{nb} + \Delta y \cdot (p'_{(j,k)} - p'_{(j+1,k)}). \tag{75}$$

Neglecting the $\sum a_{u_{nb}} u'_{nb}$ and dividing by a_{u_P} yields

$$\begin{aligned} u_{(j,k)} &\approx u^*_{(j,k)} + d_e(p'_{(j,k)} - p'_{(j+1,k)}) \\ d_e &= \frac{\Delta y_{(k)}}{a_{u_P}}. \end{aligned} \tag{76}$$

The neighboring correction terms, $\sum a_{u_{nb}} u'_{nb}$, are neglected since as a correction they will converge to zero. This equation is the basis of the velocity/pressure correction relationship used in the original 'SIMPLE' algorithm development by Patankar.[70] Since in the initial stages of iterating to a solution, the neighboring corrections may not be small, Van Doormaal and Raithby[71] recommended a modified algorithm, SIMPLE-C, in which the $\sum a_{u_{nb}} u'_{(j,k)}$ is subtracted from both

sides of Eq. (75), and then the term $\sum a_{u_{nb}} u'_{nb} - \sum a_{u_{nb}} u'_{(j,k)}$ is neglected instead of $\sum a_{u_{nb}} u'_{nb}$ to obtain a better initial approximation of the velocity as a function of pressure correction as follows:

$$\begin{aligned} u_{(j,k)} &\approx u^*_{(j,k)} + d_e(p'_{(j,k)} - p'_{(j+1,k)}) \\ d_e &= \left(\frac{\Delta y_{(k)}}{a_{u_P} - \sum a_{u_{nb}}}\right). \end{aligned} \tag{77}$$

The only difference between the Doormaal and Raithby and the Patankar expression [Eq. (75)], is in the definition of the d_e term. (This modification is coded into the FTM but is not used for the calculations presented in the current work.)

Equation (77) provides a means of correcting the velocity field based on the pressure corrections. First, however, the pressure correction field must be determined via the continuity equations.[70] The continuity equation for the pressure control volume is shown in Fig. III–7.

Conservation of Momentum: Pressure Correction Equation

The continuity equation for this volume is:

$$\begin{aligned} &\frac{\Delta x \Delta y}{\Delta t}\left[(\rho_l g_l + \rho_s(1-g_l)) - (\rho_l^0 g_l^0 + \rho_s^0(1-g_l^0))\right] - S_{\text{mass}} \\ &\quad + \left[\rho_{l_{\text{up}}} u_e - \rho_{l_{\text{up}}} u_w\right]\Delta y + \left[\rho_{l_{\text{up}}} v_n - \rho_{l_{\text{up}}} v_s\right]\Delta x = 0. \end{aligned} \tag{78}$$

Substituting $u_e = u_{(j,k)} = u^*_{e_{(j,k)}} + d_e(p'_{(j,k)} - p'_{(j+1,k)})$ and similar expressions from Eq. (77) into the above continuity Eq. (78), gives,

$$\begin{aligned} &\frac{\Delta x \Delta y}{\Delta t}\left[(\rho_l g_l + \rho_s(1-g_l)) - (\rho_l^0 g_l^0 + \rho_s^0(1-g_l^0))\right] - S_{\text{mass}} \\ &\quad + \left[\rho_{l_{\text{up}}} u^*_e - \rho_{l_{\text{up}}} u^*_w\right]\Delta y + \left[\rho_{l_{\text{up}}} v^*_n - \rho_{l_{\text{up}}} v^*_s\right]\Delta x \\ &\quad + \left[\rho_{l_{\text{up}}} d_e p'_P - \rho_{l_{\text{up}}} d_e p'_E\right]\Delta y - \left[\rho_{l_{\text{up}}} d_w p'_W - \rho_{l_{\text{up}}} d_w p'_P\right]\Delta y \\ &\quad + \left[\rho_{l_{\text{up}}} d_n p'_P - \rho_{l_{\text{up}}} d_n p'_N\right]\Delta x - \left[\rho_{l_{\text{up}}} d_s p'_S - \rho_{l_{\text{up}}} d_s p'_P\right]\Delta x = 0. \end{aligned} \tag{79}$$

The above can be regrouped to give the familiar form,

$$a_P P'_P = a_E P'_E + a_W P'_W + a_N P'_N + a_S P'_S + b \tag{80a}$$

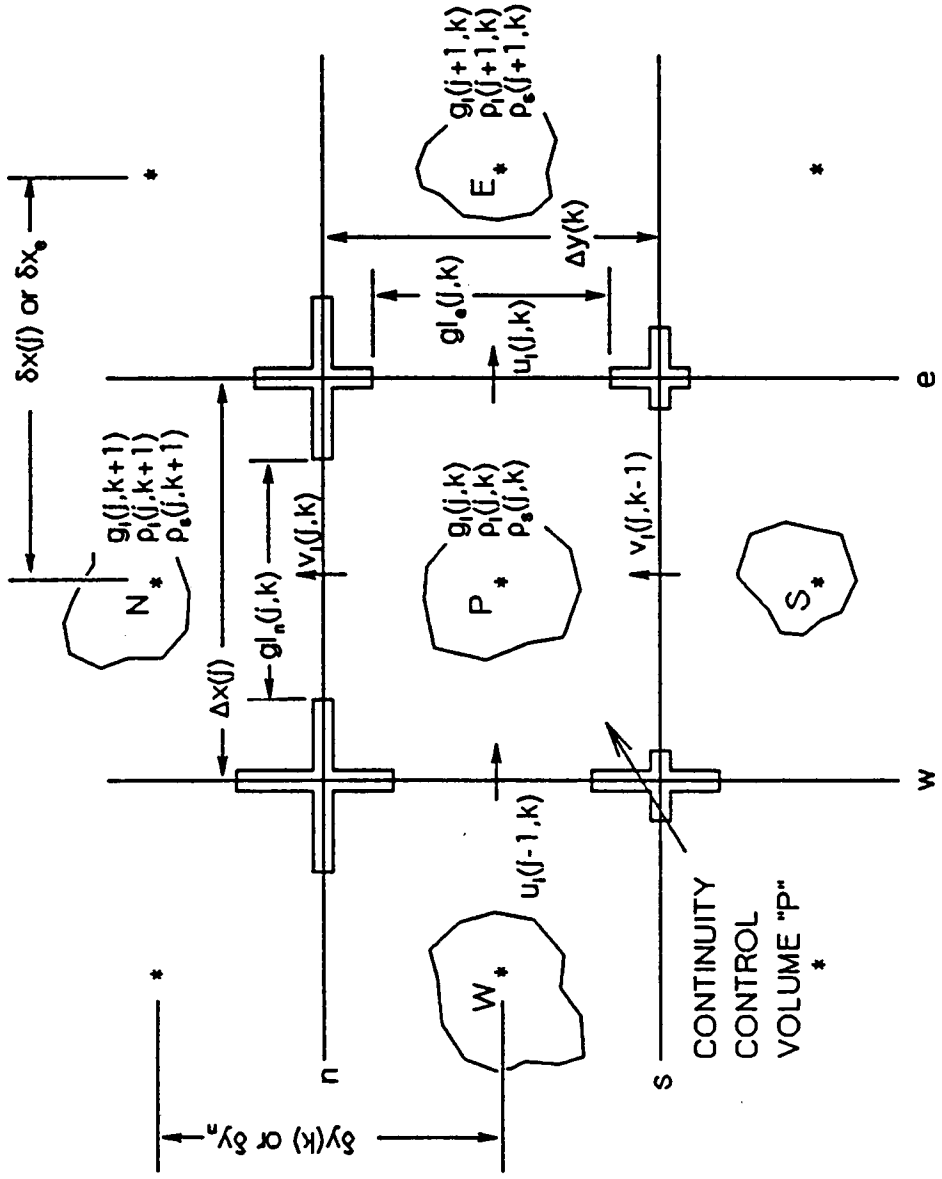

Figure III–7. Pressure control volume

where

$$\begin{aligned} a_P &= a_E + a_W + a_N + a_S \\ a_E &= \rho_{l_{\text{up}}} d_e \cdot g_{l_e} \cdot \Delta y, \qquad d_e = \frac{\Delta y_{(k)}}{(a_{u_P} - \sum a_{u_{nb}})} \\ a_W &= a_{E_{(j-1,k)}} \\ a_N &= \rho_{l_{\text{up}}} d_n \cdot g_{l_n} \cdot \Delta x, \qquad d_n = \frac{\Delta x_{(j)}}{(a_{v_P} - \sum a_{v_{nb}})} \\ a_S &= a_{N_{(j,k-1)}} \end{aligned} \tag{80b}$$

and

$$\begin{aligned} b = \frac{\Delta x \Delta y}{\Delta t} \left[(\rho_l^0 g_l^0 + \rho_s^0 (1 - g_l^0)) - (\rho_l g_l + \rho_s (1 - g_l)) \right] + S_{\text{mass}} \\ - \left[\rho_{l_{\text{up}}} u_e^* - \rho_{l_{\text{up}}} u_w^* \right] \Delta y - \left[\rho_{l_{\text{up}}} v_n^* - \rho_{l_{\text{up}}} v_s^* \right] \Delta x. \end{aligned} \tag{80c}$$

Conservation of Momentum: Pressure Equation

If a pseudo-velocity, $\widehat{u}_{(j,k)}$, is defined[70] as

$$a_{u_P} \widehat{u}_{(j,k)} = \sum a_{u_{nb}} u_{nb}^* + b_u \tag{81}$$

then from the momentum equation [Eq. (74)]

$$u_{(j,k)}^* = \widehat{u}_{(j,k)} + d_e (p_P^* - p_E^*) \qquad d_e = \frac{\Delta y_{(k)}}{a_P^u}. \tag{82}$$

While the '*de*' defined above is different than that used in the derivation of the pressure correction equation, (since it does not include the Doormaal, Raithby SIMPLE-C term), the form is the same as Eq. (77). Therefore, substitution of this expression for velocity into the continuity equation and repetition of the steps for the derivation of the pressure correction equation gives a similar result:

$$a_P P_P = a_E P_E + a_W P_W + a_N P_N + a_S P_S + b_{\text{press}}, \tag{83}$$

where, except for the definition of the *d*'s, the link coefficients are the same as for the pressure correction equations [Eq. (80)]

$$\begin{aligned} a_E &= \rho_{l_{\text{up}}} d_e \cdot g_{l_e} \cdot \Delta y, \qquad d_e = \frac{\Delta y_{(k)}}{a_{u_P}} \\ a_W &= a_{E_{(j-1,k)}} \\ a_N &= \rho_{l_{\text{up}}} d_n \cdot g_{l_n} \cdot \Delta x, \qquad d_n = \frac{\Delta x_{(j)}}{a_{v_P}} \\ a_S &= a_{N_{(j,k-1)}} \end{aligned} \tag{84}$$

and the source term is the same if $\widehat{u}$ and $\widehat{v}$ are substituted for u^* and v^*, giving a pseudo source term similar to Eq. (80*c*) but based on the pseudo-velocities [Eq. (81)]:

$$b_{\text{press}} = \frac{\Delta x \Delta y}{\Delta t}\left[(\rho_l^0 g_l^0 + \rho_s^0(1-g_l^0)) - (\rho_l g_l + \rho_s(1-g_l))\right] + S_{\text{mass}} - \left[\rho_{l_{\text{up}}}\widehat{u}_e - \rho_{l_{\text{up}}}\widehat{u}_w\right]\Delta y - \left[\rho_{l_{\text{up}}}\widehat{v}_n - \rho_{l_{\text{up}}}\widehat{v}_s\right]\Delta x. \tag{85}$$

Conservation of Momentum: The Solver Algorithm, SIMPLER

The conservation of momentum, conservation of mass, pressure correction, and velocity correction equations are linked together and solved using the SIMPLER algorithm.[70] Step one computes the link coefficients for the u–momentum equation using either equation set [(Eq. 72)] for the power law scheme or equation set [Eq. (73)] for the upwind scheme. Similar coefficients are computed for the v–momentum equations. Step 1 also computes the pseudo-velocities $\widehat{v}$ and $\widehat{u}$ as defined by Eq. (81). Step 2 calculates the link coefficients for the pressure and then uses Eq. (83) in conjunction with the $\widehat{u}$ and $\widehat{v}$ from Step 1 to compute the pressure field. This new pressure field in then used in Step 3 to compute an improved velocity field using the conservation of momentum Eq. (71). Step 4 solves the pressure correction based on the continuity error associated with the velocity field computed in Step 3 and uses this pressure correction and Eq. (77) in Step 5 to again improve the velocity field. The maximum continuity error and the maximum change in the 'u' velocity are then used as criteria to determine whether the velocity field is converged sufficiently. If not, Steps 1–5 are repeated until either the convergence tolerances are met or the number of iterations exceeds a preset limit.

Phase Change

Fundamental Considerations

The equations developed above conserve mass, momentum, energy, and solute but provide no means for determining when a phase change occurs, how much material solidifies, and what the relative liquid and solid solutal concentrations must be. These parameters are determined by the properties of the material. Numerically, the common approach to determine when and how solidification occurs is to assume the solid and liquid in a numerical control volume are in thermodynamic equilibrium. In this equilibrium approach, the temperature throughout a given numerical control volume is assumed uniform and equal in both the solid and liquid phases. The solutal concentration in the liquid, C_l, in a control volume is assumed uniform as is the solutal concentration in the solid, C_s, with the relationship between the two at a given temperature directly determined by the equilibrium phase diagram. The fraction of liquid, g_l, in the control volume at a given temperature and solutal concentration is based on conserving the net solute, C_o, in the cell. This relationship is given by: $C_o = g_l C_l + (1 - g_l) C_s$ and is known as the 'equilibrium lever rule.'[10] The rationale for this approach is that for sufficiently small control volumes the solid and liquid are in close proximity and the diffusion distances are small. Even for a small numerical control volume; however, the assumption that the concentration in the solid is uniform may not be valid. In the limit of zero solid diffusivity, only the solid in contact with liquid is at the equilibrium concentration dictated by the phase diagram. Thus, a non-uniform distribution of solute in the solid, known as coring results. This effect can be modeled by using the 'Scheil' equation[63] to determine the fraction of liquid and concentrations for a control volume based on the equation, $(C_s^* - C_l) dg_l = g_l dC_l$,

where C_s^* is the solid concentration at the solid-liquid interface. The Scheil equation conserves the net solute in a cell but assumes zero diffusion in the solid. In addition to the lever rule and Scheil equation, other assumptions for the solid and liquid thermal and solutal profiles in a given control volume may be adopted.[64] In the FTM, the equilibrium lever rule approach is used for each numerical control cell, but only after nucleation has occurred within that cell. A simple nucleation model is incorporated in the model and is explained below along with the details of the solidification algorithm.

Phase Change Calculations

For the ammonium chloride and water system, the equilibrium phase diagram relating the phase to the temperature and concentration was shown in Fig. II–3. In the FTM, the solidification for each numerical cell is based on the net energy and solute in that cell, the equilibrium phase diagram, and the amount of solid preexisting in the current and neighboring control volumes. If the nucleation criteria for a given cell are satisfied, the lever rule is applied to compute a new fraction of liquid based on the net solute in the cell and the given temperature. After this calculation, the net solutal concentration in the control volume has been conserved, but energy has not. In most models, this discrepancy is corrected later, during the conservation of energy algorithm, but in the FTM the solidification subroutine has its own internal iteration on the energy, using the lever rule to satisfy the phase diagram while adjusting the temperature to conserve net energy in the cell. This results in improved values for the volume fraction of liquid, the temperature, solid concentration, and the liquid concentration. This approach, while requiring additional computational effort in iterating for the temperature while computing liquid fractions, reduces the number of iterations required by the external nu-

merical loops containing the conservation of energy calculations. Because of the interdependent nature of energy, concentration, momentum, and mass, multiple iterations of the phase change along with all the conserved quantities are typically required before the solution converges to a fraction of liquid distribution which simultaneously satisfies the boundary conditions, the conservation equations, and the phase diagram.

Nucleation Criteria

The nucleation criteria in the FTM solidification subroutine require that at least one of three conditions be met before solid can form in a local numerical control volume. The first condition is preexisting solid, i.e., if solid already exists in the control volume from the previous time step then additional solidification is allowed. The second condition that results in nucleation is sufficient undercooling. Ammonium chloride-72 wt% water has been shown to undercool from 15°C to 30°C prior to solidification.[72] The lower limit, 15°C, was used as a conservative value for the criterion, since it corresponds to the threshold of possible nucleation due to undercooling. This approach was considered adequate for the CAST run conditions modeled since this degree of undercooling was not anticipated, as validated by the fact that during the simulation this second criterion was never invoked. If the run conditions were modified, e.g. faster cooling rates resulting in greater than 15°C undercooling, a more sophisticated undercooling criterion would be needed. The third condition for allowing solid to form in a numerical control volume is the proximity of solid, i.e., if solid in any of the neighboring cells exceeds a threshold value. This requirement is a geometrical constraint that attempts to account for the dendritic structure, by assuming that only if a critical amount of solid exists in the neighboring cell is there sufficient probability that

the dendrites in that cell can provide a nucleation site for growth within the given cell. A rough estimate can be made based on empirical observations of dendrite geometries and growth rates for the material being modeled. A threshold value of 1 percent volume fraction solid for current simulation was found to give a significant improvement over the assumption of zero threshold (the equilibrium assumption), and produced reasonable correlation with mushy zone growth data.

Properties

An accurate knowledge of the properties of the solidifying binary material is essential. Figure II–3 gave an idealized phase diagram for the NH_4Cl-H_2O system. The phase diagram is idealized in that the liquidus and solidus lines are approximated by straight lines. At the small length scales (on the order of millimeters)[3] and boundary conditions examined in this study, the slope of this line can be significant. For the sample case of a 7°C/cm temperature gradient near the mushy zone, a third of a degree error in the temperature results in a translation of the liquidus, and therefore the mushy zone, by almost half a millimeter. A change in solutal concentration of 0.07 weight percent would have a similar effect. These sensitivities point to the importance of incorporating realistic properties values in the numerical simulation. Fortunately the ammonium chloride and water system has been well researched and its properties published in a number of sources.[4,62,73–76] The specific method of calculation for each property used in the model are given below.

Thermal Conductivity

The conductivity of the liquid NH_4Cl-H_2O is approximately constant over the range of temperatures and concentrations of the CAST experiments. The conductivity used in the FTM is 5.02×10^4 $\frac{\text{ergs}}{\text{cm}\cdot\text{sec}\cdot^\circ\text{C}}$ which corresponds to 28

wt% NH_4Cl-H_2O at 25°C.[4] Similarly, the conductivity of the solid NH_4CL-H_2O is approximated as a constant at 3.93×10^4 $\frac{ergs}{cm \cdot sec \cdot °C}$.[67] The quartz has a conductivity of 1.38×10^5 $\frac{ergs}{cm \cdot sec \cdot °C}$.[73]

Diffusivity

The diffusivity of the liquid NH_4Cl-H_2O is approximated as 2.3×10^{-5} cm^2/sec which is an extrapolation of existing data over the range 0 wt% to 28 wt% NH_4Cl-H_2O at 25°C to 28 wt% NH_4Cl-H_2O at 25°C.[74] The diffusivity of solute in the solid NH_4Cl-H_2O and the quartz is negligible and assumed zero.[67]

Density

The density of the liquid NH_4Cl-H_2O is computed as a function of the temperature and concentration based on a two dimensional Taylor series expansion. The series is expanded about 25°C and 72 wt% solute density of 1.0767 gm/cm^3 with a constant thermal expansion coefficient, $\beta_t = 2.95 \times 10^4$ $\frac{1}{°C}$, and a constant solutal expansion coefficient, $\beta_S = -2.81 \times 10^{-3}$ $\frac{1}{wt\%}$.[4] The density of the solid NH_4Cl-H_2O (hypoeutectic) used is 1.5256 $\frac{gm}{cm^3}$ corresponding to its value at 20°C.[75] The value of the quartz density used was 2.2 $\frac{gm}{cm^3}$.[73]

Enthalpy

The enthalpy of the liquid NH_4Cl-H_2O is computed relative to an arbitrary enthalpy reference line at 18°C. The specific heat $\frac{\partial h}{\partial T}$ used to compute the enthalpy relative to this reference line is calculated as a function of the liquid concentration,[75]

$$C_p = \left(4.3 \times 10^{-4} \cdot (100 - C_l)^2 - 4.4 \times 10^{-2} \cdot (100 - C_l) + 4.189\right) \times 10^7 \quad \frac{ergs}{°C \cdot gm}$$

and the liquid enthalpy is then calculated based on this specific heat:

$$h_l = C_p \cdot (T - 18°C).$$

The specific heat for the solid enthalpy is also calculated as a function of the solutal concentration based on a proportional combination of the specific heat for the solid enthalpy of pure solid NH_4Cl and the specific heat for pure ice. The specific heat for pure NH_4Cl is computed from:

$$\left(\frac{\partial h_s}{\partial T}\right)_{NH_4CL} = 4.1789 \times 10^7 \cdot \left(\frac{9.8 + .0368 \cdot (273. + 18.)}{53.49}\right) \qquad \frac{ergs}{°C \cdot gm}.$$

The specific heat for pure ice is 2.89×10^7 $\frac{ergs}{°C \cdot gm}$[73] and the combination of the two is:

$$\left(\frac{\partial h_s}{\partial T}\right) = \left(\frac{\partial h_s}{\partial T}\right)_{NH_4CL} + \frac{C_l}{100} \cdot \left[\left(\frac{\partial h_s}{\partial T}\right)_{ice} - \left(\frac{\partial h_s}{\partial T}\right)_{NH_4CL}\right].$$

The dependence of the solid enthalpy on solutal concentration is calculated by a linear interpolation between the latent heat for pure water and pure NH_4Cl. Since the latent heat, L, for pure NH_4CL is 2.764×10^9 $\frac{ergs}{gm^3}$ and for pure water is 3.327×10^9 $\frac{ergs}{gm^3}$,[73] the change in enthalpy for the solid as a function of concentration is assumed to be:

$$\left(\frac{\partial h_s}{\partial C_s}\right) = \frac{2.764 - 3.327}{100} \times 10^9 \qquad \frac{ergs}{wt\% \cdot gm}.$$

Combining all the above gives an enthalpy of the solid NH_4Cl-H_2O calculated as

$$h_s = \left(\frac{\partial h_s}{\partial T}\right) \cdot (T - 18°C) + \left(\frac{\partial h_s}{\partial C_s}\right) \cdot C_s - L \qquad \frac{ergs}{gm}.$$

The enthalpy of the quartz is computed based on a reference enthalpy line of zero at 18°C and a specific heat of 7.54×10^6 $\frac{ergs}{°C\ gm}$.[73]

Viscosity

The viscosity of the liquid NH_4Cl-H_2O is set to 1.06×10^{-2} $\frac{dynes \cdot sec}{cm^2}$, the value at 28 wt% NH_4Cl and 25°C.[75] The error introduced by the assumption of constant viscosity is less than 10% over the temperature range from 10°C to 40°C.

The viscosity of the quartz is set to 1.0×10^{20}. Setting the viscosity of the quartz to a high number allows the numerical solver to implicitly account for the rigidity of the quartz rather than having to directly specify its effect on the neighboring fluid momentum.

Phase Diagram

The liquidus temperture, T_{liq} of the NH_4Cl-H_2O phase diagram from 70 wt% to 80.4 wt% H_2O (eutectic) was approximated ($\sigma = .83\%$), as a linear function of liquid concentration, C_l, $T_{\text{liq}} = 360.03 - \left[\frac{375.03}{80.315}\right] C_l$.[75] The solidus was then dictated by the partition coefficient, the ratio of the concentration in the solid to that in the liquid, which has been measured by McCay et al.[5] as .004. A list of the property values used in this study is provided in Table III–1.

Numerics

The discretized conservation of momentum, mass, energy, and solute equations, along with the phase change algorithm and the properties above must be linked together in an iterative scheme in order to calculate a solution. This interlaced program structure is outlined in the flow chart in Fig. III–8. The chart reflects the coupled nature of the equation system. Within a time step, the fraction of liquid is first evaluated over the domain based on the best estimates of temperature and concentration. This calculation is followed by the calculation of the density. Next the flow field is solved to satisfy the momentum force balance and continuity. The resulting improved estimates of the fraction of liquids, densities, and velocities are then used in the computation of the transport of heat and solute which will be passed back to the top of the main loop to provide an improved value for computing the fraction of solid. The complete process is repeated until tolerances are met or a maximum iteration number is exceeded.

TABLE III–1. Material Properties

	NH_4Cl-72 wt% H_2O		
	Solid	Liquid	Quartz
Specific heat $\frac{ergs}{°C \cdot gm^3}$	1.61×10^7	3.30×10^7	7.54×10^6
Conductivity $\frac{ergs}{°C \cdot cm^1}$	3.93×10^4	5.04×10^4	1.38×10^4
Density ($gm \cdot cm^{-3}$)	1.53	1.06 to 1.08	2.20
Diffusion Coefficient ($cm^2 \cdot s^{-1}$)	0	2.3×10^{-5}	0
Viscosity ($dyne \cdot s \cdot cm^{-2}$)	—	1.06×10^{-2}	1×10^{20}
Enthalpy ($ergs \cdot gm^{-1}$)	$(-2.56 \times 10^9$ to $-1.71 \times 10^9)$	$(2.31 \times 10^8$ to $2.17 \times 10^9)$	$(1.74 \times 10^7$ to $5.40 \times 10^8)$
Thermal expansion coef ($°C^{-1}$)	0	2.95×10^{-4}	0
Solutal expansion coef ($wt\%^{-1}$)	0	-2.8×10^{-3}	—
Equilibrium partition ratio	.004		

The convergence tolerances and maximum iteration numbers associated with the program structure are an important set of numerical parameters, since specify the desired degree of accuracy and iteration limits for various blocks of the program. For example, the calculation of the pressure in Step 2 of the SIMPLER flow solver (Fig. III–8b), is regulated by a tolerance and maximum number of iterations for pressure (labeled as toler (press) and loop (press)). These two parameters are critical since the flow field is very sensitive to small errors in pressure. This sensitivity is the primary reason the model requires double precision and the tolerance for the pressure is set to the minute value of 1×10^{-7} $\frac{dynes}{cm^2}$, only 10^{-10} of the maximum value of the pressure. The mass error tolerance is another critical

input and is set to an absolute value of 1.0×10^{-8} grams per control volume. Since the density is critical, the temperature tolerance is set to 0.001°C and the concentration tolerance to .0001 weight percent water.

As a general rule, all of the numerical tolerances in the model were kept very small to assure accuracy of the solution. This was done at the expense of computational time. For a time step of 0.25 sec, a physical second of simulation using a 386/33 MHz personal computer required about 2.5 minutes during the diffusion dominated growth stage. Once convective breakdown occurred, the computational requirement increased dramatically to approximately 1.6 hours per second of simulation. A sample listing of the code is to be released in the Casting and Solidification Technology (CAST) Final Report, M. H. McCay, NASA CR, NAS8-37292, Marshall Space Flight Center, Huntsville, Alabama.

One other important numerical feature of the FTM is the choice of grid. The grid used for the simulation is shown in Fig. III–9. Experimental results[3] have indicated that the solutal boundary layer which forms ahead of the liquid-solid region is on the order of 1 millimeter, thus necessitating the need for a fine grid in and above the mushy zone. The height of a control volume at the bottom of the cuvette is 0.125 mm. The lateral dimension of the interior grid cells is 0.625 mm. Even this small scale will be shown to be inadequate to resolve some of the detailed flow structures associated with the current experiment.

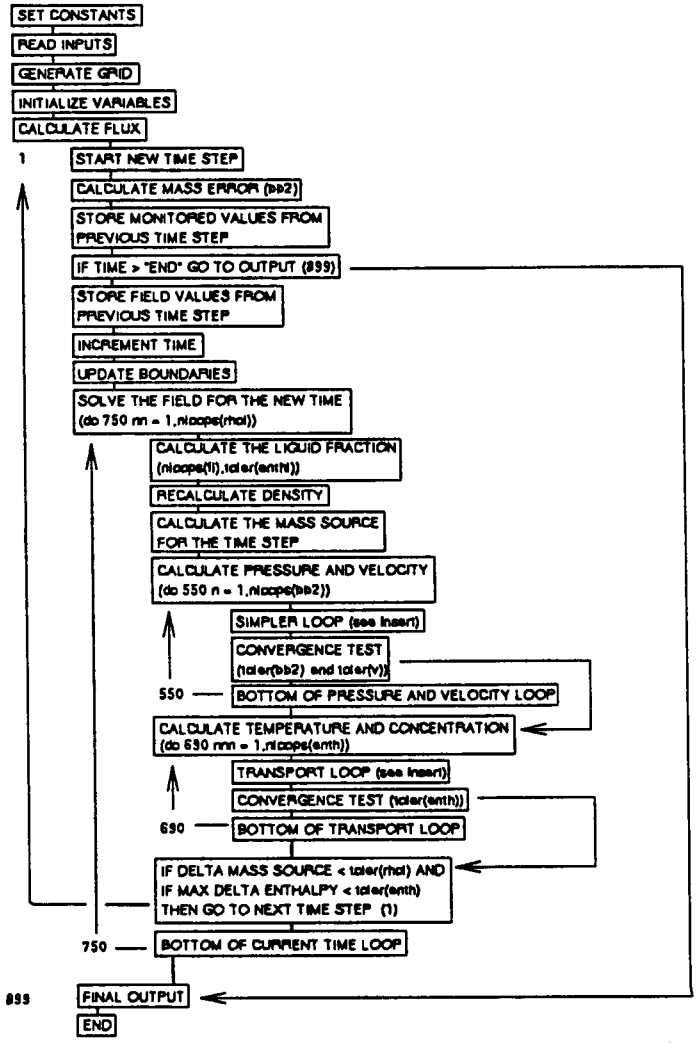

Figure III–8a. FTM flowchart

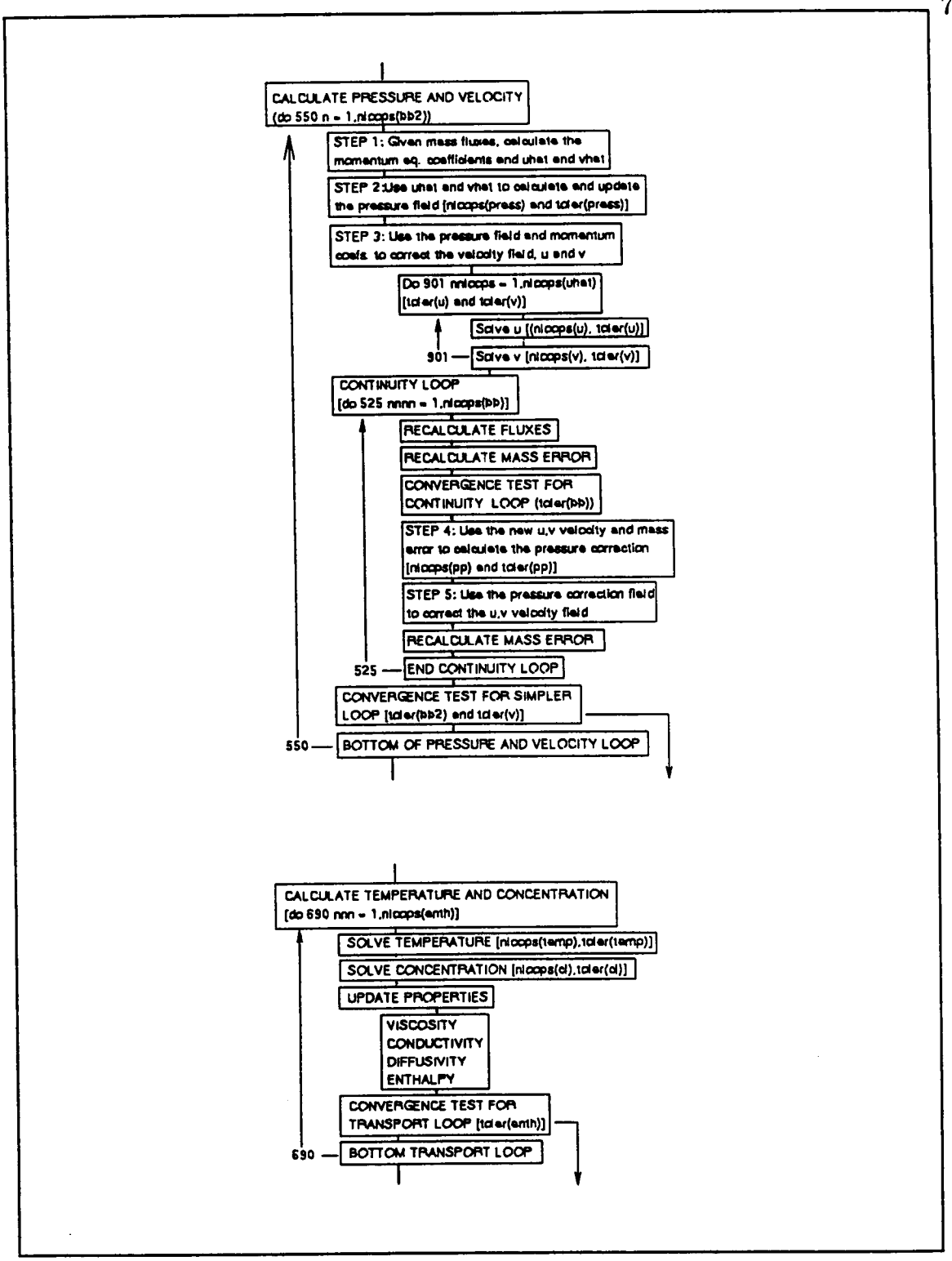

Figure III–8b. FTM flowchart (cont.)

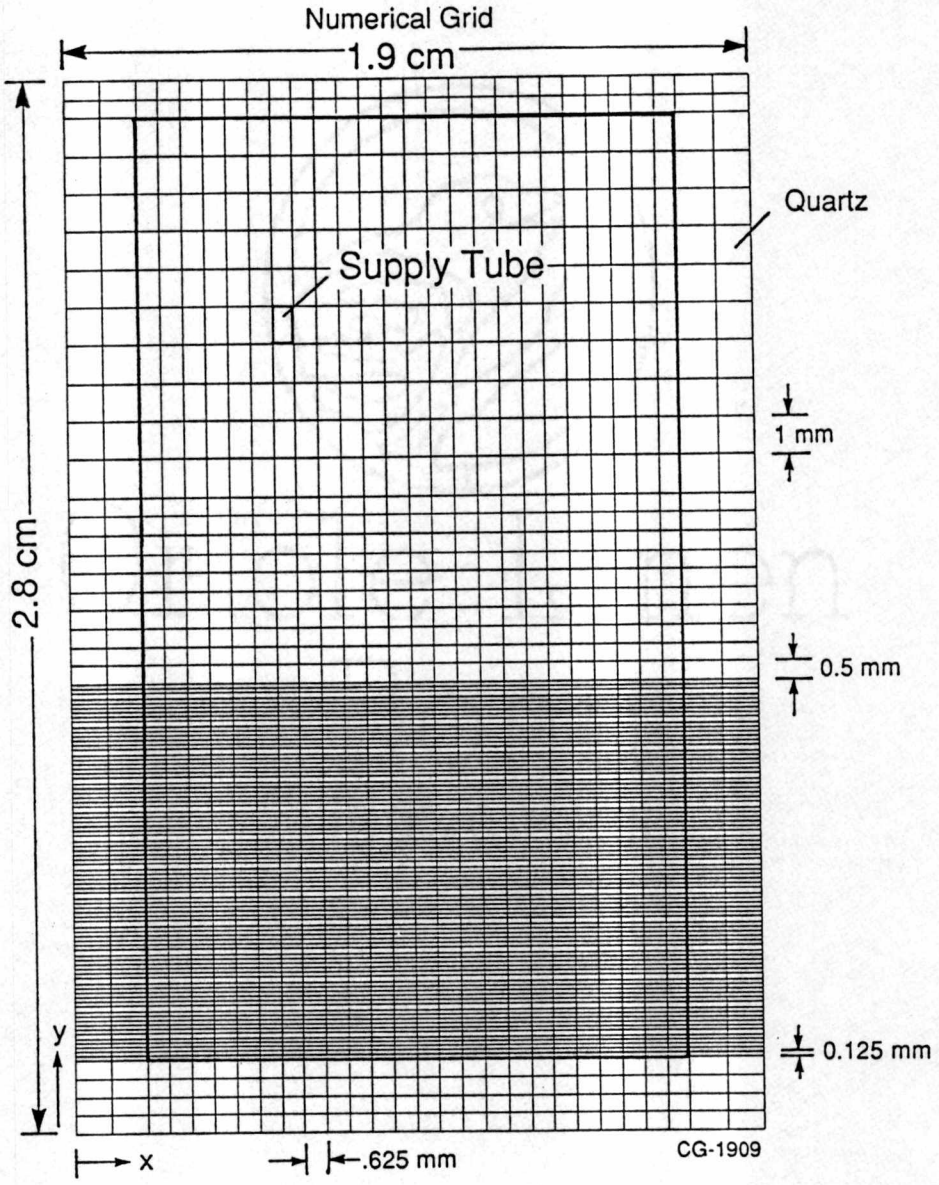

Figure III–9. Numerical grid

SECTION IV

MODEL VALIDATION

Introduction

Prior to using the FTM to predict solidification in microgravity, a number of validation cases were run. These cases included basic hydrostatic problems, no-flow thermal transient predictions, simple flow problems such as Poisieulle flow, and natural convection of water in a square cavity. A representative set of the natural convection comparisons is provided below.

The FTM was further validated by comparison with CAST ground-based data. This comparison provided a more comprehensive test of the model's capabilities since it included all aspects of the process (conduction in the quartz, phase change, thermal and solutal convection, etc.) required for the microgravity simulation. The ground-based CAST runs also serve as a reference for the microgravity predictions.

Buoyancy (Thermal) Driven Convention

The FTM's ability to model thermally driven flows was tested by comparison with a set of numerical and experimental data for the natural convection of water in a square cavity. The experiments used for this comparison were conducted by Inaba and Fukuda[77] and the numerical predictions were computed by Lin and Nasteel.[78]

The natural convection experiments[77] were for water in a tilted, rectangular test section 1.5 cm tall by 1.5 cm wide by 10 cm deep with fixed side wall temperatures. The remaining front, back, top, and bottom walls were insulated.

The depth of the container was chosen by the experimenters to be large relative to the height and width to make the experiment approximately two-dimensional. The angles of inclination (about the long axis) ranged from 0 to 180 degrees and the fixed side wall temperatures ranged from 0°C to 8°C. A test run consisted of imposing the desired angle and temperatures on the test section and holding those conditions until the resulting flow stabilized. Particles in the water were then illuminated and photographed using long exposure times in order to record the flow pattern. These particle traces constituted the basis for comparison with the FTM predictions.

The Inaba and Fukuda study was chosen for comparison with the FTM for two reasons: the properties of water over the temperature range of the Inaba experiment (4°C ± 4°C) are well known,[78,79] and it provided flow visualization data for a geometry and Rayleigh number (1.24×10^5) similar to those of the CAST experiment. The properties are listed in Fig. IV–1.

$$\mu = (1.789 - .0489 \cdot T) \cdot \rho \cdot 10^{-2}. \qquad \left(\frac{\text{dyne}\cdot\text{sec}}{\text{cm}^2}\right)$$

$$\rho = 0.99997 \cdot \left[1 - \alpha_1 |T - 4.029325|^{1.894816}\right] \qquad \left(\frac{\text{gm}}{\text{cm}^3}\right)$$

$$k = .558 \times 10^5 + .0019 \times 10^5 \cdot T \qquad \left(\frac{\text{erg}}{\text{cm}\cdot s\cdot{}^\circ\text{C}}\right)$$

$$Cp_l = 4.226 \times 10^7 - .0031 \times 10^7 \cdot T. \qquad \left(\frac{\text{erg}}{{}^\circ\text{C}\cdot\text{gm}}\right)$$

Figure IV–1. Properties of water near 4°C as a function of temperature

The first set of experimental conditions used for comparison was for 8°C on the left wall, 0°C on the right, with zero inclination (the imposed temperature gradient was orthogonal to the gravity vector). The time-lapse photograph for the resultant steady state flow pattern is shown on the right-hand side of Fig. IV–2. The streamlines predicted by the FTM for these conditions are provided on the left-hand side of the same figure. The imposed temperature distribution from 8°C to 0°C generated a pair of vortices. In the middle of the test cell the flow was downward, corresponding to the maximum density of water near 4°C. Comparison of the computations and the data shows that the FTM has predicted this basic flow pattern. The small differences in shape between the predicted and the experimental streamlines are attributed to three-dimensional effects inherent in the physical experiment.

As a second comparison, the FTM was used to compute the flow for a similar case in which the side wall temperatures were the same as above, except the container was rotated counterclockwise 60°. A comparison of the predicted and experimental steady state flow pattern for this case is given in Fig. IV–3. Again the qualitative comparison is good, with small differences in the streamline shapes probably due to three-dimensional effects.

In order to obtain a quantitative validation for buoyancy driven convection using a strictly two-dimensional problem, a comparison was made with the two-dimensional numerical prediction of Lin and Nansteel[78] for the first of the experiments discussed above (Fig. IV–4). Their numerical model computed the temperature distribution along the centerline of the container and those results are given in Fig. IV–4 along with the FTM prediction. The two numerical predictions correlate to within 0.25 °C. The difference may be attributed to Lin and Nansteel's assumption of constant properties (other than for density).

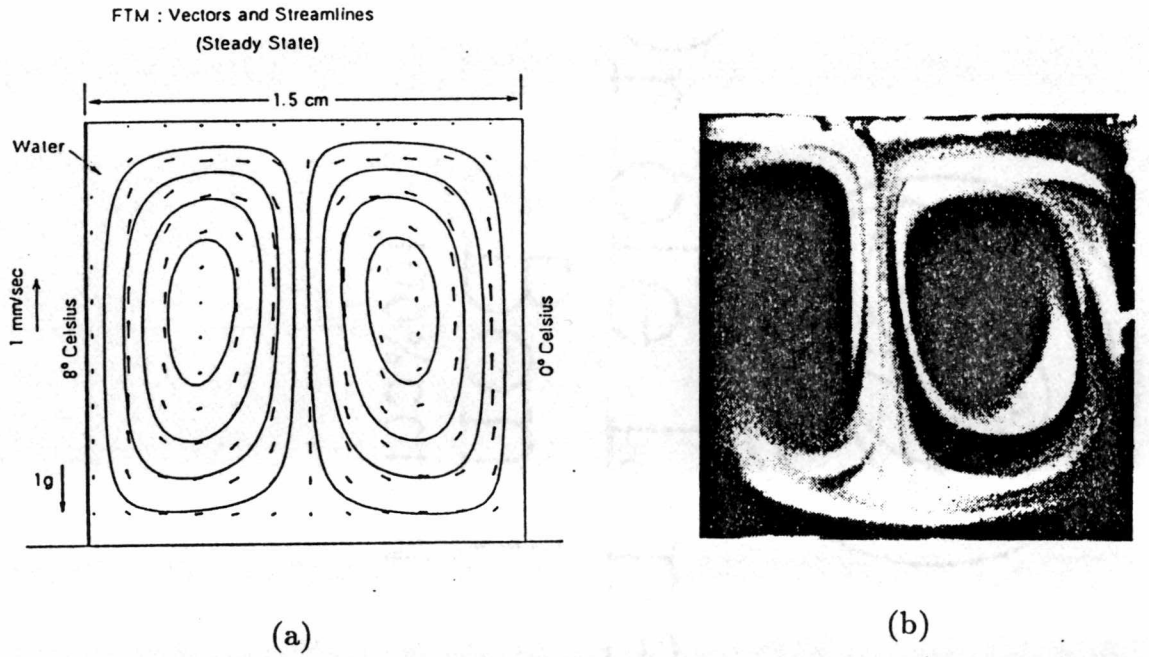

(a) (b)

Figure IV–2. Flow patterns for water in a 1.5 cm by 1.5 cm square cavity with 8°C on the left wall and 0° on the right (a) FTM streamlines (b) Experiment particle traces[77]

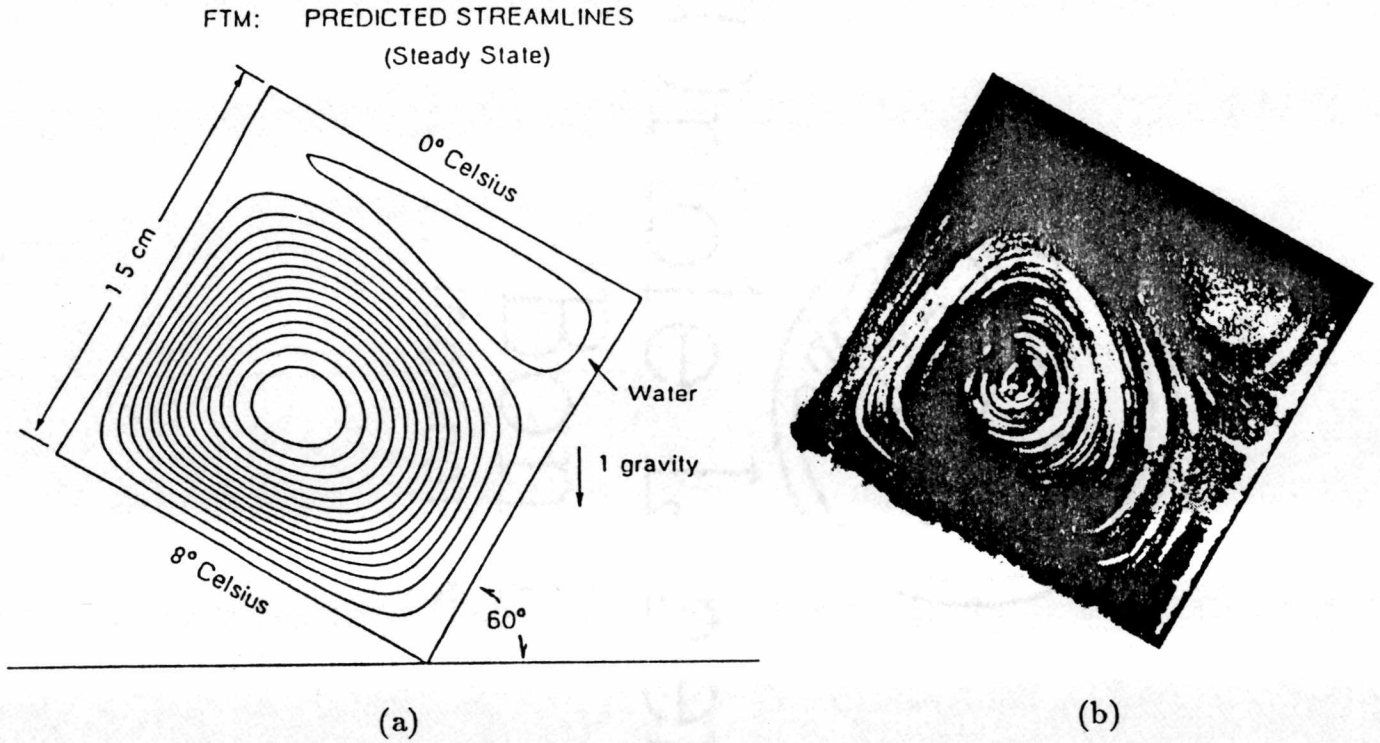

Figure IV–3. Flow patterns for water in a 1.5 cm by 1.5 cm square cavity tilted 60° counterclockwise with 8°C on the left wall and 0° on the right (a) FTM streamlines (b) Experiment particle traces[77]

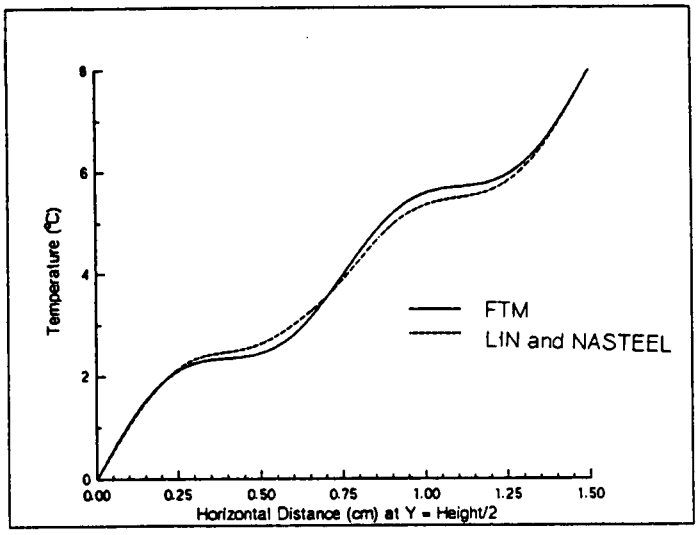

Figure IV–4. Thermal profile (at y = height/2) for water in a 1.5 cm by 1.5 cm square cavity with 8°C on the left wall and 0°C on the right

CAST Ground Based Runs: Initial Conditions

The quantitative comparison with Lin and Nansteel's numerical computations and the qualitative comparison with Inaba and Fukada's experiments demonstrated the FTM's capability to compute the coupled effects of flow and temperature for steady state natural convection in water. This capability is only part of that required for the modeling of the more complex transient, two-phase, thermosolutal phenomena inherent in the CAST solidification experiments.

The major verification of the model's capability to accurately simulate all aspects of the CAST space experiment was accomplished by comparison with existing data from the CAST ground-based experiments. Three ground-based

runs were chosen for comparison, each initiated from the same set of initial steady state conditions. Thus the first requirement for the FTM was to predict these initial conditions. The method used by the FTM to compute the initial state and the accuracy of those computations are discussed below.

For the three cases to be presented, the initial conditions consisted of 72 wt% H_2O-NH_4Cl solution with 58.5°C imposed on the top of the cuvette and 21°C on the bottom. With these boundary conditions, the solution at the bottom of the cuvette is below the liquidus temperature but above the eutectic temperature, resulting in a thermally stratified solution with a two-phase dendritic mushy zone at the bottom of the cuvette.

An intricate process is required to achieve the initial state in the laboratory. As the first step, solid NH_4Cl-H_2O must be formed if not already present. Next, the initial temperature gradient is imposed on the cuvette and held for a 'sufficiently' long period to allow the system to stabilize. This procedure involves nucleation kinetics, solidification, dendrite coarsening, convection due to expansion (pressure driven) flows, and mass transport due to diffusion. In the one-gravity environment, buoyancy driven flows and settling of dendrite fragments further complicate the process.

The end result of the above procedure is a set of initial steady state conditions which depend only on fixed boundary conditions. Hence, the method of preparation of the initial state is not critical if the final boundary conditions are held sufficiently long to allow the system to equilibrate. In the laboratory, three hours of thermal hold time is considered sufficient to establish equilibrium, since additional holding does not result in any perceptible change in the state of the system.[8]

The FTM prediction of the CAST initial conditions is also path independent if the boundary conditions corresponding to the initial state are held sufficiently long. This provides the freedom to compute the initial state by the most numerically expedient computational path. As in the laboratory, it is determined that the system has attained steady state based on the subjective assessment that the system is no longer undergoing any significant change.

The specific path used in the FTM to compute the initial conditions for the three CAST runs under consideration was to first compute a steady state without gravity and then adjust to one-gravity conditions. This avoided the difficulty of computing the vigorous natural convection associated with the coarse readjustment of the dendritic layer that typically occurs when the initial temperatures are first imposed on the cuvette.

The details of the numerical initial state predictions are as follows. The ammonium chloride and water solution in the numerical domain was input as liquid NH_4Cl-72 wt% H_2O. The bottom and top temperatures of the cuvette were fixed at 21°C and 58.5°C, respectively. The temperature distribution between the top and bottom was estimated and specified (but not fixed) as linear.

The boundary temperatures were then held constant while the model was run to simulate 160 hours of holding time without gravity effects. The large simulated run time (large relative to the three hours required in the laboratory) was needed because setting gravity to zero eliminated natural convection, leaving diffusion as the only transport mechanism, and thus increased the 'real' time required to obtain equilibrium. Numerically, however, it was still more expedient to simulate 160 hours of diffusion (using one hour time steps) then to simulate 3 hours of combined diffusion and convection. In order to verify that the 160 hour results were in fact steady, the boundary conditions were imposed for an additional 1600

hours using 10 hour time steps. The results indicated that the mushy zone height, the thermal field, and the solutal distribution had all stabilized to within the numerical error.

Gravity effects were then included to account for lateral variations in density. In order to include gravitational effects in the numerical computation of the initial conditions, the results from the 1600 hour hold at zero-g were input into a second transient simulation using the same steady state boundary conditions with the exception of the gravity term, which was set to one earth gravity. For this more difficult problem, the numerical time step was first reduced to 0.25 seconds and the boundary conditions held for 10 minutes, followed by 50 minutes of holding using 15 second time steps. The end result was that buoyancy driven flows had developed due to lateral temperature gradients. As verification that these predicted flows were steady, the simulated hold was extended to 10 hours using 150 second time steps. These 10 results were accordingly used as the FTM prediction of the steady initial state corresponding to the ground-based experimental initial conditions.

The FTM model parameters used to establish the initial conditions are provided in Fig. IV–5. The first three inputs (i.e., the top temperature, the bottom temperature, and the solutal concentration) correspond to the initial conditions of the ground-based experiments. The next input, K_o, is the constant in the Darcy flow term in the momentum equations and relates to the flow resistance in the two-phase region. The value used is the same as that used by Bennon and Incropera[67] for NH_4Cl-H_2O and is based on available dendrite arm spacing data. The last two terms, T_R and h_{coef}, are the room temperature and the heat loss coefficient, used in the FTM to account for the heat lost from the walls of the cuvette.

The initial steady state temperatures, flow field, solutal field and the mushy zone height predicted by the FTM are compared with the experimental data below.

Top Temperature = 58.5°C

Bottom Temperature = 21.0°C

Concentration = 72 wt% H_2O - 28 wt% NH_4Cl

$K_o = 5.56 \times 10^{-7}$ cm^2

$T_R = 22°C$

$h_{coef} = 24000 \frac{ergs}{cm^2 \cdot °C}$

Figure IV–5. Model parameters: Initial conditions

The computed initial temperature distribution is shown in Fig. IV–6. The distribution exhibits a nonlinear profile in both the vertical and horizontal directions due to heat loss through the side walls and the mismatch between the conductivity of the quartz container and the solution. Parametric calculations indicate that the heat lost from the exposed walls is the primary cause of the vertical non-linearity shown in the Fig. IV–6.

The capability to account for the effects of spatially varying conductivities is an integral part of the FTM, but the heat lost to the environment must be included using an empirical model based on a loss coefficient times the temperature difference between the quartz wall and the environment. Although the FTM is essentially two-dimensional, this loss is numerically accounted for at all exposed walls, including the front and back walls. For the CAST ground-based cases, the room temperature was approximately 22°C and the heat loss coefficient was set at 24,000 $\frac{ergs}{cm^2 \cdot °C}$. This coefficient is roughly four times that for natural convection on a vertical plate and accounts for the more complex geometry and additional forced convection in the laboratory.

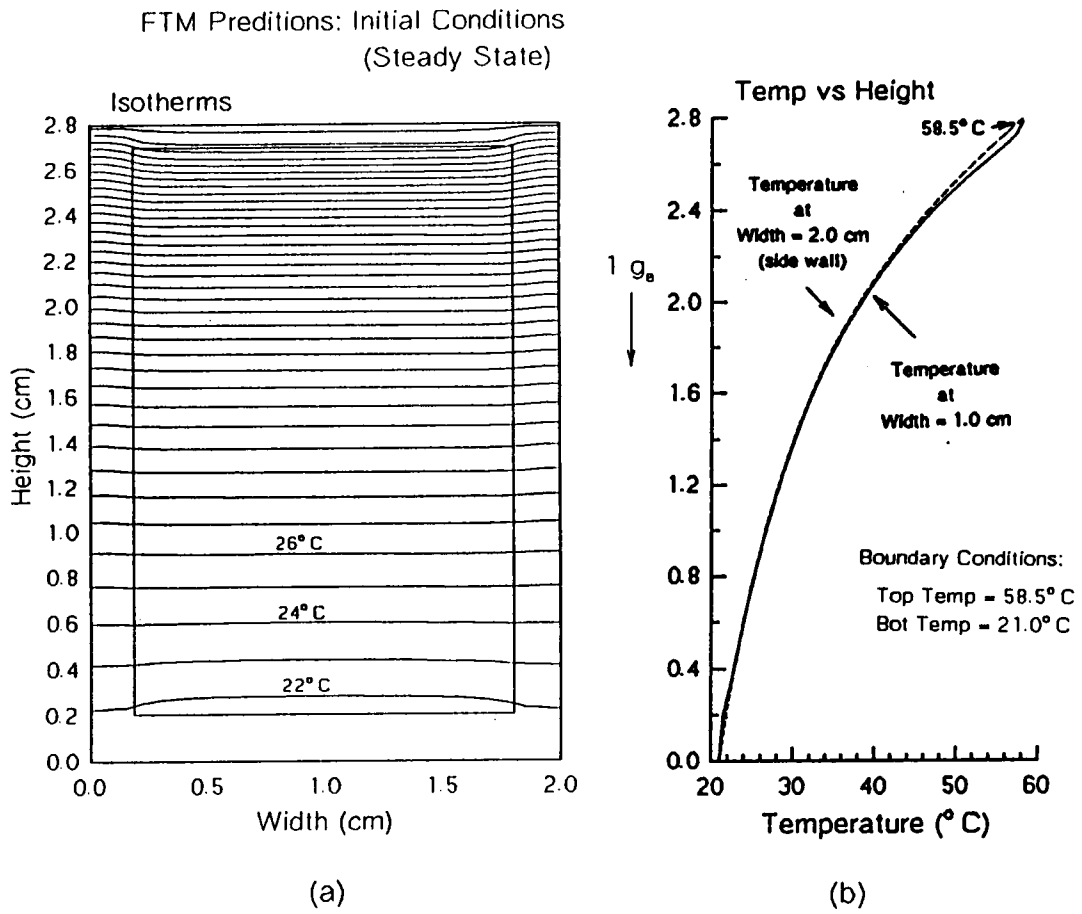

Figure IV–6. Initial conditions: Predicted temperature distribution. Top temperature = 58.5°C; Bottom temperature = 21°C (a) Isotherms (frontal view) (b) Temperature vs. height (centerline and sidewall)

The combined effects of heat loss to the ambient and the difference in conductivity between the quartz and fluid influence the initial conditions in several ways. One is the lateral temperature gradient in the fluid, evidenced in the predicted isotherms (Fig. IV–6a). These small lateral temperature gradients are sufficient to drive flow. The non-uniform initial temperature field also affects the initial height of the mushy zone and influences the morphology of the system by reducing the temperature gradient near the mushy zone. This gradient is calculated to be approximately 6°C/cm compared with a 13.4°C/cm gradient for a linear temperature distribution between the top and bottom.

The predicted streamlines for the initial condition flows are shown in Fig. IV–7. Thermally driven vortical rolls are evident in the upper corners with velocities on the order of 0.005 cm/sec. The FTM also predicts weak roll structures at the bottom of the cuvette with velocities on the order of 0.001 cm/sec, shown in the expanded view of the velocities in Fig. IV–7(b). The presence of these flows is significant since they provide a preexisting perturbation source for convective instabilities.

The solutal distribution computed for the initial conditions is shown in Fig. IV–8. The solutal contours and the centerline solutal distribution versus cuvette height indicated equilibrium to within .005 wt% solutal concentration. In the liquid region, the bulk concentration is nearly constant at approximately 72.465 weight percent solute (water). The difference between this concentration and the original liquid concentration of 72.00 wt% is due to salt (NH_4CL) being preferentially incorporated into the solid. The resultant bulk liquid concentration coupled with the equilibrium temperature distribution determines the height of the mushy zone and the solid fraction. The 0.99 fraction of liquid contour in Fig. IV–9 provides an outline of the initial mushy zone shape. The mushy zone thickness is relatively uniform except at the side walls. The detailed distribution of the solid in the

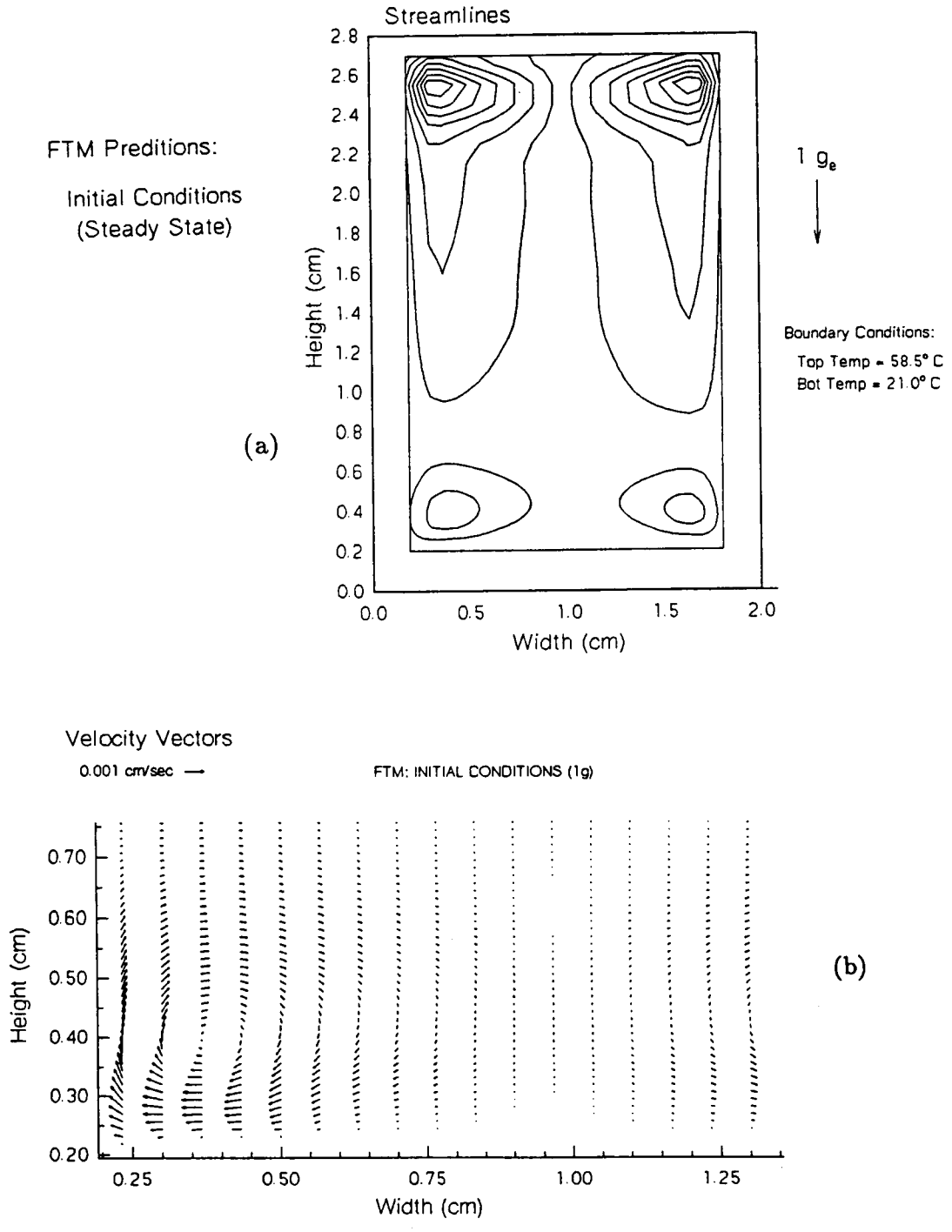

Figure IV–7. Initial conditions: Flow pattern. Top temperature = 58.5°C; Bottom temperature = 21°C (a) Numerical streamlines (b) Velocity vectors (expanded view)

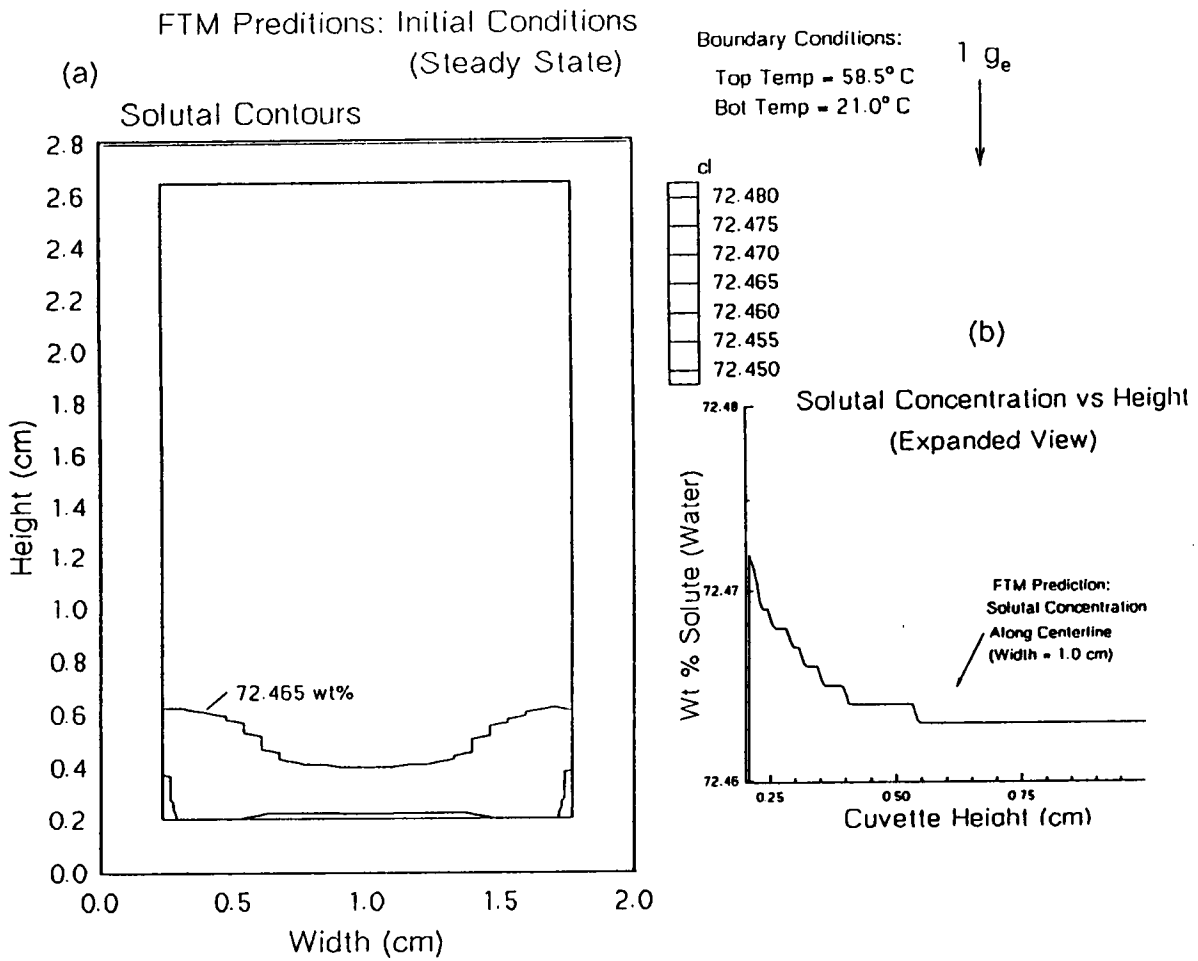

Figure IV–8. Initial conditions: Predicted solutal distribution. Top temperature = 58.5°C; Bottom temperature = 21°C (a) Concentration contours (frontal view) (b) Concentration vs. height (centerline).

mushy zone is provided in the expanded view in Fig. IV–9.

The above figures, IV–6 through IV–9, show the initial state of the CAST ground-based experiments as predicted by the FTM. The primary experimental data used for comparison with the FTM results were recorded interferometer images. Since the index of refraction of the ammonium chloride and water is a known function of concentration and temperature, interferometer fringe patterns are easily computed from the FTM results, providing a direct means of comparison with the observed fringe patterns, as shown in Fig. IV–10. The view is the lower two thirds of the cuvette and the scale is indicated by the grouping of dots. These dots have a vertical incremental spacing of 1 mm. The interval between fringes corresponds to a temperature change of 0.457°C. Inspection of Fig. IV–10 thus indicates that the temperature gradient above the mushy zone is predicted to within 0.5°C/cm.

In addition to interferometer images, the initial velocity fields computed by the model were qualitatively compared with ground-based data obtained using time lapse photography of suspended neutral density particles. The predicted vortical flows at the top of the cuvette were observed in the laboratory with velocities on the order of 0.008 cm/sec, compared with the computed velocities on the order of 0.005 cm/sec. The predicted weak roll structures at the bottom of the cuvette with velocities on the order of 0.001 cm/sec were not evident in the particle tracking photographs. The lack of empirical evidence of the rolls in the lower corners may be due to the difficulty of using particle tracking for such weak phenomena.

The final parameter used for comparison is the shape and height of the mushy zone. The predicted curvature of the mushy zone near the side walls Fig. IV–9 is evident in the experiments and substantiates the isotherm curvature in Fig. IV–6. The absolute height of the mushy zone, however, is over-predicted as 0.44 mm, compared to an average measured[12] value of 0.34 $\pm$.06 mm.

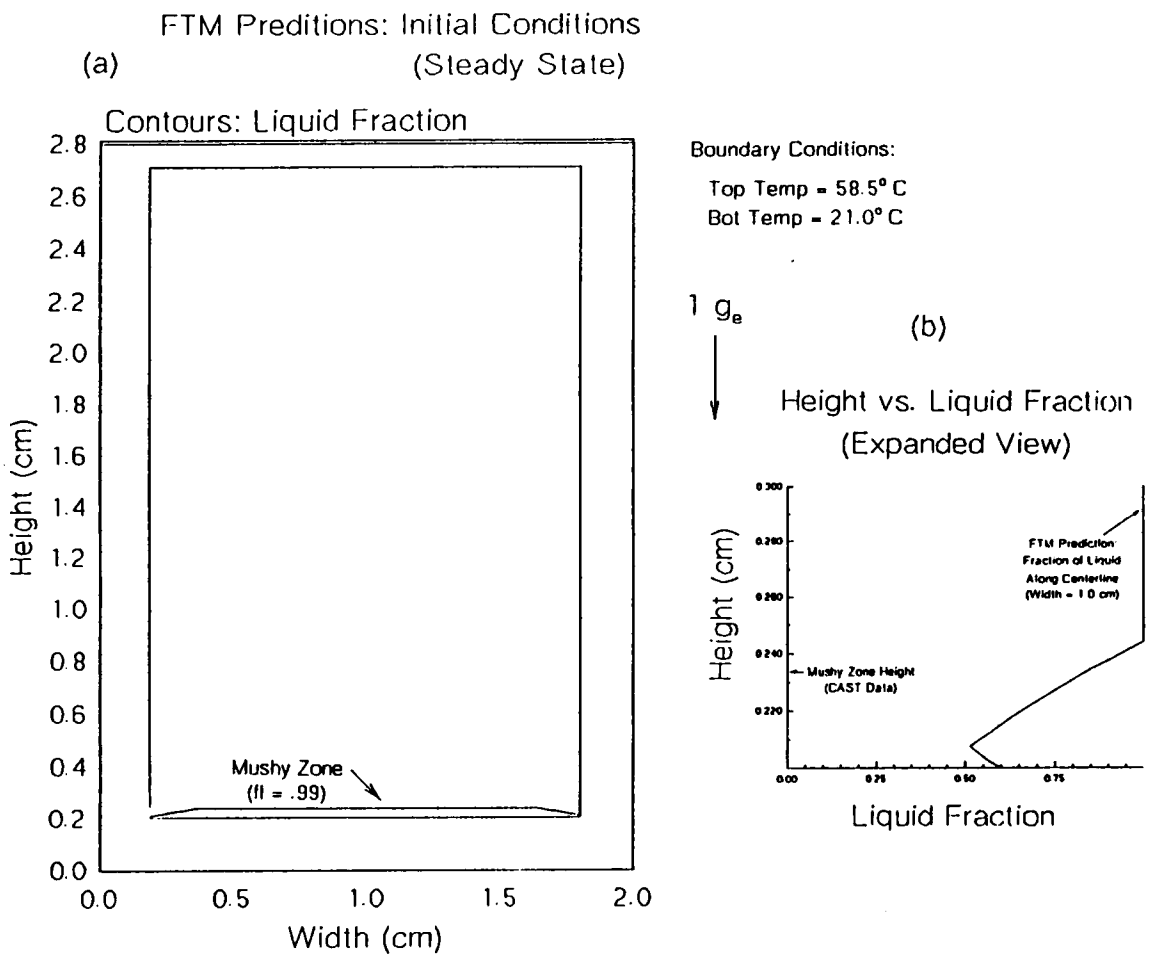

Figure IV–9. Initial conditions: Predicted fraction of liquid distribution. Top temperature = 58.5°C; Bottom temperature = 21°C (a) Contour (frontal view) (b) Fraction of liquid vs. height (centerline)

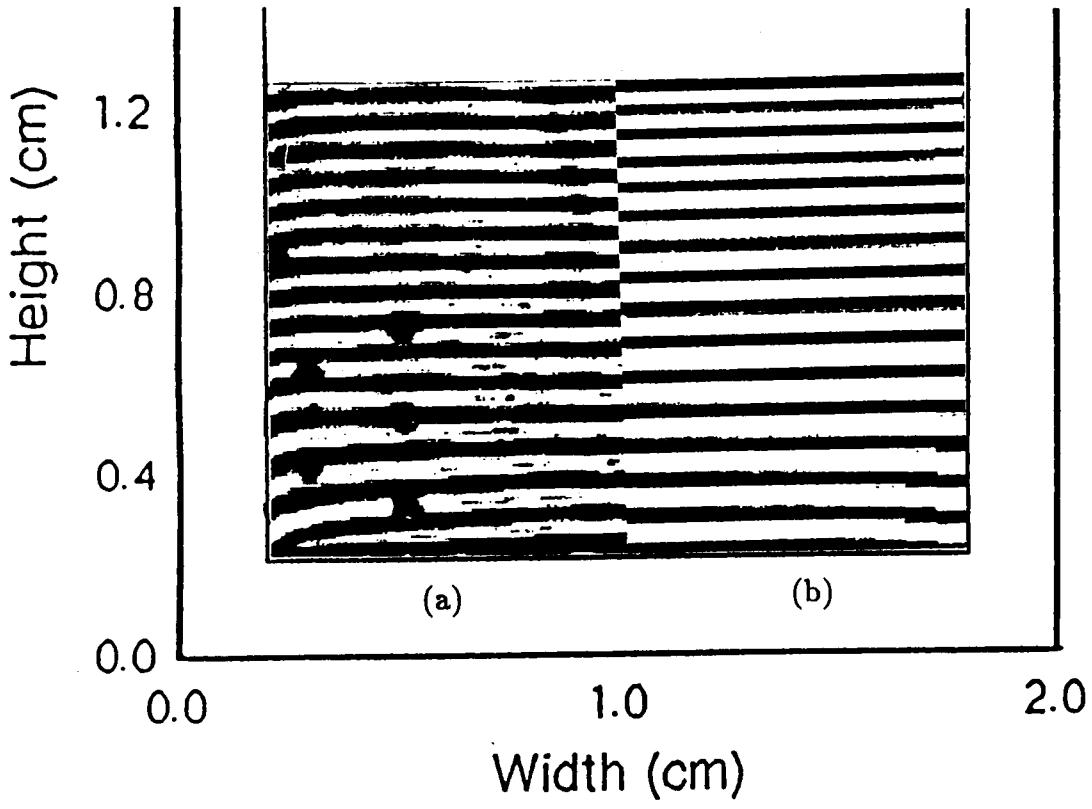

Figure IV–10. Initial conditions: Interferometer fringe comparison. Top temperature = 58.5°C; Bottom temperature = 21°C (a) Experimental (b) Predicted

This error of 0.1 mm in the predicted height of the interface could be due to a combination of several factors, including the step function nature of the interface position due to the finite grid; errors in the properties; the lack of three dimensional effects; an error in the environmental heat transfer coefficient; or thermocouple measurement errors introduced through the boundary conditions. Without specific knowledge on the source of the error, the discrepancy must be considered a model inaccuracy.

The error in the position of interface was a concern, in particular, for the prediction of the ground-based runs in which the net height of the mushy zone is small over the course of the experiment. For the ground base initial conditions, the 0.1 mm error in predicting the location of the mushy zone front is equivalent to a 30% error in the mushy zone thickness, which is expected to have some influence on the convective stability of the system. Fortunately, both numerical results and the experiments have shown[5,8] that for a given thermal gradient (i.e., density gradient), variations in initial mushy zone height on this order have a weak influence on the primary growth phenomena such as the development of the inversion layer, mushy zone growth, and time of convective breakdown. Only the critical Rayleigh number associated with convective breakdown is significantly affected by the initial zone height. As such, the 0.1 mm error in the mushy zone height is not expected to significantly degrade the model's capability to predict the transient phenomena, with the exception of the critical Rayleigh number. Accordingly, the FTM initial conditions as computed above were accepted as the starting conditions for the three ground-based solidification predictions to be discussed in the next sub-section.

CAST Ground Based Runs: Directional Solidification

The initial conditions calculated by the FTM demonstrated the capability to compute steady state conditions for the CAST experiments. The capability to compute the transient phenomena, in particular directional solidification, was validated by simulating the directional solidification stage of the CAST ground-based experiments. The validation is based on predictions of the growth of the mushy zone, the development of the density inversion layer, the transient two-dimensional thermal and solutal fields, and the spatial and temporal onset of convective breakdown. Results of this simulation are presented for the three cases outlined in Table IV–1.

The 2°C/min cooling rate was chosen as the primary verification case because of the extensive data available for that cooling rate.[8] The initial conditions were those of the previous section. Starting from those steady boundary conditions, the top and bottom temperatures were lowered at 2°C/min to produce directional solidification.

The predicted growth of the mushy zone is compared with experimental data in Fig. IV–11. A similar set of results for the density inversion layer is provided in Fig. IV–12. The heights in these figures are relative to the floor of the cuvette and the times are elapsed time relative to the start of cooling. The mushy zone height was specified as the centerline location corresponding to a 0.99 liquid volume fraction as determined by interpolation, and the vertical coordinate of the centerline numerical control volume with the maximum density was considered to be the top of the density inversion. Due to the finite nature of the grid, both heights exhibit step function characteristics.

TABLE IV–1. Numerical and experimental run parameters

Parameter	CASE 1	CASE 2	CASE 3
Cooling Rate	1°C/min	2°C/min	3°C/min
Initial Top Temp.	58.5°C	58.5°C	58.5°C
Initial Bottom Temp.	21°C	21°C	21°C
Ambient Temp.	22°C	22°C	22°C
Heat Loss Coefficient	24000 $\frac{\text{ergs}}{\text{°C}\cdot\text{cm}^2}$	24000 $\frac{\text{ergs}}{\text{°C}\cdot\text{cm}^2}$	24000 $\frac{\text{ergs}}{\text{°C}\cdot\text{cm}^2}$
Bulk Concentration	72 wt% H_2O	72 wt% H_2O	72 wt% H_2O
Permeability const. K_o	5.56×10^{-7} cm^2	5.56×10^{-7} cm^2	5.56×10^{-7} cm^2

Two sets of predictions are included in Fig. IV–11 and Fig. IV–12. The first set, denoted by the dashed lines, assumed thermodynamic equilibrium within each numerical control volume. The second set, denoted by the solid lines, included the non-equalibrium approximation which incorporates the nucleation criteria.

A comparison of the equilibrium and non-equilibrium predictions with the experimental data indicates that non-equilibrium effects must be included to accurately simulate the physical process. Without accounting for non-nucleation effects, the calculations grossly overestimate the growth rates of both the density inversion layer and the mushy zone. With the inclusion of non-equilibrium effects, the predictions were improved to within the experimental error. Based on these results, non-equilibrium predictions were used for all subsequent ground-based and microgravity predictions.

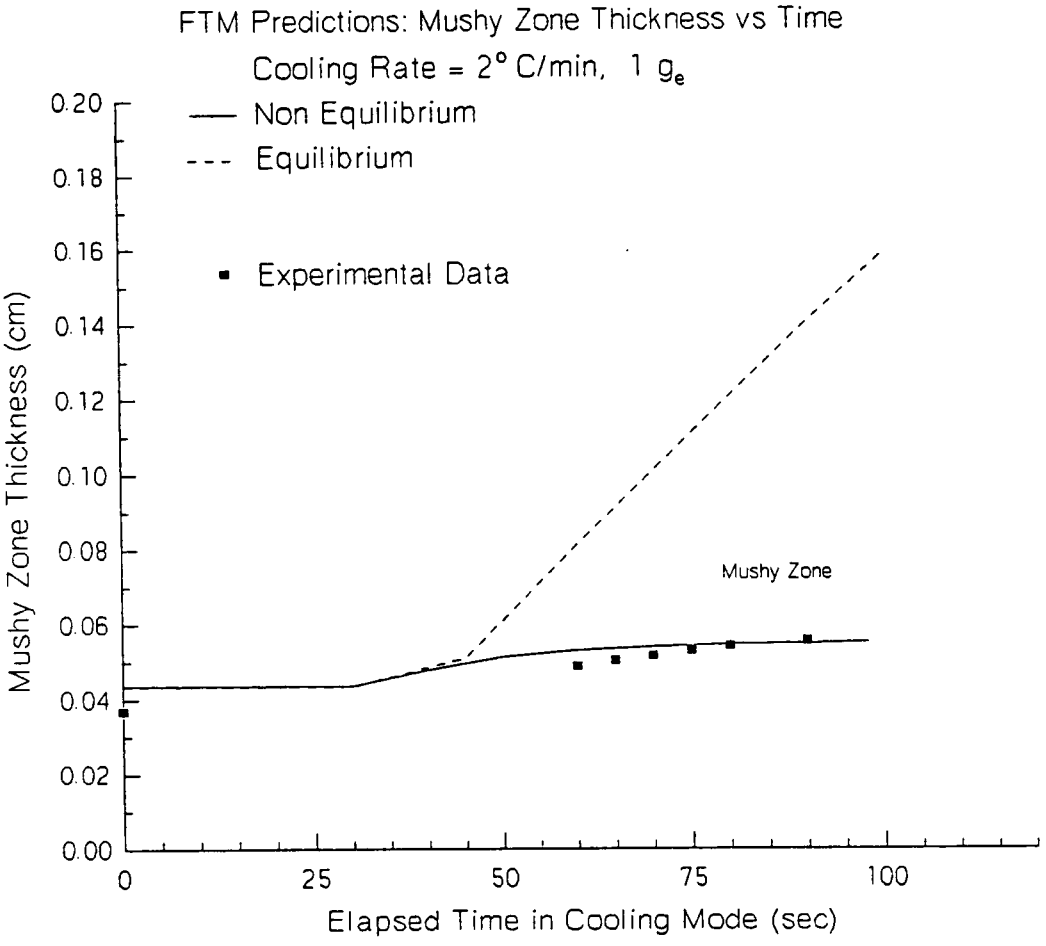

Figure IV–11. Mushy zone height vs. time. 2°C/min cooling rate: Numerical and experimental

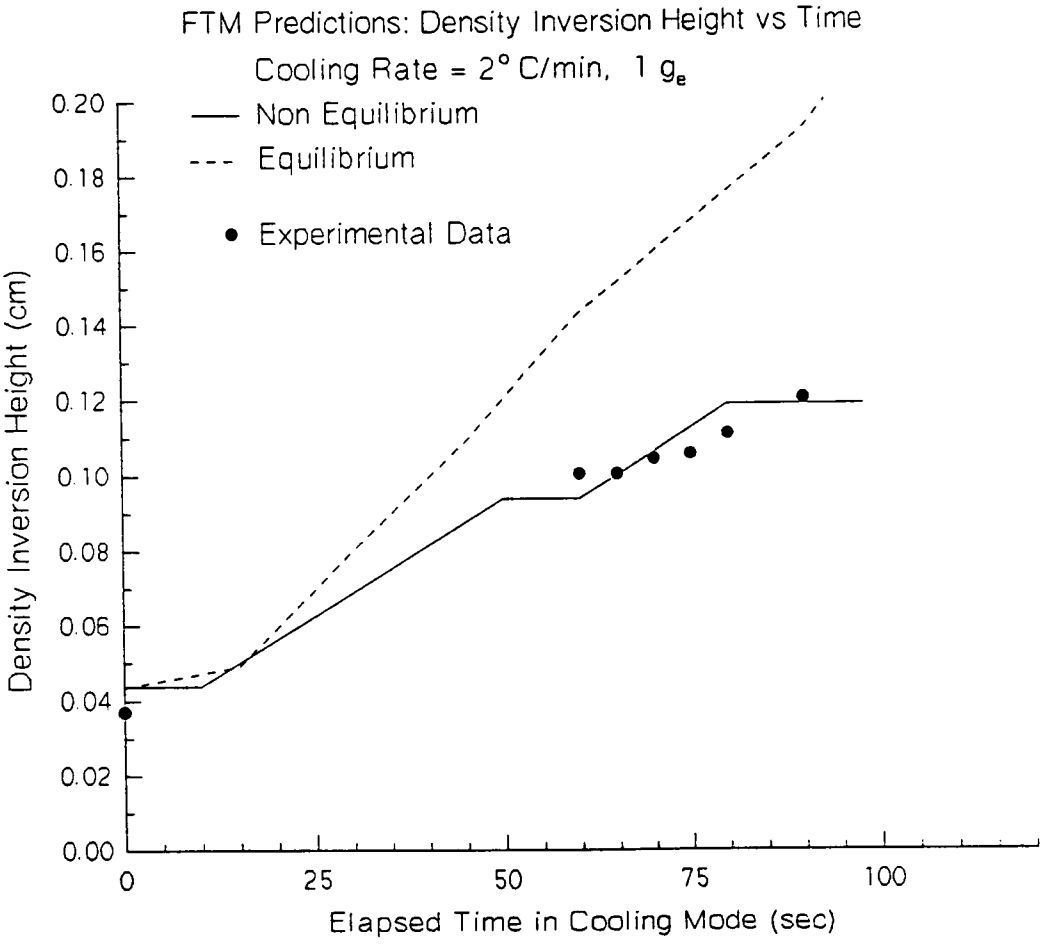

Figure IV–12. Density inversion height vs. time. 2°C/min cooling rate: Numerical and experimental

The incorporation of the nucleation criterion also provides a more accurate prediction of the transition from diffusion dominated to convection dominated solidification, i.e., convective breakdown. In the experiments, this transition is judged to occur when the the top of the density inversion layer, as indicated by a thick interferometric null, begins to undulate and form a series of cells.[4,5,7] Prior to this stage, the density field is primarily stratified with the exception of some small perturbations at the side walls. As soon as the null fringe begins to break into cells, however, the stratified density field deteriorates and strong buoyancy driven flows quickly ensue.[4,8] For the 2°C/min cooling rate ground-based experiment (Case 2), the observed onset of breakdown, based on the formation of these fringe cells, was 95 ± 10 seconds.[8]

In the numerical simulation, the onset of dominate convective activity was best indicated by the net kinetic activity in the domain. The computed net kinetic energy during directional solidification for Case 2 is given in Fig. IV–13, for both equilibrium and non-equilibrium predictions. The non-equilibrium prediction of the net kinetic energy in the cuvette indicated that after 75 seconds of cooling, convection begins to build rapidly and by 95 seconds the strength of the flow field, as reflected in the kinetic energy, has increased an order of magnitude. This predicted kinetic energy profile appears consistent with the significant increase in convective activity observed in the experiments[8] at 95 ± 10 seconds. In contrast, the equilibrium model did not predict any significant increase in kinetic energy until 135 seconds, well past the experimentally observed convective breakdown time.

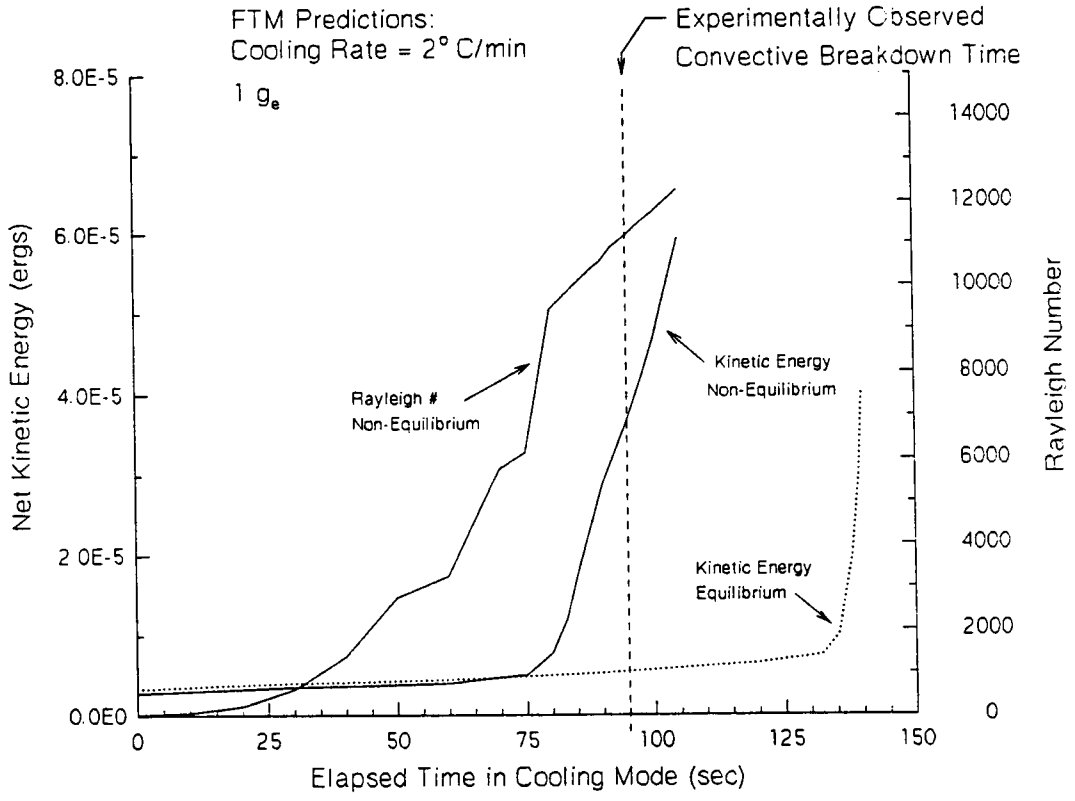

Figure IV–13. Numerical kinetic energy (KE) and combined Rayleigh number vs. time. 2°C/min cooling rate

Another indicator of the convective stability of the CAST double-diffusive system is the combined thermal-solutal Rayleigh number as proposed by Stern[30]:

$$Ra = \frac{g\beta_S(\Delta C_l)L^3}{\nu D} + \frac{g\beta_T(\Delta T)L^3}{\nu\alpha_T},$$

where 'L' is the appropriate length scale, i.e., the height of the density inversion layer[7]. ΔT and ΔC_l are the respective variations of temperature and concentration across this layer. When the resultant combined Rayleigh number exceeds a certain value, the critical Rayleigh number, the system becomes unstable and strong convective flows are expected to ensue.

At 95 seconds, the predicted critical combined Rayleigh number is 11,200 as shown in Fig. IV–13. This value is 1.4 times the experimental[8] critical combined Rayleigh number of 8150. The difference between the two can be accounted for by the fact that the experimental Rayleigh number incorporated a linear extrapolation of the solutal concentration across the density inversion layer to estimate ΔC_l, while the FTM used predicted values corresponding to a more realistic non-linear solutal profile. Considering this difference in the method of calculating the critical Rayleigh number and the sensitivity of Rayleigh number to the subjective determination of the precise time of breakdown, the correlation between the predicted and observed critical Rayleigh number is considered reasonable.

The next set of FTM results to be examined is the predicted evolution of the flow field, which directly affects the interface shape, the density distribution, and the solutal segregation during solidification. A review of the initial conditions (Fig. IV–7) shows that flows are predicted to be present prior to the initiation of the cooling phase of the experiment. The FTM predicts steady vortices in each of the lower corners during the thermal gradient hold. These upward flows are driven by the warmer side walls.

Figure IV–14 shows the status of the predicted flow field at the bottom of the cuvette after 60 seconds of cooling. The initial thermally driven vortices have increased in magnitude and counter-rotating rolls have appeared deep in the lower corners. These rolls have a maximum velocity of less than .001 cm/sec. The lower left of these rolls is evident in the expanded velocity vector plot at the bottom of Fig. IV–14. These embryonic vortices are driven by the lateral solutal gradients caused by non-uniform solidification along the cuvette bottom due to the warmer side walls. If the lower left vortex in Fig. IV–14 were instead directly driven by thermal effects, the flow would have been clockwise, corresponding to the warmer side wall to the left.

By 90 seconds, during the transition to convection dominated solidification, the developing corner solutal rolls have formed doublets and strengthened over an order of magnitude compared with their magnitude at 60 seconds. Their maximum velocities at 90 seconds are on the order of 0.02 cm/sec (Fig. IV-15). By 110 seconds these cells extend upward over 0.5 cm and have propagated across the cuvette bottom as shown in Fig. IV–16. In addition, four new cells are forming along the bottom of the cuvette as evident in the streamline plot.

The predicted thermal and solutal distributions corresponding to the cooling phase of Case 2 are shown in Fig. IV–17 and Fig. IV–18, respectively. The temperature field shows the effects of solutal rolls. It also indicates that the lower side walls are warmer than the neighboring solution, providing the lateral variation in solidification which creates the lateral gradients in the solutal concentration. Solutal contours, along with an outline of the mushy zone, are provided in Fig. IV–18 for 60, 90, and 110 seconds into the cool down. As with the thermal profiles, the influence of convection is clearly evident after the onset of significant convection at approximately 90 seconds.

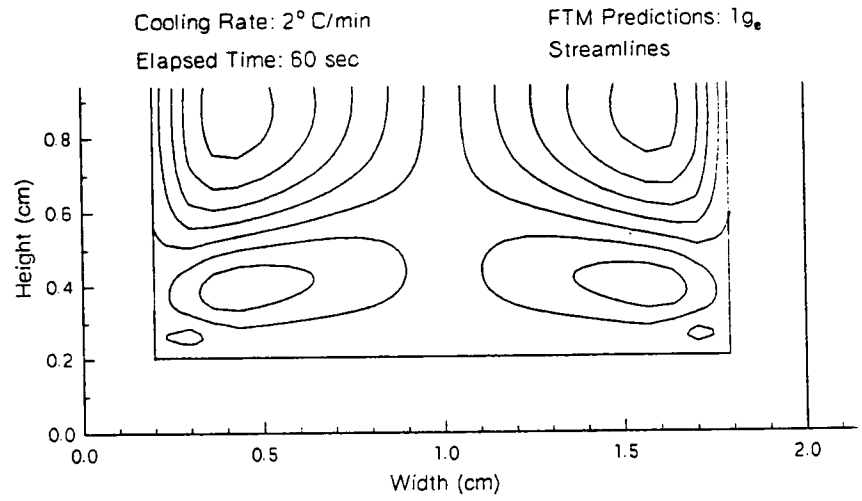

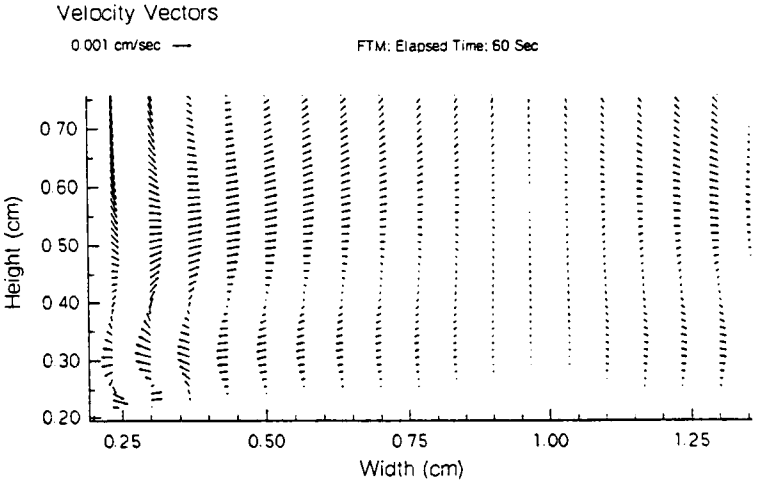

Figure IV–14. Predicted flow pattern at t = 60 sec. 2°C/min cooling rate: Streamlines and velocity vectors

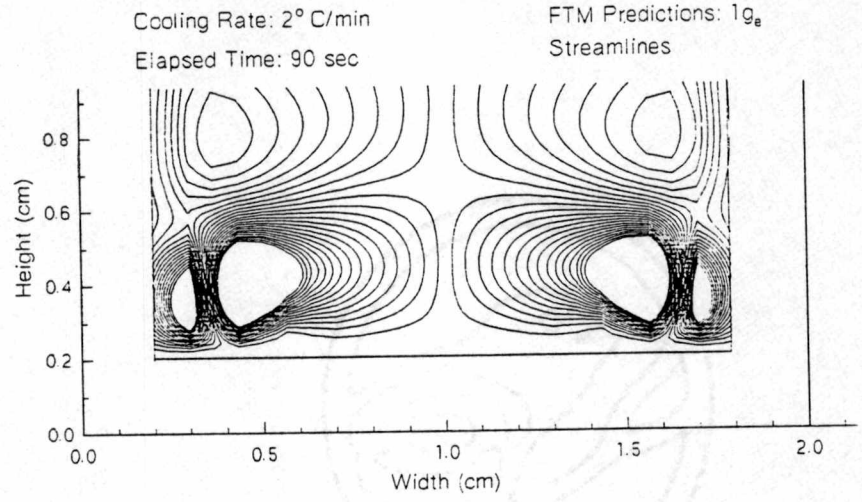

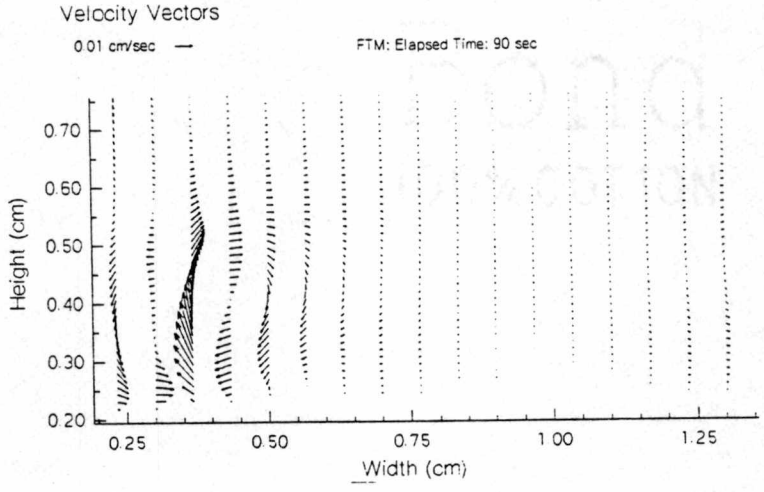

Figure IV–15. Predicted flow pattern at t = 90 sec. 2°C/min cooling rate: Streamlines and velocity vectors

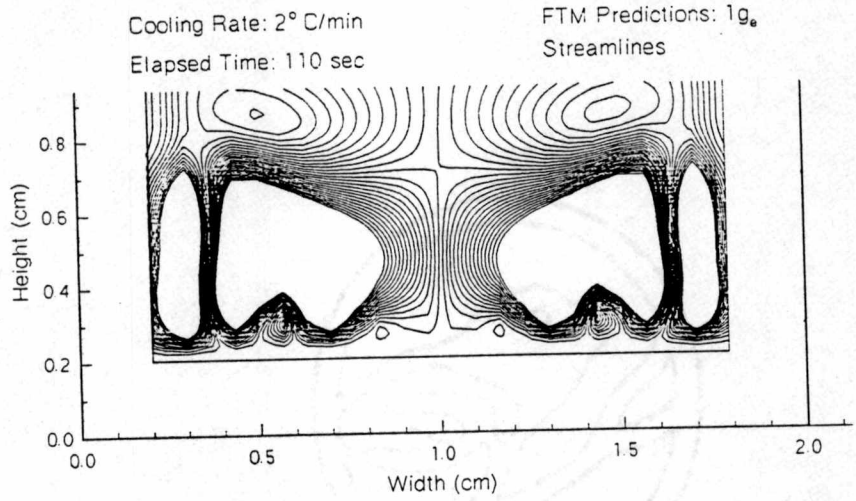

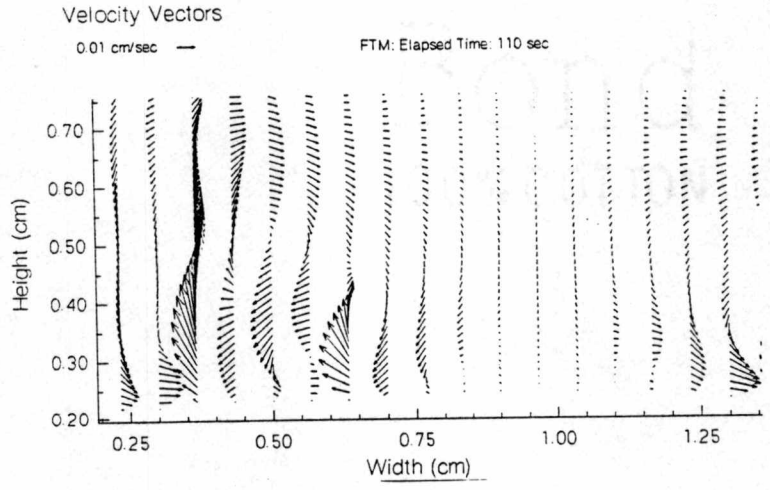

Figure IV–16. Predicted flow pattern at t = 110 sec. 2°C/min cooling rate: Streamlines and velocity vectors

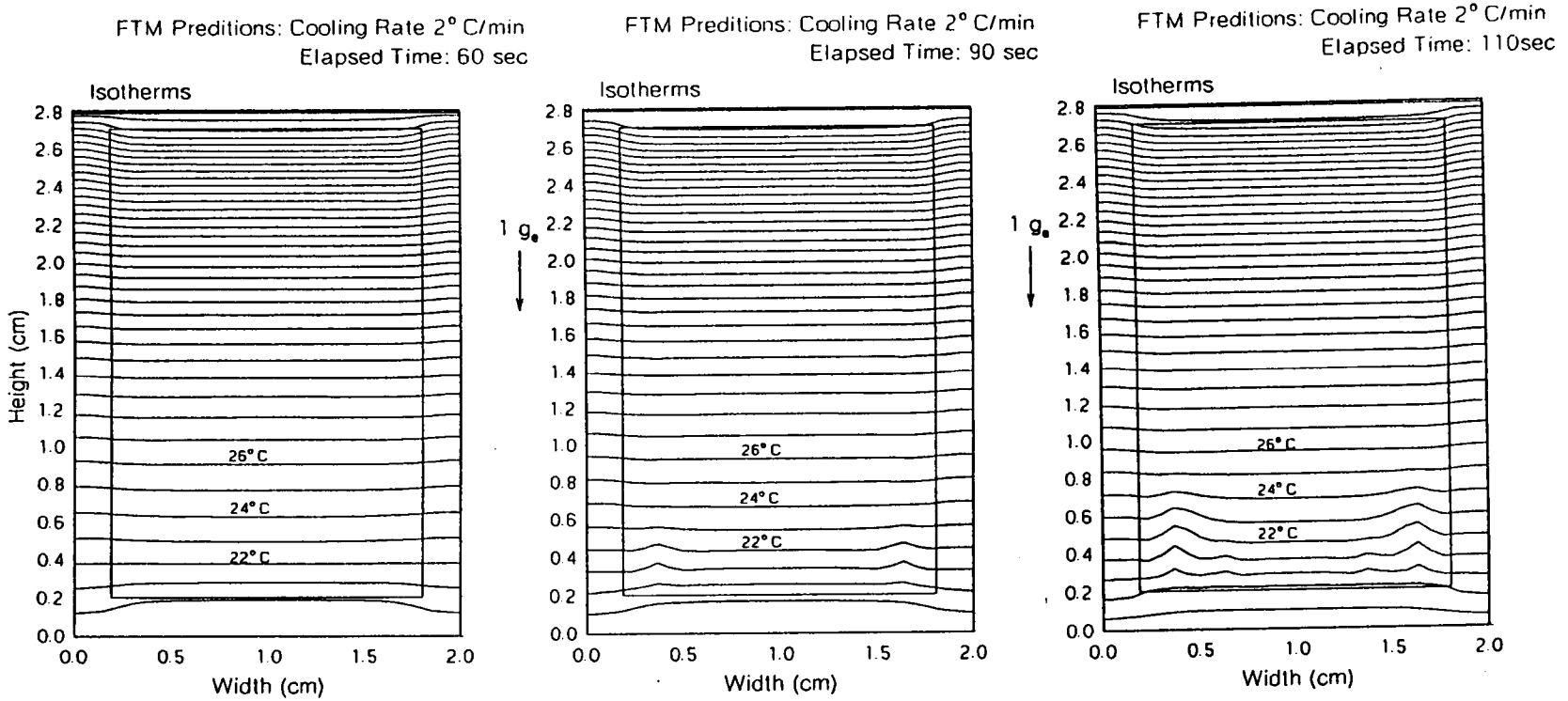

Figure IV–17. Predicted thermal history. 2°C/min cooling rate; Isotherms: (a) Pre-breakdown (t = 60 sec); (b) Transition (t = 90 sec) (c) Post-breakdown (t = 110 sec)

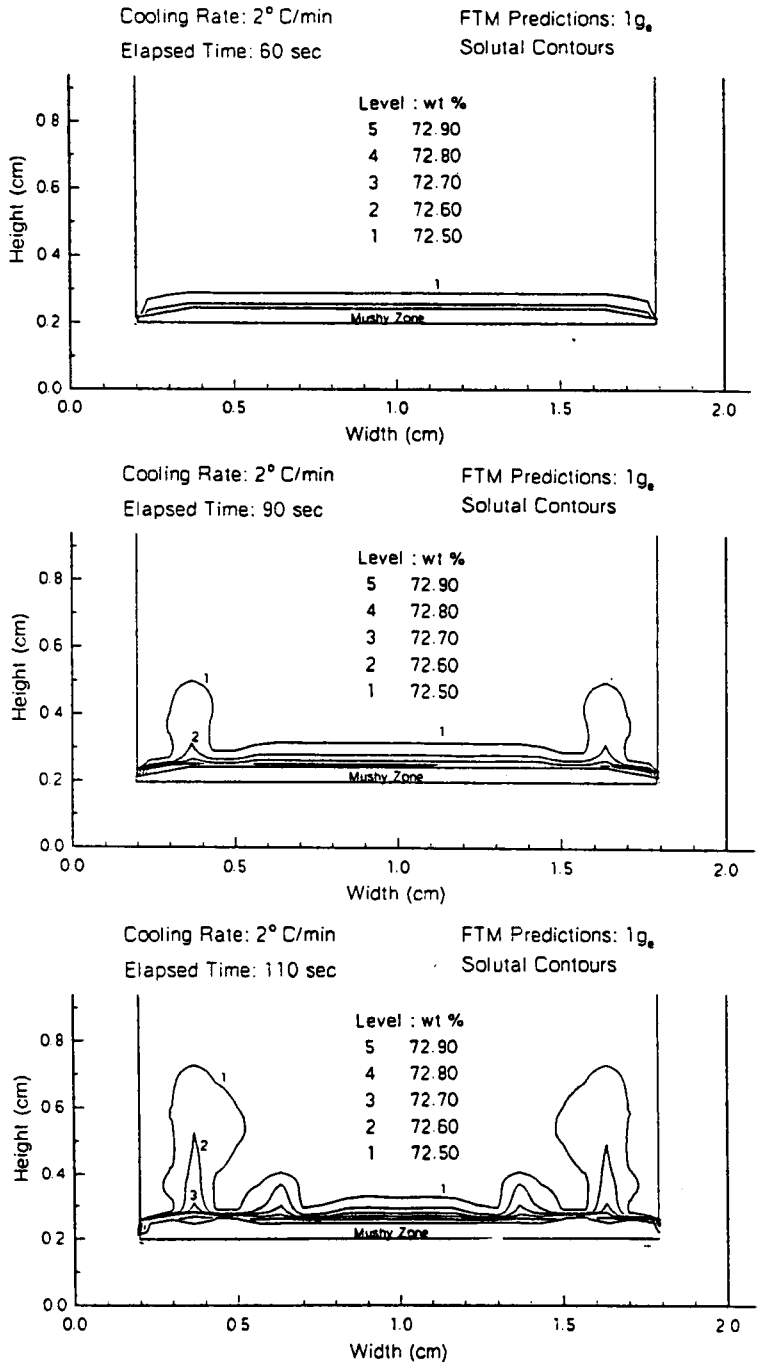

Figure IV–18. Predicted concentration distribution history. 2°C/min cooling rate; Contours: (a) Pre-breakdown (t = 60 sec) (b) Transition (t = 90 sec) (c) Post-breakdown (t = 110 sec)

Examination of the mushy zone outline shows that at 110 seconds the interface is developing a depression due to a locally high concentration of solute underneath the solutal plumes. These depressions correspond to the onset of channeling.[46]

Figure IV–19 provides the predicted centerline solutal concentration as a function of height at 60, 90, and 110 seconds after initiation of cooling. The linear segments of the profiles are in the mushy zone where the concentrations are directly related to the linear thermal profiles via the phase diagram. To the right of these straight line segments, denoted by 'mz' and corresponding to the limit of the mushy zone, is the solutal boundary layer ahead of the mushy zone. This has been measured experimentally[8] and is included on the plot for 60 and 92 seconds. The correlation between the prediction and data is within the $\pm.04$ wt% measurement error.

The temperature and solutal fields directly determine the density distribution of the liquid. Figure IV–20 provides the computed density contours for Case 2 at 60, 90, and 110 seconds. The spacing between contours represents a change in density of 1.43×10^{-4} gm/cm^3. Again, the effects of the convective flow after transition are clearly evident. One means of verifying the combined temperature and solutal fields is to examine their combined effect on the index of refraction of the liquid. This is done by calculating interferograms using the predicted index of refraction. In order to compare the numerical and experimental interferograms, a split image composite is presented in Fig. IV–21. Because of the symmetry of the experiment, the two halves of this composite should mirror each other. The left-hand side shows the experimental fringes, the right-hand side provides the simulated numerical fringes after 60 seconds of cooling. The five dots on the left are scaling marks spaced 1mm apart. The dark region at the left-hand bottom of the cuvette is the mushy zone. On the right-hand side, the predicted mushy zone

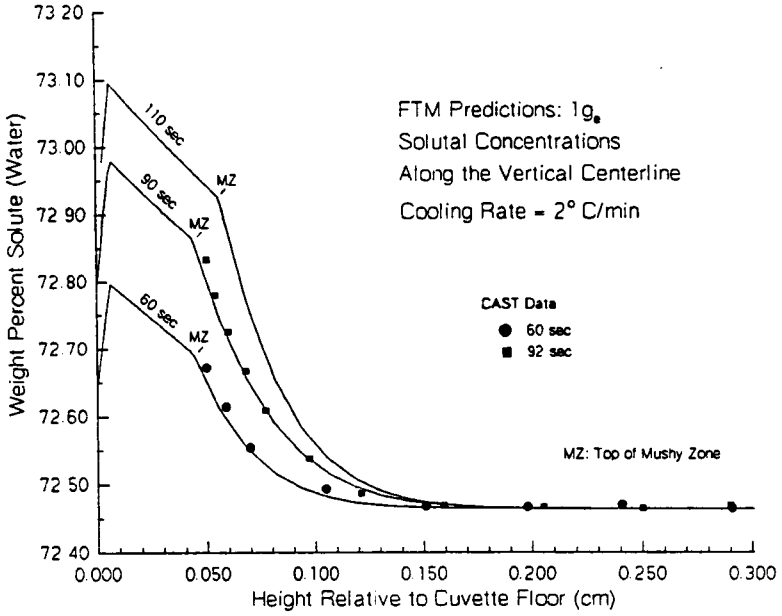

Figure IV–19. Predicted concentration distribution history. 2°C/min cooling rate: Concentration vs. height (t = 60, 90, and 110 seconds)

height is shown for comparison. Above the mushy zone, the experimental fringes have begun to show a slight effect of the vortices developing in the lower corners, as predicted, but the system is still stratified and the transport of heat and mass is primarily by diffusion.

A subsequent interferometer comparison is provided in Figure IV–22 during convective breakdown at 90 seconds into the cooling phase. The FTM image indicates significantly perturbed fringes at the side wall. The extent of this perturbation is consistent with the experimental image within the resolution of the relatively coarse lateral dimensions of the numerical grid cells. These rapidly developing perturbations portend the complete breakdown of the stratified density inversion layer. In the laboratory experiment, the subsequent deterioration of

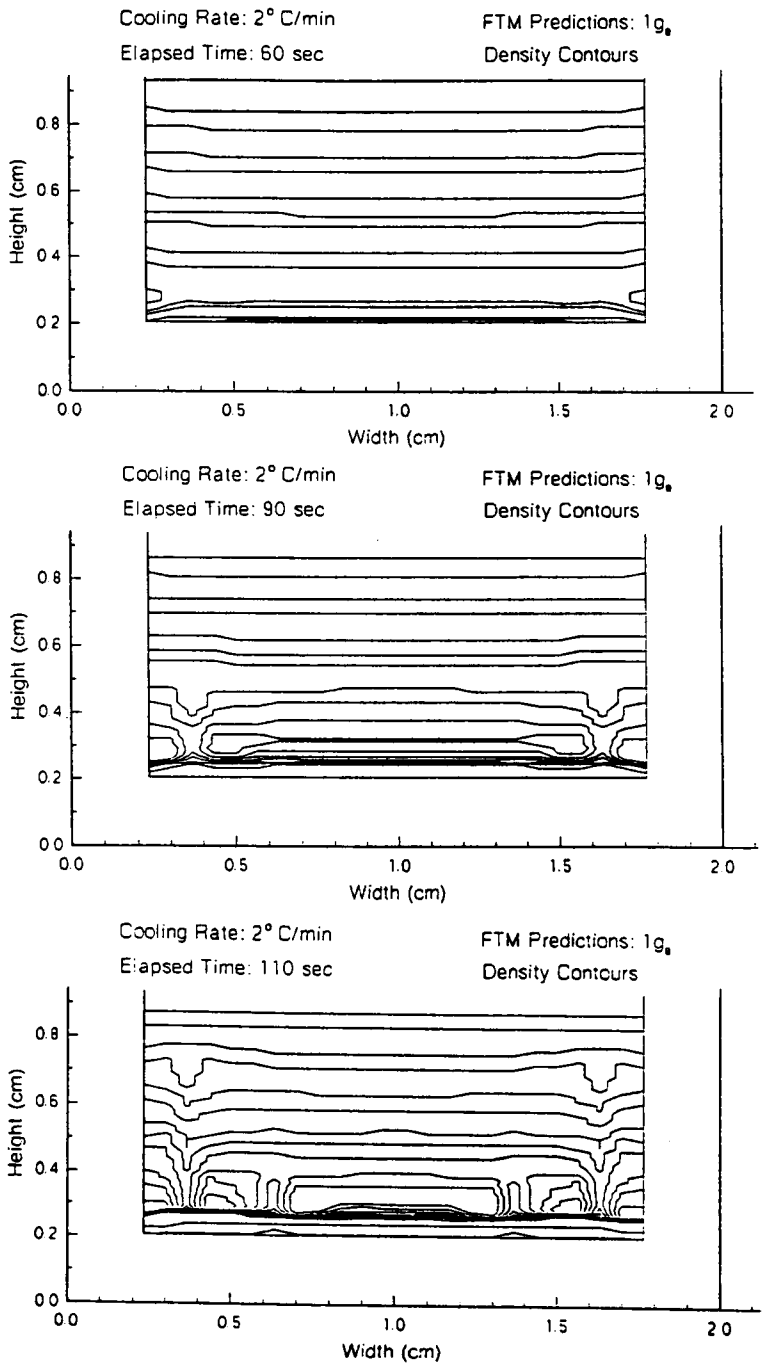

Figure IV–20. Density distribution history: 2°C/min cooling rate; Contours: (a) Pre-breakdown (t = 60 sec) (b) Transition (t = 90 sec) (c) Post-breakdown (t = 110 sec)

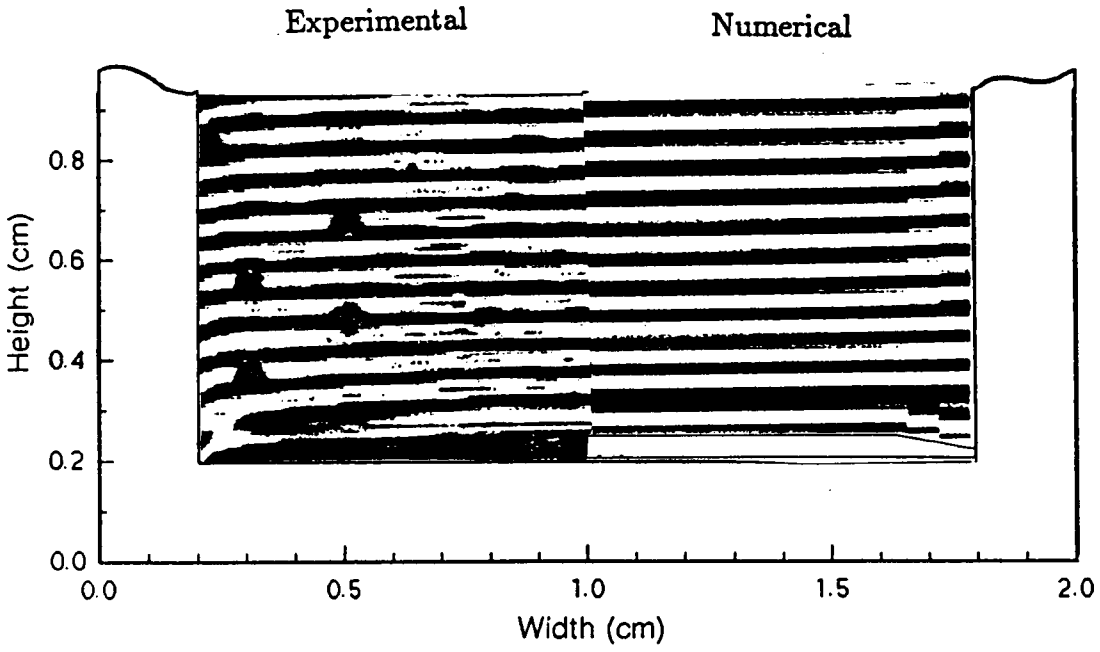

Figure IV–21. Interferometer fringe comparison (experimental vs. numerical): 2°C/min cooling rate: Pre-breakdown (t = 60 sec)

the layer occurs nearly simultaneously across the cuvette. In the numerical computations, the breakdown flows propagate inward from the sides of cuvette more slowly, leaving the center relatively unperturbed. This contrast in the extent of the breakdown is evident in the comparison of the post convective breakdown fringe patterns in Fig. IV–23. This limitation in the extent of the predicted convection and its effect on the fringe pattern most likely occurs because the FTM is two-dimensional and does not include the effects of flow structures developing on the front and back walls of the cuvette. If the FTM were three-dimensional, it could predict analogous flows on the front and back walls. These flows are expected, since lateral gradients, caused by the mismatch in the conductivity between the solution and the quartz, must exist perpendicular to those surfaces, as they at the side walls. In the experiment, front and back wall flows would affect the interferometer images and could also expedite convective breakdown by providing additional perturbations to the system.

In general, the predicted results indicate that the FTM is capable of predicting the transient two-dimensional thermal and solutal fields during the diffusion dominated phase of the ground-based solidification and should accordingly simulated the diffusion dominated solidification in microgravity as well. The ability to compute the three-dimensional flow pattern associated with the convective breakdown on the ground is not critical for predicting the microgravity experiments, and thus the two-dimensional model is considered adequate for the task.

The two other ground-based cases listed in Table IV–1 were also simulated. Figure IV–24 shows the predicted interface and density inversion growth for all three cooling rates, 1°C/min, 2°C/min, and 3°C/min. Figure IV–25 gives the kinetic energy and Rayleigh number temporal behavior for each. The predicted times of convective breakdown, as dictated by the steep rise in kinetic energy at

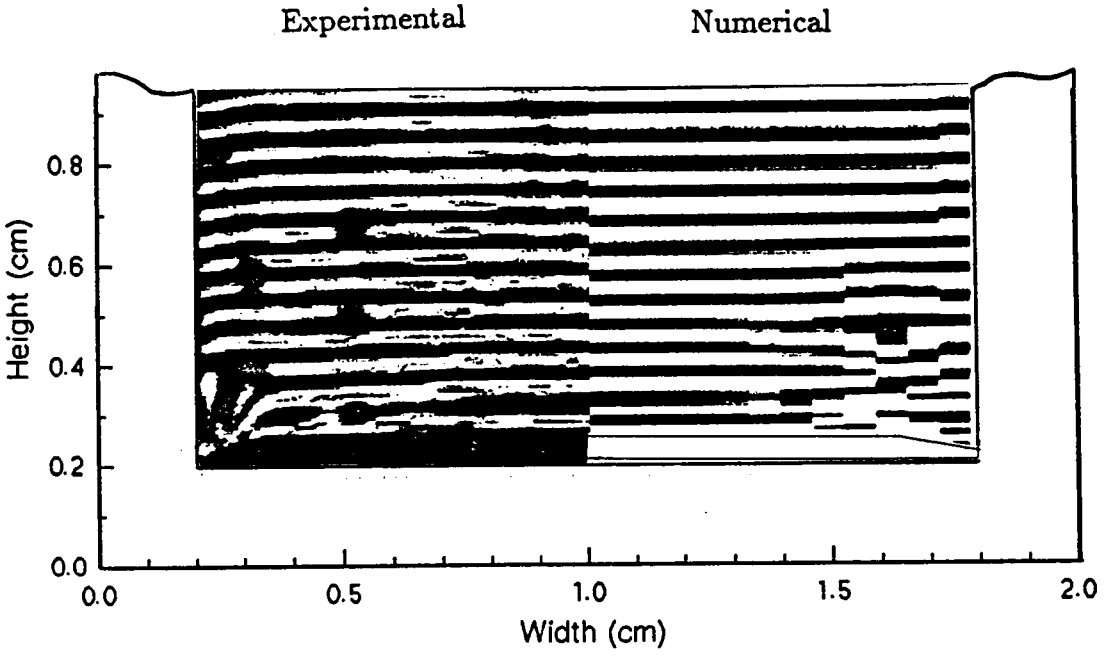

Figure IV–22. Interferometer fringe comparison (experimental vs. numerical): 2°C/min cooling rate: Transition (t = 90 sec)

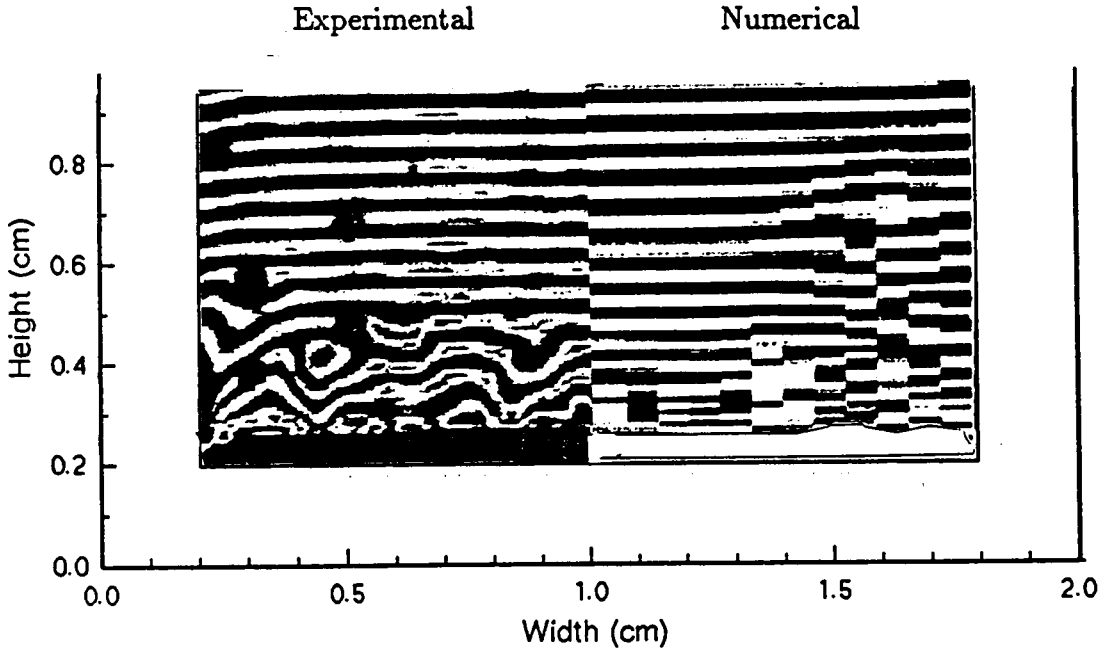

Figure IV–23. Interferometer fringe comparison (experimental vs. numerical): 2°C/min cooling rate: Post-breakdown (t = 110 sec)

approximately 1.7×10^{-5} ergs, are 140, 85, and 68 seconds for the respective cooling rates of 1°C/min, 2°C/min, and 3°C/min. The corresponding critical Rayleigh numbers fall in the range of 10,000 to 12,000. While there is limited experimental data for quantitative confirmation of these additional results, the trends are realistic and the correlation of a constant (approximately) critical Rayleigh number with breakdown is consistent.

In summary, the FTM was been tested in preparation for the CAST microgravity predictions. The first validation test was a comparison with experimental data for the thermally driven convection of water in a container. The results demonstrated qualitative agreement with the observed flow patterns. The next test was a quantitative comparison with numerical results from a validated model for the case of thermally driven natural convection of water. The correlation was found to be within 0.25°C (3%). After these thermal convection comparisons, the steady state capabilities of the FTM were tested by comparison with the initial conditions for the CAST ground-based runs. The predicted and experimental initial conditions were found, in general, to correlate closely. The predicted thermal and solutal field and the general shape of the interface agreed closely with the data. The major discrepancy was an error of 0.1 mm in the absolute height of the predicted mushy zone thickness. Based on the comparison with the experimental data, the FTM initial conditions were determined to be sufficiently accurate to use as starting conditions for the numerical simulation of the three CAST ground-based directional solidification runs. The results compared favorably with experimental parameters, including the thermal, solutal and density distribution, the growth of the mushy zone and density inversion layer, the formation of vortices at the side walls, and the time of convective breakdown for a 2°C/min cooling rate. A correlation between the numerically computed combined Rayleigh number and the time

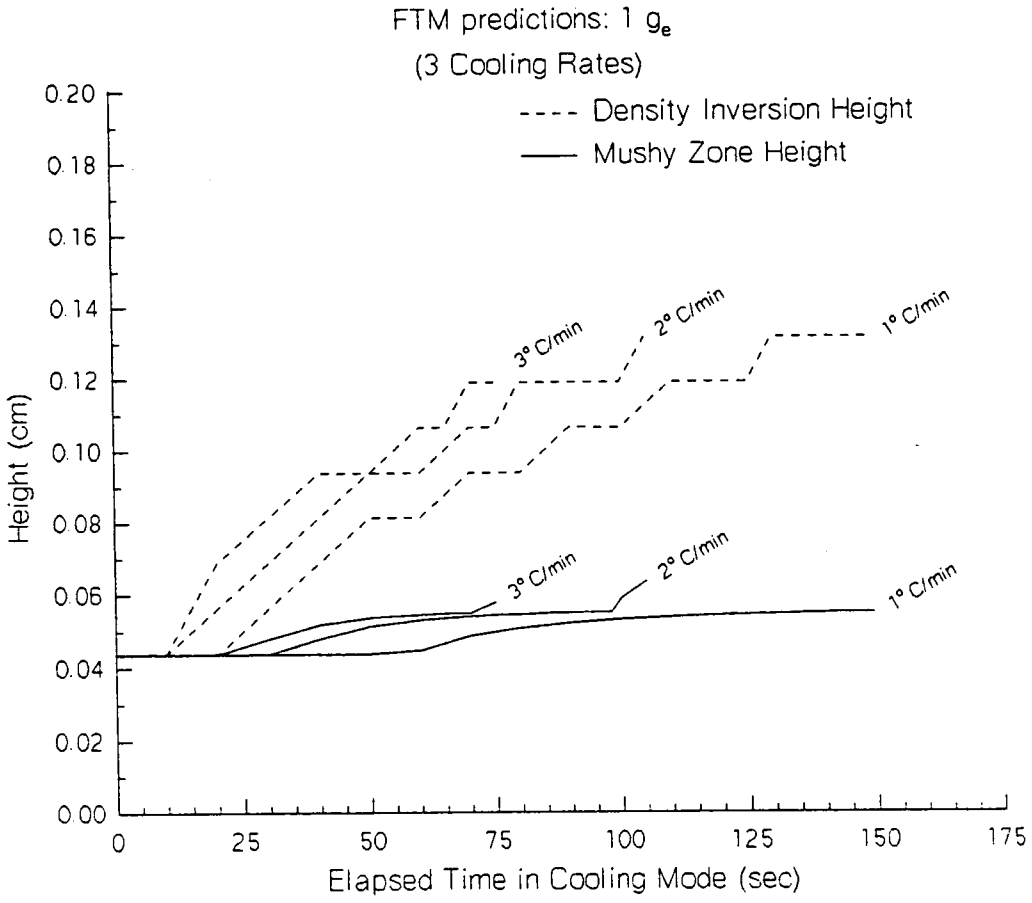

Figure IV–24. Mushy zone height and density inversion height vs. time for three different cooling rates: 1°C/min, 2°C/min, and 3°C/min

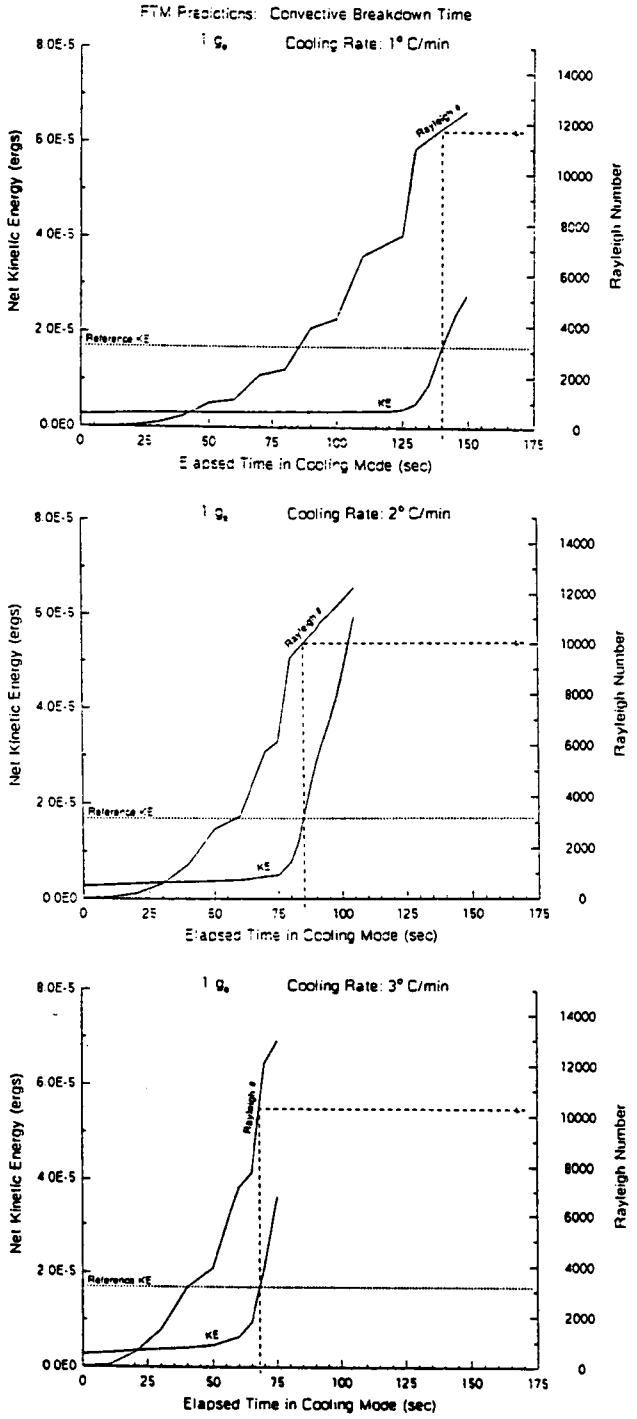

Figure IV–25. Numerical net kinetic energy and combined Rayleigh number vs. time for three different cooling rates: 1°C/min, 2°C/min, and 3°C/min

of convective breakdown was also demonstrated for three different cooling rates. The weakness of the FTM in modeling the transient, ground-based solidification was its inability to predict the effect of the fully three-dimensional flow pattern on the solutal and thermal distribution after convective breakdown. The capability to predict such flows is non-critical in this study, however, since the microgravity experiment does not entail vigorous natural convection. Based on these validation results, it was concluded that the essential elements needed to predict the CAST microgravity experiments have been incorporated into the FTM. The next step was to provide a sample prediction for a CAST microgravity run.

SECTION V

MICROGRAVITY PREDICTIONS

Introduction

The primary purpose of the FTM is to predict directional solidification of the metal analogue, NH_4Cl-H_2O, in a microgravity environment. The results presented here are for a planned run for the CAST experiment to be flown on the Shuttle International Microgravity Laboratory (IML-1). The sample cooling rate is 2°C/min, providing for direct comparison with the Case 2 ground-based results.

The information from this (and future) FTM microgravity simulations support the CAST study in several ways. Prior to the flight, the model results provide experimental planning guidance for selection of critical parameters such as the duration of the initial temperature hold, the values of the cuvette top and bottom temperatures, the rate of cooling, and the duration of cooling. The FTM predictions can also provide pre-flight guidance pertaining to data acquisition, such as the optimum camera view and time interval between holographic exposures. In addition, the numerical predictions indicate the relative significance of such potential phenomena as subtle microgravity flow patterns.

After the flight, the model will aid in data analysis, and conversely, the microgravity experimental results will provide additional benchmarks for the FTM. Key elements of the model, such as the nucleation criterion, become more critical at the extended space experiment growth times and will be thoroughly tested by the microgravity experiments. The comparison between the numerical results and flight data will either validate these basic model elements or indicate the necessary improvements. The final objective is an improved understanding of the solidification process.

FTM predictions for the 2°C/min cooling rate microgravity run are presented in this section and compared with analogous one-gravity results. The effects of reduced buoyancy driven convection and the implications for the space flight experiment are discussed.

Microgravity Run: Initial Conditions

The initial bottom and top boundary conditions of of 21°C and 58.5°C for the microgravity run are identical to those used for the one-gravity case, but the heat loss boundary condition at the side walls and the body force term are different and need to be reevaluated for the numerical simulation.

Orbital flight reduces the effective acceleration forces on a payload and accordingly reduces, but does not eliminate, buoyancy driven convection of fluids on board. The acceleration forces in the Shuttle environment are on the order of 1×10^{-5} g_e, with the magnitude and direction of the acceleration dependent on a number of transient phenomena such as thruster firings, crew movement, and the attitude of the spacecraft relative to earth. As a first approximation, the model assumes a steady acceleration vector of 1×10^{-5} g_e, aligned opposite to the growth direction. This level of acceleration is sufficient to generate natural convective flow for the microgravity steady initial conditions as illustrated in Fig. V–1. As with the one-gravity case, large convective cells form in response to lateral density gradients. At the reduced acceleration levels, these flows are predicted to be four orders of magnitude less than for the related initial state in one-gravity.

The low gravity levels on the Shuttle are also expected to reduce the cooling flows normally present on the external surfaces of the cuvette to the extent that the heat loss to the environment is assumed negligible for the microgravity numerical simulations. The effect of this reduced heat transfer on the initial

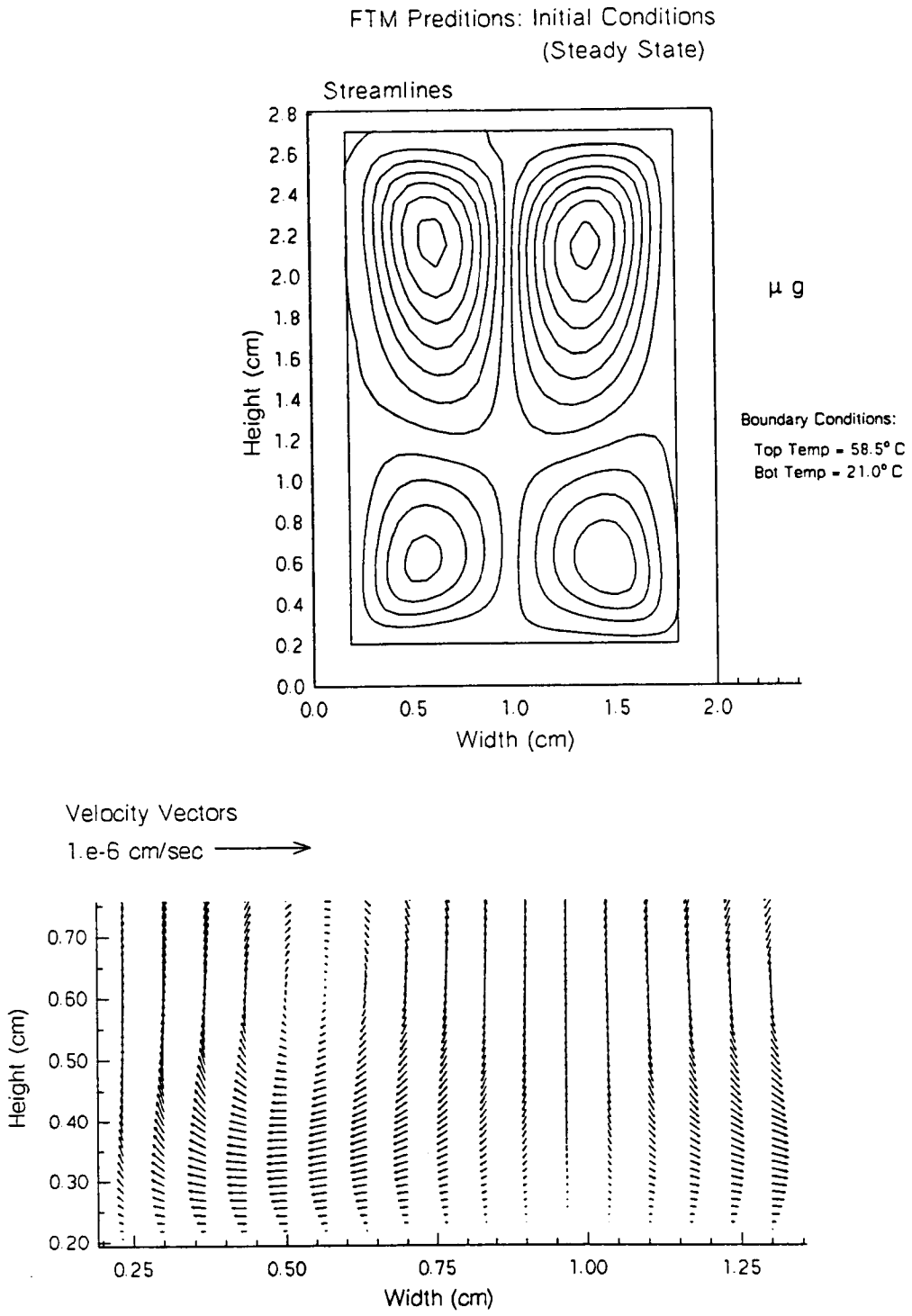

Figure V–1. Microgravity initial conditions: Predicted flow field. Top temperature = 58.5°C; Bottom temperature = 21°C (a) Streamlines (b) Velocity vectors (expanded view)

temperature distribution in the cuvette, as compared with the corresponding one-gravity prediction, is shown in Fig. V–2. Although the microgravity predictions still exhibit the lateral non-linear temperature gradients caused by the mismatch of the quartz and water-ammonium chloride solution conductivities, the vertical non-linearity of the temperature distribution is virtually eliminated. As a result, the gradient at the bottom of the cuvette has steepened approximately two-fold and the average temperature near the bottom of the cuvette is higher. This more linear temperature distribution directly affects the density distribution and the mushy zone height.

The resultant predicted mushy zone distribution for the microgravity steady state is provided in Fig. V–3. Compared with the the liquid fraction distribution computed for the initial conditions in one-gravity, the mushy zone height in microgravity is predicted to be smaller by .13 mm (.31 mm vs. .44 mm at the vertical centerline). At the edges, the mushy zone is predicted to melt back completely, due to the reduced heat loss, and no longer covers the bottom of the cuvette as it did under one-gravity conditions. The average liquid solutal concentration corresponding to the reduced mushy zone in the IML initial state prediction is 72.315 wt% solute as opposed to 72.465 wt% for the one-gravity case.

Thus, although the initial end temperatures of 21°C and 58.5°C are the same for both the one-gravity and microgravity initial gradient hold, the resulting steady state for the IML CAST experiment is expected to be different. The FTM predicts that in microgravity the temperature distribution will be more linear, the mushy zone reduced, the average liquid concentration lower, and the flow velocities significantly smaller. These numerical results were used as the initial conditions for the microgravity directional solidification simulation below.

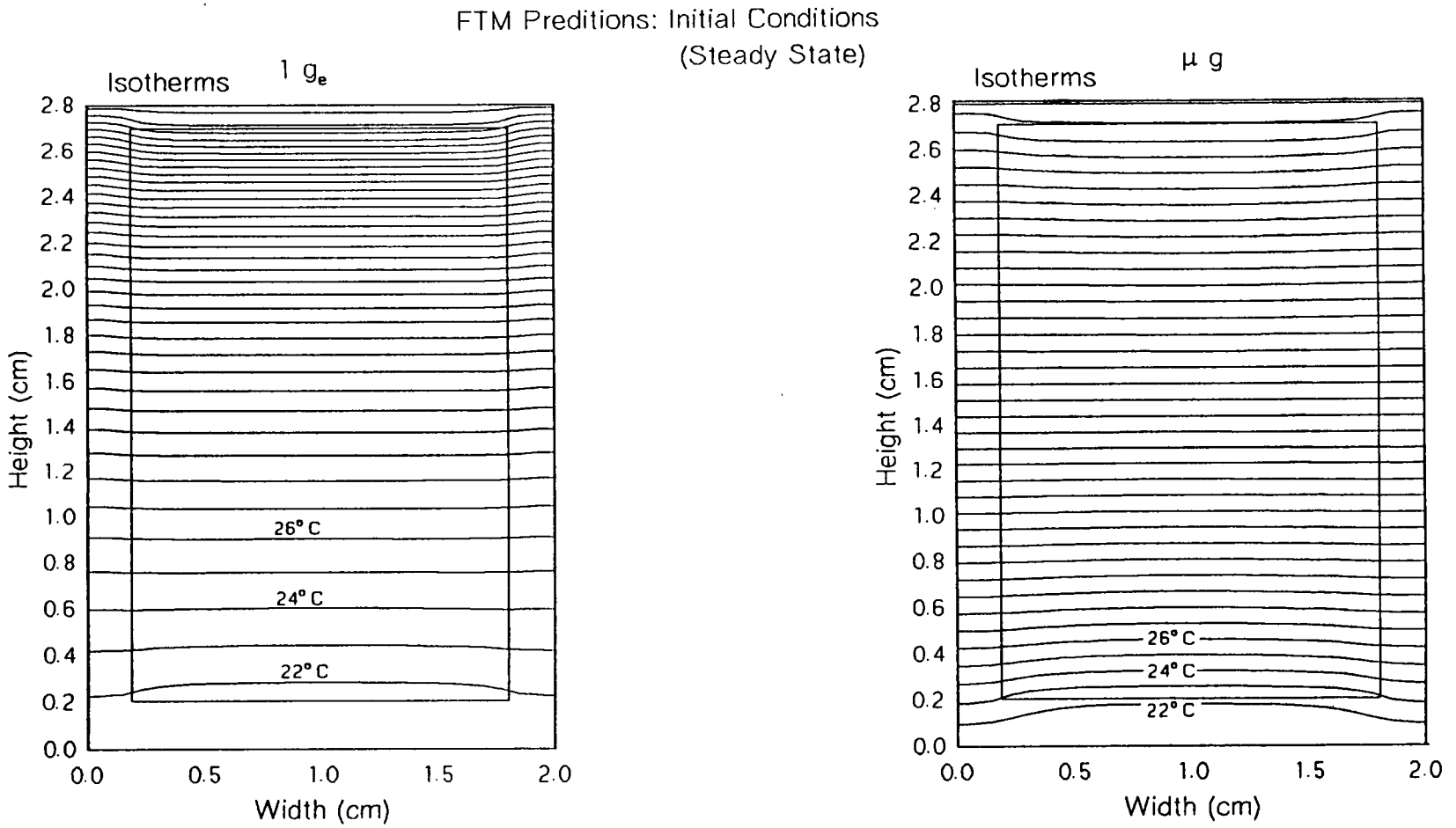

Figure V–2. Microgravity initial conditions: Predicted temperature distribution. Top temperature = 58.5°C; Bottom temperature = 21°C (a) One-gravity (b) Microgravity

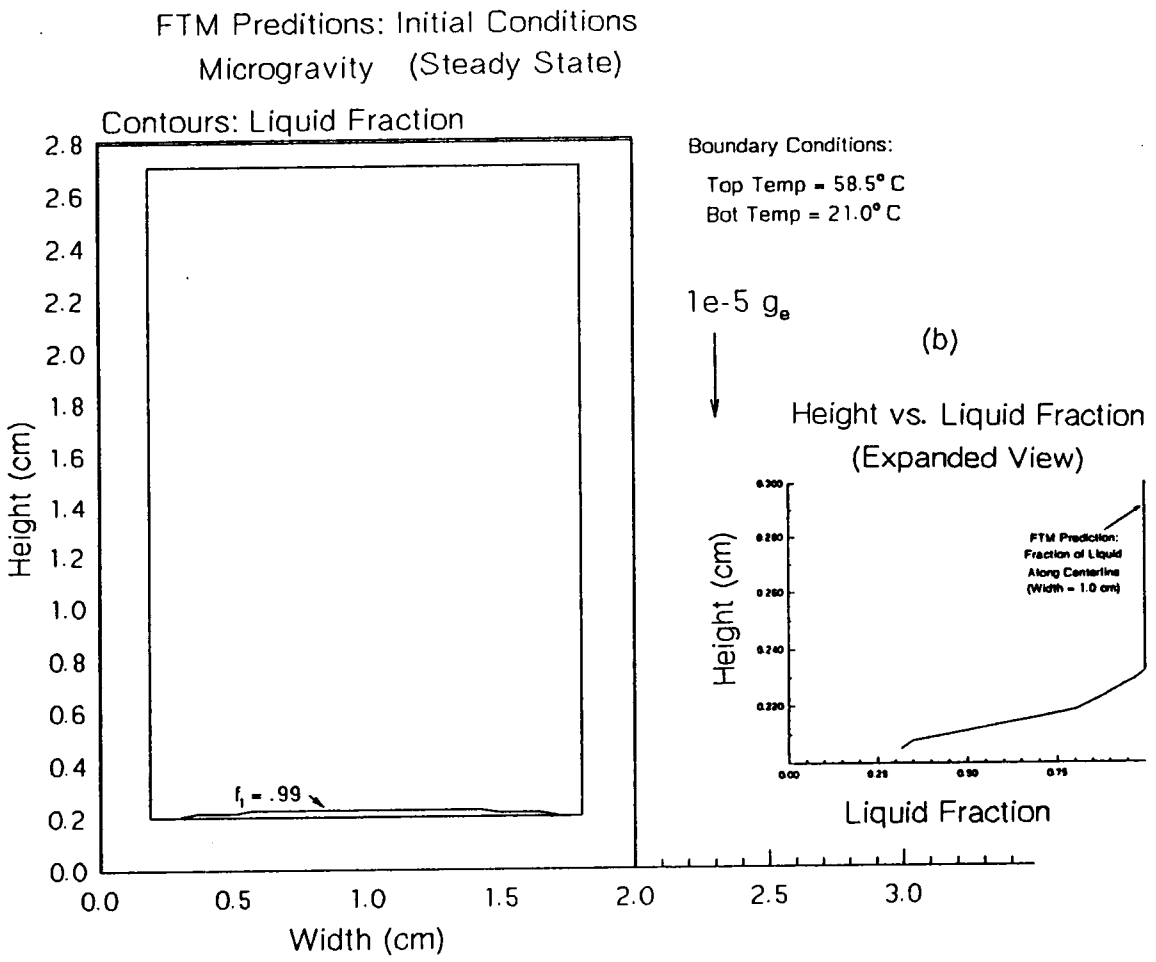

Figure V–3. Microgravity initial conditions: Predicted liquid fraction distribution. Top temperature = 58.5°C; Bottom temperature = 21°C (a) Contours (b) Liquid fraction vs. height (centerline)

Microgravity Run: Directional Solidification

As with the ground experiments, the cuvette and the NH_4Cl-H_2O solution are cooled at a specified rate in order to induce directional solidification. The specified cooling rate for these calculations was 2°C/min and the resulting growth rates of the mushy zone and density inversion layer are shown in Fig. V–4.

The initial growth rates for the one-gravity and the microgravity runs are predicted to be similar, despite the difference in the initial conditions and gravity levels. This is because the early stage of the ground-based experiments was designed to minimize convection and thus, like the microgravity run, was diffusion dominated. However, above a critical Rayleigh number the ground-based experiment becomes convection dominated with a resulting rapid growth of the mushy zone and the disruption of the inversion layer (not shown). In contrast, the mushy zone and inversion layer in microgravity continue to grow smoothly, unperturbed by strong convective flow.

After 10 minutes of cooling in microgravity, the growth rates of the mushy zone and density inversion layer are predicted to approach an approximately constant value of 1.19×10^{-3} cm/sec as shown in Fig. V–4. The absolute difference between the density inversion, which corresponds closely with the extent of the solutal boundary layer, and the height of the dendritic zone is .065 cm during the steady growth phase. The steady nature of this growth is confirmed by the concentration distribution in Figure V–5 which shows that at 800 seconds the predicted solutal distribution in front of the advancing front is close to the classic exponential distribution for steady state growth.[73]

Figure V–6 provides the net kinetic energy and the combined Rayleigh number for both the ground-based and microgravity run. The kinetic energy and

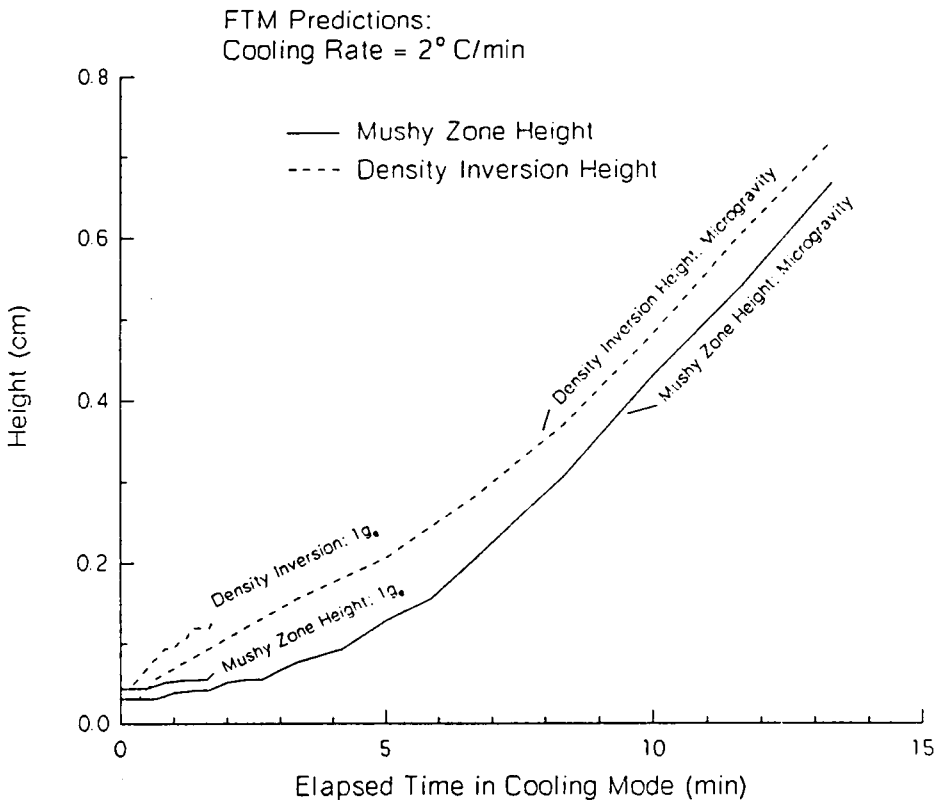

Figure V-4. Predicted mushy zone height and density inversion height vs. time. 2°C/min cooling rate: One-gravity and microgravity

Rayleigh number are predicted to remain small over the full course of the microgravity experiment. The result is a diffusion dominated process, void of the significant convective transport of energy and mass that occur post-breakdown in the one-gravity environment. This contrast can be seen in the comparison of solutal contours in Fig. V–7. After the point at which convective effects are clearly evident in the ground-based run, the microgravity case continues to develop with a uniform diffusion front.

The convection that is predicted to occur during the microgravity solidification is primarily caused by contraction of the material due to cooling and phase change. Figure V–8 provides numerical particle tracks and velocities for the flight experiment after 800 seconds of cooling. The dominant flow is fluid being drawn from the supply tube. The magnitude of these contraction flows is on the order of 1×10^{-5} cm/sec and they obscure the weaker (two orders of magnitude) natural convection flows that were evident in the initial state in Fig. V–1. The corresponding mushy zone and solutal distribution at 800 seconds from the start of cooling is given in Fig. V–9. While these contours exhibit some irregularities, they are still predominantly planar, as expected for diffusion dominated directional solidification.

In general, the FTM predicts that the reduction of buoyancy driven convection in microgravity influences virtually every aspect of the directional solidification experiment including the establishment of the initial conditions for which the lack of convective cooling external to the cuvette makes the internal temperature more linear and reduces the extent of the initial mushy zone. The most significant effect of the microgravity environment is that the combined solutal and thermal Rayleigh number remains below a critical value over the course of the experiment, allowing the heat and mass transport in the system to remain diffusion dominated and the

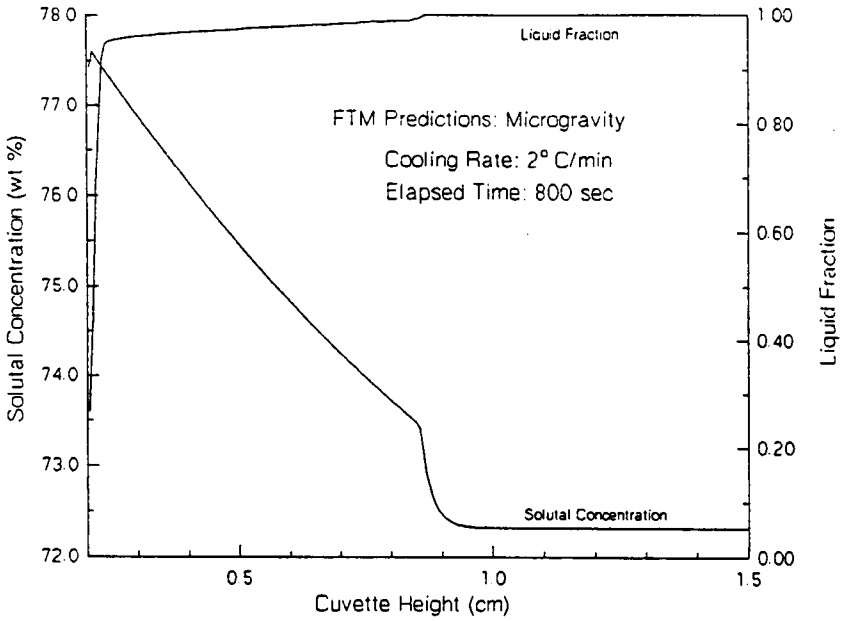

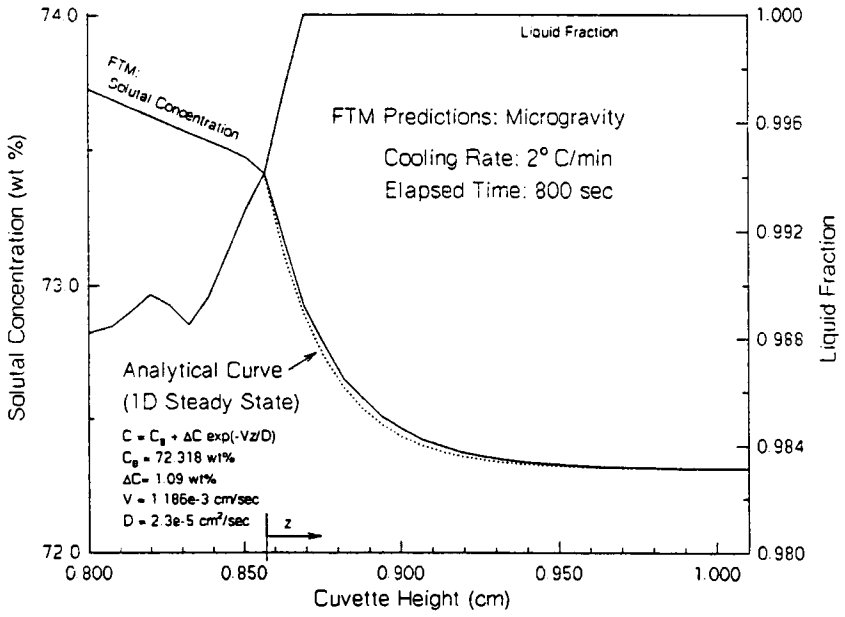

Figure V–5. Predicted solutal concentration distribution and fraction of liquid vs. height (centerline) in microgravity. 2°C/min cooling rate: Elapsed time = 800 sec

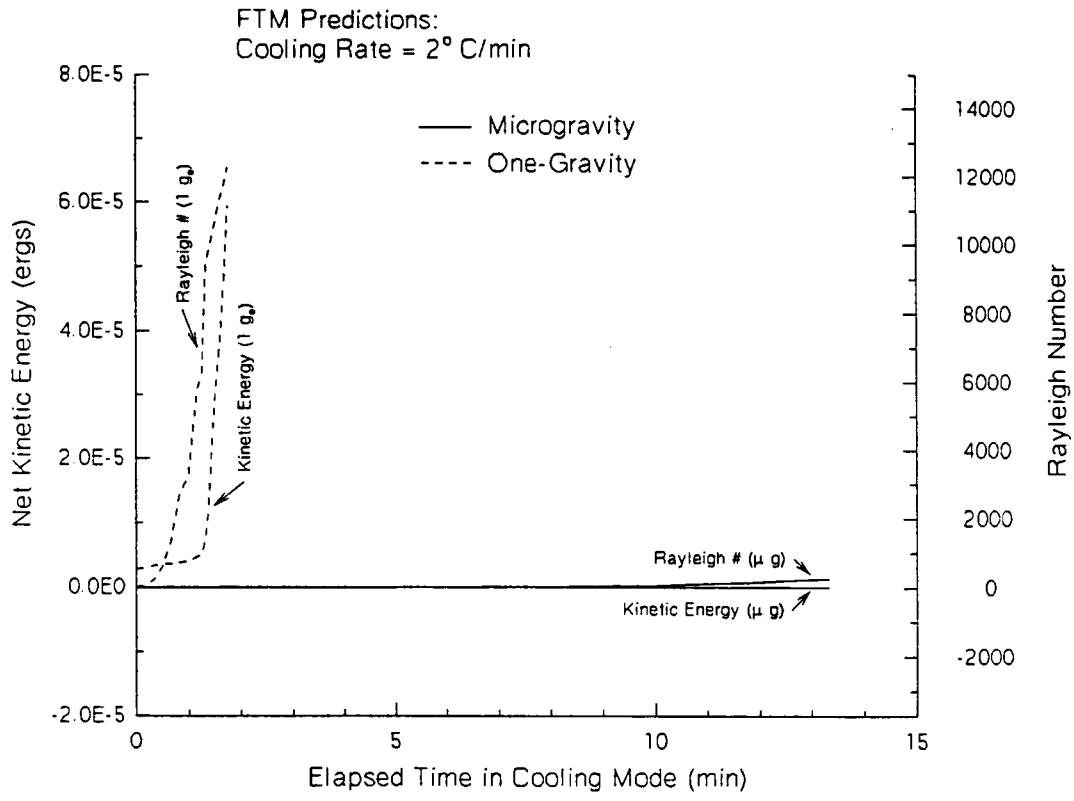

Figure V–6. Predicted net kinetic energy (KE) and combined Rayleigh number vs. time. 2°C/min cooling rate: One-gravity and microgravity

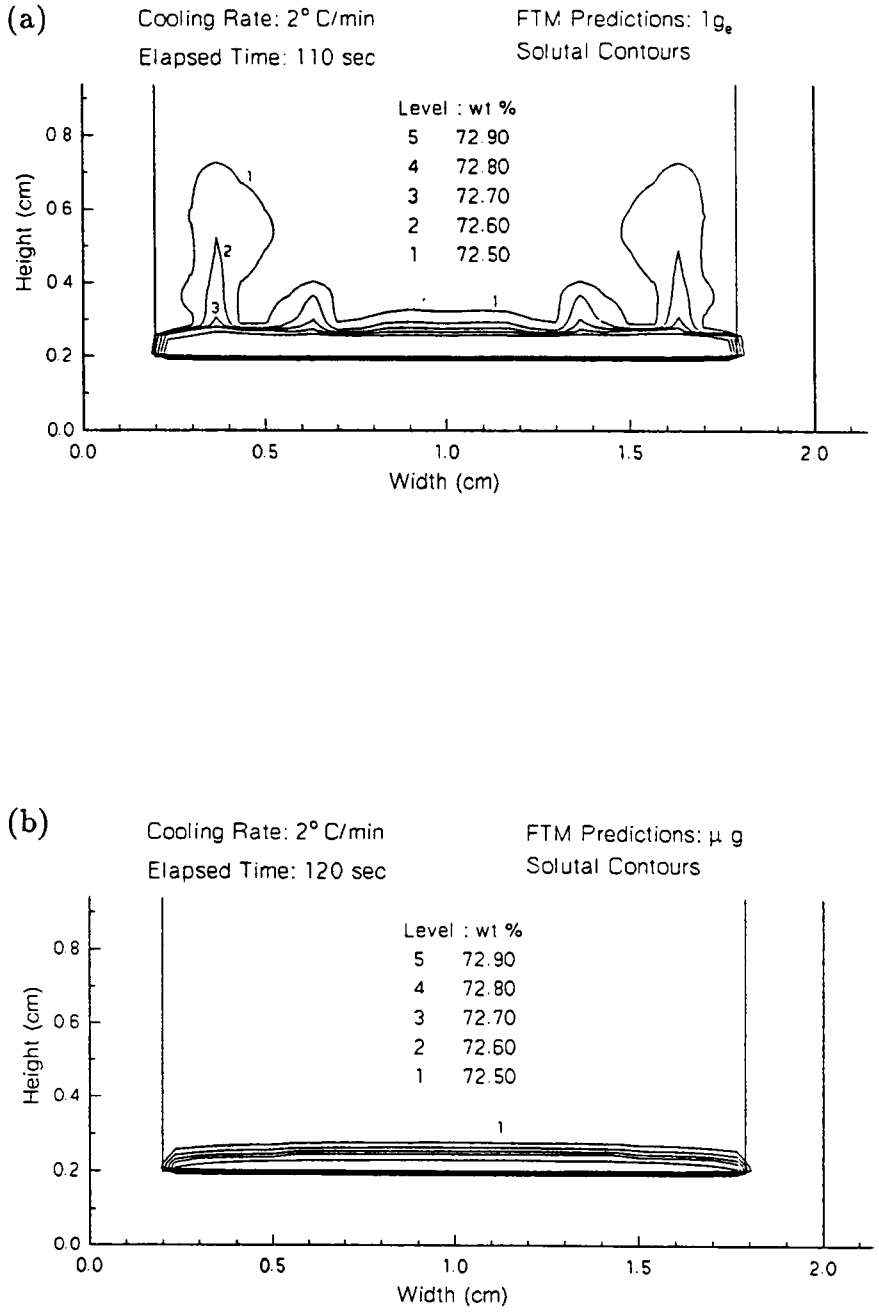

Figure V-7. Predicted solutal concentration contours. 2°C/min cooling rate: (a) One-gravity (110) (b) Microgravity (120)

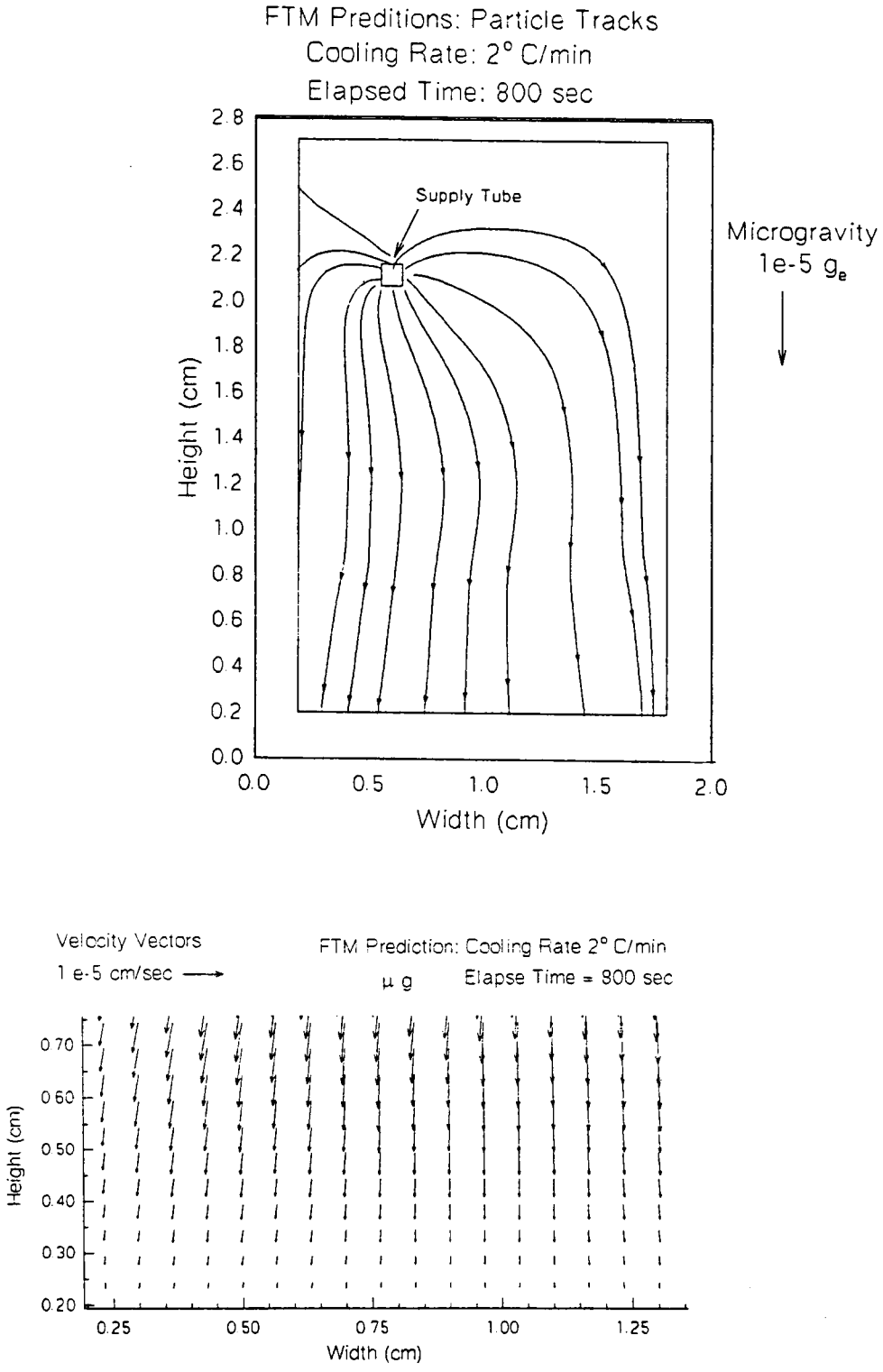

Figure V–8. Predicted microgravity flow field. 2°C/min cooling rate: Elapsed time = 800 sec: (a) Particle tracks (b) Velocity vectors

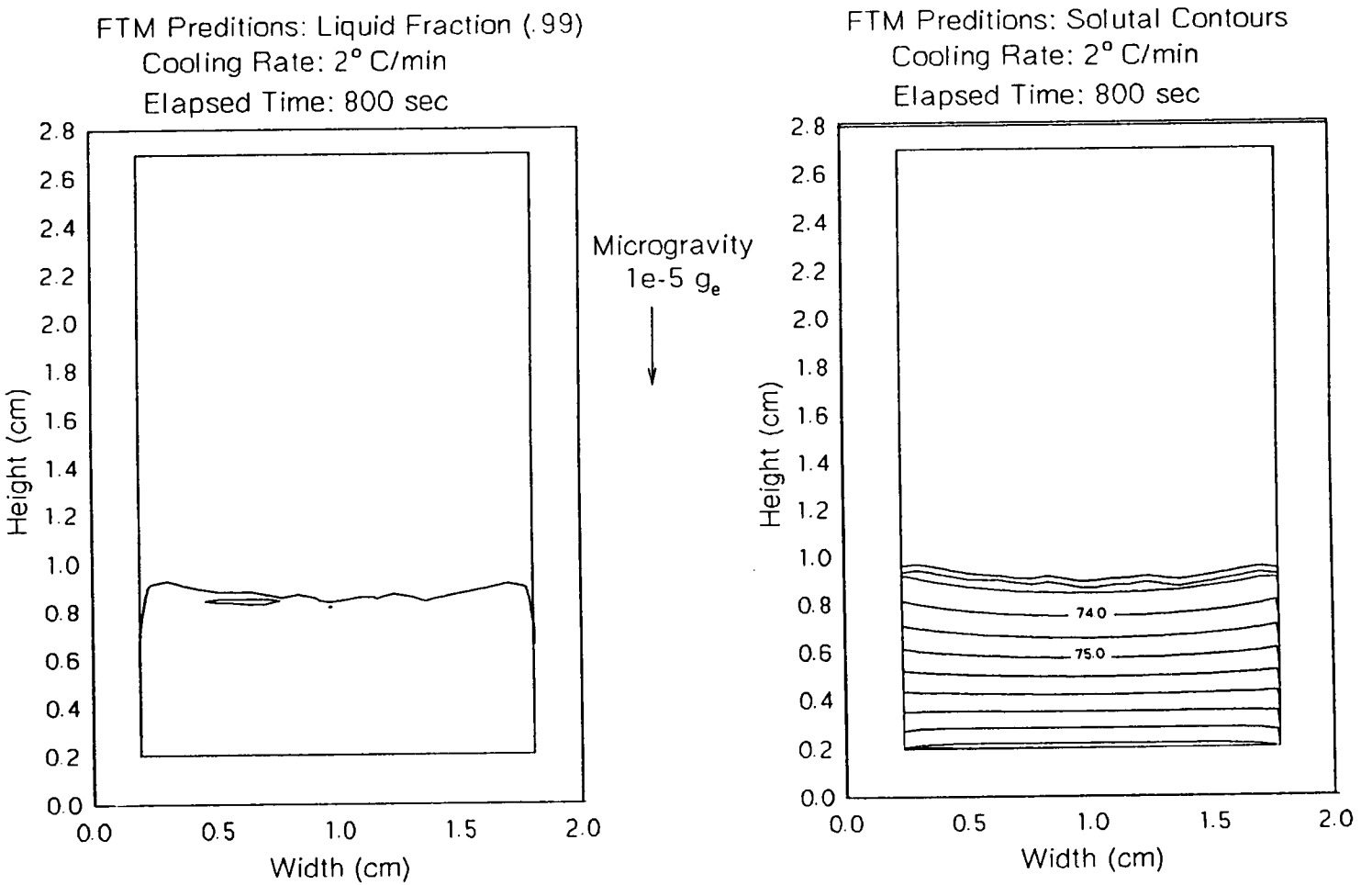

Figure V–9. Microgravity predictions: 2°C/min cooling rate: Elapsed time = 800 sec: (a) Liquid fraction contours (b) Solutal contours

solidification front to establish a steady growth rate. This is in sharp contrast with the convective breakdown and vigorous convection observed in the ground laboratory.

The model predicts the influence of convection in microgravity to be minimal, but nonzero. For the given cooling rate and boundary conditions, the convection that does exist is primarily due to contraction flows on the order of 1×10^{-5} cm/sec. The buoyancy driven flows are secondary at approximately 1×10^{-7} cm/sec. When compared with the 1.19×10^{-3} cm/sec translation rate of the solidification front, these buoyancy driven flows are negligible. However, for either slower growth rates or an unfavorably aligned body force vector, the relative influence of natural convection, even in microgravity, might be significant. Thus, the absence of convective effects in microgravity cannot be assumed, but must be evaluated for each different set of boundary conditions. For the current case, however, the FTM results confirm that the conditions of the experiment meet the CAST objectives to study directional solidification with negligible convective influence. This confirmation is based on very specific predictions for the development of the thermal, solutal, and velocity fields, and the extent of solidification. The detailed verification of these results awaits flight data.

SECTION VI

CONCLUSIONS

A two-dimensional computational fluids model was developed for the express purpose of supporting experimental research on the directional solidification of a dendritic binary material in microgravity. The model required the extension of existing control volume techniques to include the presence of a solidifying two-phase mushy zone. A single set of continuum two-phase conservation equations for mass, momentum, species, and energy, coupled with the physical properties of the materials, was applied over the experimental domain, including both the test solution and its quartz container. This reduced the empirical inputs required in the model to a set of nucleation criteria, an external heat loss coefficient, and a Darcy coefficient to account for flow resistance in the two phase region. All phenomena internal to the domain, such as the position of the growth front, fraction of solid, temperature, concentration, and velocity were then computed as a function of the specific transient boundary conditions corresponding to a given run.

The model avoided simplification of the governing equations in order to maintain fidelity and generality. As such, the body force terms were retained in the momentum equations despite the weak influence of this term in microgravity. Similarly, the density was treated rigorously, allowing for the calculation of contraction flows which are traditionally neglected. Most significantly, the numerical control volumes were not constrained to be in equilibrium. The liquid in a local control volume was allowed to undercool, depending on the nucleation criteria. This later feature was found essential for the accurate simulation of the solidification process. The general capabilities of the model enabled it to be used in support of ground-based studies as well as the microgravity research.

A set of model predictions for a ground-based run correlated favorably with the ground-based data during the early diffusion dominated stages of solidification, i.e., before convective effects became dominant. Using an effective heat loss coefficient based on interferometer data from the initial steady state run conditions and an estimate of the nucleation parameters and Darcy coefficient, the model predicted the growth of the mushy zone; the development of the solutal, thermal, and density fields ahead of the growth front; the time of the transition to convective domination, i.e., convective stability; and the qualitative flow pattern preceding the transition for a sample ground-based run. Since microgravity solidification is inherently diffusion dominated, the success of the ground-based predictions was taken as verification of the model's capability to provide microgravity predictions.

The model was then used to calculate a representative microgravity experiment in support of pre-flight preparation. The results for the given case confirmed the buoyancy driven flows in microgravity to be subordinate to contraction flows which, in turn, were shown to be small relative to the growth rate of the mushy zone and the transport of energy and solute during solidification. Without the transition to vigorous convection encountered in the one-gravity environment, the solutal and thermal fields developed smoothly over the duration of the simulated experiment and the mushy zone growth achieved an approximately steady growth velocity within the time frame of the run. A secondary effect of the microgravity environment was shown to be the reduction of the initial mushy zone height due to the reduced convective cooling on the exterior of the test cell. In general, the model verified that for the representative run parameters, the test objective of investigating dendritic directional solidification with minimal convection will be achieved, as long as initial conditions are adjusted to allow for increased preparation time and reduced heat loss to the ambient.

In modeling the ground-based experiment and providing a prediction for the microgravity experiment, the FTM demonstrated the usefulness and validity of applying the numerical control volume conservation technique to a solidifying dendritic system and a number of conclusions can be drawn. One is that the inclusion of the solution container, in this case the quartz cuvette, is necessary for the correct simulation of the temperature field in such a system. In the ground-based simulation, the presence of the quartz sidewalls was shown to be the primary driver for the initial convective flows. In addition, the inclusion of non-equilibrium effects is critical in the model in order to realistically model the growth of the two-phase region and the corresponding effect on the solutal, thermal, and velocity fields. In microgravity the effects of low levels of convection due to either natural convection or contraction flow, while negligible for the current run parameters, were concluded to be potentially significant for other cooling rates or boundary conditions and must also be included for the accurate simulation of microgravity solidification. For the ground-based simulations, the incorporation of the non-equilibrium effects provided good correlation with the experimental results during diffusion dominated growth, predicting the perturbation mechanism and approximate onset time for convective breakdown. As such, the model could be used to do sensitivity studies on the effect of various parameters such as cooling rate and mushy zone resistance on direction solidification and convective breakdown. By changing the properties, the FTM could be used to model other materials as well. In addition, the convection dominated solidification growth stage could be modeled by including a turbulence model and extending the FTM to three dimensions.

While these and other improvements in the FTM are possible, they are secondary to the primary purpose of the model, support of basic research on the diffusion dominated directional solidification of a dendritic binary material, as

planned for the CAST microgravity experiment. Once available, data from the CAST experiments will be compared with the quantitative predictions of the model and used to refine the physical models. The thermocouple and index of refraction data will be used to dictate the correct effective external heat loss coefficient. The position of the growth front relative to the liquidus will reveal the degree of undercooling ahead of the mushy zone and allow for refinement of the nucleation criteria. These criteria are seen as the weak link in the extrapolation to microgravity since they are difficult to verify in the one-gravity environment due to the limited growth of the mushy zone prior to the dominant effects of convection. Perhaps the greatest contribution of the flight data will be unanticipated results and deviations from the model predictions, revealing the significance of phenomena normally overlooked in one gravity, thus leading to both improved modeling capabilities and a more fundamental understanding of the solidification process as it occurs in the earth and orbiting laboratory.

REFERENCES

REFERENCES

1. Open Session Proceedings of the XXII ICHMT International Symposium on Manufacturing and Materials Processing, Dubrovnik, Yugoslavia, August 27-31, 1990 (in press).

2. McCay, T.D. and McCay, M.H., "Measurements of Solutal and Thermal Layers in Unidirectional Solidification," *AIAA-87-1494*, AIAA 22th Thermophysics Conference, Honolulu, Hawaii, June 8-10, 1987.

3. McCay, T.D., McCay, M.H., Lowry, S.A., and Smith, L.M., "Convective Effects on Directional Solidification of a Simulated Metal Alloy," *AIAA-88-0258*, AIAA 26th Aerospace Sciences Meeting, Reno, Nevada, January 11-14, 1988.

4. Gray, P.A., "Experimental Study of Convective Breakdown in Solidification of a Metal Model Material," M.S. Thesis, The University of Tennessee, Knoxville, TN, May 1989.

5. McCay, T.D., McCay, M.H., and Gray, P.A., "Experimental Observations of Convective Breakdown During Directional Solidification," *Physical Review Letters,* Vol. 62, No. 17, pp. 2060-2063, April 1989.

6. McCay, T.D., McCay, M.H., Lowry, S.A., Smith, L.M., and Henderson, A.H., "Measurements of Diffusion Limited Solidification at Varying Gravity," *AIAA-89-1755*, AIAA 24th Thermophysics Conference, Buffalo, New York, June 12-14, 1989.

7. McCay, T.D., McCay, M.H., Lowry, S.A., and Smith, L.M., "Convective Instabilities During Directional Solidification," *Journal of Thermophysics and Heat Transfer,* Vol. 3, No. 3, pp. 345-350, July 1989.

8. Hopkins, J.A., "Experimental Study of Convective Instability of the Diffusion Layer Produced During Directional Solidification of a Metal Model Material," M.S. Thesis, The University of Tennessee, Knoxville, TN, December 1988.

9. Hopkins, J.A., McCay M.H., Smith, L.M., and McCay, T.D., "Optical Methods for Study of Mass Transfer During Metal Model Directional Solidification," Proceedings of the XXII ICHMT International Symposium on Manufacturing and Materials Processing, Dubrovnik, Yugoslavia, August 27-31, 1990 (in press).

10. Flemings, M.C., *Solidification Processing*, McGraw Hill, 1974.

11. Jackson, K.A. and Hunt, J.D., "Transparent Compounds That Freeze Like Metals," *Acta Metallurgica*, Vol. 13, pp. 1212-1215, 1965.

12. Kurtz, W. and Fisher, D.J., *Fundamentals of Solidification*, Trans Tech Publications, Aedermannsdorf, Switzerland, 1989.

13. Tiller, W.A., Jackson, K.A., Rutter, J.W., and Chalmers, B., "The Redistribution of Solute Atoms During the Solidification of Metals," *Acta Met.,* Vol. 1, pp. 428-437, 1953.

14. Mullins, W.W. and Sekerka, R.F., *J. App. Physics*, Vol. 35, p. 444, 1964.

15. Jackson and Hunt, "Transparent Compounds That Freeze Like Metals," *Acta Metallurgical*, Vol. 13., pp. 1212-1215, 1965.

16. Jackson, K.A., Hunt, J.D., Uhlmann, and Seward III, T.P., "On the Origin of the Equiaxed Zone in Castings," *Trans. TMS-AIME,* Vol. 236, pp. 149-158, 1966.

17. McCay, M.H. and McCay, T.D., "Experimental Measurements of Solutal Layers in Unidirectional Solidification," *Journal of Thermophysics and Heat Transfer*, Vol. 2, No. 3, pp. 197-202, 1980.

18. Stewart, M.J. and Weinberg, F.J., "Fluid Flow in Liquid Metals," *Journal of Crystal Growth,* Vol. 12, pp. 217-227, 1972.

19. Lowry, S.A., M.H. McCay, T.D. McCay, and Gray, P.A.,"Surface Tension Measurements of Aqueous Ammonium Chloride in Air," *Journal of Crystal Growth,* Vol. 96, 1989.

20. Johnston, M.H. and Owen, R.B., "Optical Observations of Unidirectional Solidification in Microgravity," *Metallurgical Transactions*, Vol. 14A, pp. 2163-2167, 1983.

21. Copley, S.M., Giamei, A.F., Johnson, S.M., and Hornbecker, M.F., "The Origin of Freckles in Unidirectionally Solidified Castings," *Metallurgical Transactions*, Vol. 1, pp. 2193-2204, 1970.

22. Glicksman, M.E., Winsa, E., Hahn, R.C., Lograsso, T.A., Tirmizi, S., and Selleck, M.E., Dendritic Solidification Under Microgravity Conditions," *AIAA-88-0248*, 26th Aerospace Science Meeting, AIAA, Reno, Nevada, January11-14, 1988.

23. Johnston, M.H. and Griner, C.S., "Compositional Variations in the Undercooled Pb-Sn Eutectic Solidified at Various Acceleration Levels," *Scripta Met.*, Vol. 2, pp. 253-255, 1977.

24. McDonald, R.J. and Hunt, J.D., "Fluid Motion Through the Partially Solid Regions of a Casting and Its Importance in Understanding A Type Segregation," *TMS-AIME*, Vol. 245, pp. 1993-1997, September 1969.

25. McDonald, R.J. and Hunt, J.D., "Convective Fluid Motion within Interdendritic Liquid of Casting," *Metall. Trans.*, Vol. 1, pp. 1787-1788, 1970.

26. Johnston, M.H., Griner, C.S., Parr, R.A., and Robertson, S.J., "The Direct Observation of Unidirectional Solidification as a Function of Gravity Level," *Journal of Crystal Growth*, Vol. 50, p. 831, 1980.

27. Ostrach, S., "Fluid Mechanics in Crystal Growth - The 1982 Freeman Scholar Lecture, " *J. Fluids Engineering.,* Vol. 105, pp. 5-20, 1983.

28. Pimputkar, S.M. and Ostrach, S., "Convective Effects in Crystal Grown from Melt," *J. Crystal Growth*, Vol. 55, pp. 614-646, 1981.

29. Fu, B.I. and Ostrach, S., "The Effects of Stabilizing Thermal Gradients on Natural Convection Flows in a Square Enclosure," *Natural Convection* , Catton, I. and Smith, R.N., Eds., ASME, HTD-Vol. 16, pp. 91-104

30. Stern, M.E., "The Salt-Fountain and Thermohaline Convection," *Tellus X*, pp. 172-175, 1960.

31. Linden, P.F., *Convective Transport and Instability Phenomena*, Zierep, J. and Oertel, H., Jr., Eds., Brann Pub., Karlsruhe, pp. 171-197, 1982.

32. Thorpe, S.A., Hutt, P.K., and Soulsby, R., "The Effects of Horizontal Gradients on Thermohaline Convection," *J. Fluid Mechanics*, Vol. 38, Part 2, pp. 375-400, 1969.

33. Chen, C.F., "Onset of Cellular Convection in a Salinity Gradient Due to Lateral Temperature Gradients," *Journal of Fluid Mechanics*, Vol. 63, pp. 563-576, 1974.

34. Chen, C.F., Briggs, D.G., and Wirtz, R.A., "Stability of Thermal Convection in a Salinity Gradient Due to Lateral Heating," *Int. J. Heat Mass Transfer*, Vol. 14, pp. 57-65, 1971.

35. Asai, S. and Muchi, I., "Theoretical Analysis and Model Experiments on Formation Mechanism of Channel-Type Segregation," *Trans. Iron Steel Institute of Japan*, Vol. 18, pp. 90-98, 1978.

36. Mehrabian, R., Keane, M.A., and Flemings, M.C., "Experiments on Macrosegregation and Freckle Formation," *Metalurgical Transactions*, Vol. 1, pp. 3238-3241, 1970.

37. Stewart, M.J. and Weinberg, F., "Fluid Flow Through a Solid-Liquid Interface," *Metallurgical Transactions*, Vol. 3, pp. 333-337, 1972.

38. Szekely, J. and Jassal, A.S., "An Experimental and Analytical Study of the Solidification of a Binary Dendritic System," *Metallurgical Transactions B*, Vol. 9B, pp. 389-398, September 1978.

39. Christenson, M.S. and Incropera, F.P., "Solidification of Aqueous Ammonium Chloride Solution in a Rectangular Cavity - I. Experimental Study," *Int. J. Heat Mass Transfer.*, Vol. 32, No. 1, pp. 47-68, 1989.

40. Beckermann, C. and Viskanta, R., "Double Diffusive Convection During Dendritic Solidification of a Binary Mixture," *Physico-Chemical Hydrodynamics*, Vol. 10, pp. 195-213, 1988.

41. Caldwell, T.W., Campagna, A.J., Flemings, M.C., and Mehrabian, R., "Refinement of Dendrite Arm Spacing in Aluminum Ingots Through Heat Flow Control," *Metallurgical Transactions B*, Vol. 8B, pp. 261-270, 1977.

42. Bower, T.F. Brody, H.D. and M.C. Flemings, "Measurement of Solute Redistribution in Dendritic Solidification," *Trans. AIME*, Vol. 236, pp. 624-634, 1966.

43. Flemings, M.C. and Nereo, G.E., "Macrosegregation: Part III," *Trans TMS-AIME*, Vol. 242, pp. 50-55, 1968.

44. Verhoven, J.D., Mason, J.T., and Trivedi, R., "The Effect of Convection on the Dendrite to Eutectic Transition," *Metallurgical Transactions A*, Vol. 17A, pp. 991-1000, 1986.

45. Streat, N. and Weinberg, F., "Macrosegregation During Solidification Resulting from Density Differences in the Liquid," *Metallurgical Transactions A*, Vol. 5, pp. 2539-2548, 1974.

46. Sample, A. and Hellawell, A., "The Mechanism of Formation and Prevention of Channel Segregation during Alloy Solidification," *Metallurgical Transactions A*, Vol. 15A, pp. 2163-2173, 1984.

47. Sarazin, J.R. and Hellawell, A., "Channel Formation in Pb-Sn, Pb-Sb, and Pb-Sn-Sb Ingots and Comparison with the System NH_4Cl-H_2O," *Metallurgical Transactions,* Vol. 19A, pp. 1861-1871, 1988.

48. "Casting and Solidification Technology, Fluid Experiment System, International Microgravity Lab-I," Rudy Ruff, Technical Monitor. Marshall Space Flight Center, NASA, Huntsville, AL.

49. Tien, R.H. and Gieger, G.E., "A Heat-Transfer Analysis of the Solidification of a Binary Eutectic System," *J. Heat Transfer*, pp. 231-234, August 1967.

50. Cho, S.H. and Sunderland, J.E., "Heat-Conduction Problems with Melting or Freezing," *J. of Heat Transfer*, pp. 421-426, August 1969.

51. Lipton, J., Garcia, A., and Heinemann, W., "An Analytical Solution of Directional Solidification with Mushy Zone," *Arch. Eisenhuttenwes*, Vol. 53, No. 12, pp. 469-473, 1982.

52. Brody, H.D. and Flemings, M.C., "Solute Redistribution in Dendritic Solidification," *Trans AIME*, Vol. 236, pp. 615-624, 1966.

53. Flemings, M.C. and Nereo, G.E., "Macrosegregation: Part I," *Trans. TMS-AIME*, Vol. 239, pp. 1449-1461, 1967.

54. Flemings, M.C., Mehrabian, R., and Nereo, G.E., "Macrosegregation: Part II," *Trans. TMS-AIME*, Vol. 242, pp. 41-59, 1968.

55. Mehrabian, R., Keane, M., and Flemings, M.C., "Interdendritic Fluid Flow and Macrosegregation; Influence of Gravity," *Metall. Trans.*, Vol. 1, pp. 1209-1220, 1970.

56. Fujii, T., Poirier, D.R., and Flemings, M.C., "Macrosegregation in a Multicomponent Low Alloy Steel," *Metallurgical Transactions B*, Vol. 10B, pp. 331-339, December 1979.

57. Coriell, S.F., Cordes, M.P., Boettinger, W.J., and Serkerka, R.F., "Convective and Interfacial Instabilities During Unidirectional Solidification of a Binary Alloy," *Journal of Crystal Growth*, Vol. 49, pp. 13-28, 1980.

58. McFadden, G.B., Rehm, R.G., Coriell, S.R., Chuck, W., and Morrish, K.A., "Thermosolutal Convection During Directional Solidification," *Metallurgical Transactions A*, Vol. 15, pp. 2125-2137, 1984.

59. McFadden, G.B. and Coriell, S.R., "Thermosolutal Convection During Directional Solidification. II. Flow Transitions," *Physics of Fluids*, Vol. 30, pp. 659-671, 1987.

60. Heinrich, J.C., "Numerical Simulation of Thermosolutal Instability During Directional Solidification of a Binary Alloy," *Computer Methods and Engineering*, Vol. 69, pp. 65-88, 1988.

61. Nandepunkar, P., Poirier, D.P., Heinrich, J.C., and Felicelli, S., "Thermosolutal Convection During Dendritic Solidification of Alloys, Part 1. Linear Stability Analysis, " *Metallurgical Transactions B*, Vol. 20, pp. 711-721, 1989.

62. Heinrich, J.C., Felicelli, S., Nandapurkar, P., and Poirier, D.R., "Thermosolutal Convection During Dendritic Solidification of Alloys: Part II. Nonlinear Convection," *Metallurgical Transactions B*, Vol. 20B, pp. 883-890, December 1989.

63. Voller, V.R. and Prakash, C., "A Fixed Grid Numerical Modeling Methodology for Convection-Diffusion Mushy Region Phase-Change Problems," *Int. J. Heat Mass Transfer.*, Vol. 30, No. 8, pp. 1709-1719, 1987.

64. Beckermann, C. and Ni J., "Micro-Macroscopic Modeling of Transport Phenomena During Solidification," Proceedings of the XXII ICHMT International Symposium on Manufacturing and Materials Processing, Dubrovnik, Yugoslavia, August 27-31, 1990 (in press).

65. Voller, V.R., Brent, A.D., and Prakash, C., "The Modeling of Heat, Mass and Solute Transfer," *Int. J. Heat and Mass Transfer,* Vol. 32, pp. 1719-1931, 1989.

66. Bennon, W.D. and Incropera, F.P., "A Continuum Model for Momentum, Heat and Species Transport in Binary Solid-Liquid Phase Change Systems - I. Model Formulation," *Int. J. Heat Mass Transfer.*, Vol. 30, No. 10, pp. 2161-2170, 1987.

67. Bennon, W.D. and Incropera, F.P., "A Continuum Model for Momentum, Heat and Species Transport in Binary Solid-Liquid Phase Change Systems - II. Application to Solidification in a Rectangular Cavity," *Int. J. Heat Mass Transfer.*, Vol. 30, No. 10, pp. 2171-2187, 1987.

68. Christenson, M.S. and Incropera, F.P., "Solidification of aqueous ammonium chloride Solution in a Rectangular Cavity - II. Comparison of Predicted and Measured Results," *Int. J. Heat Mass Transfer.*, Vol. 32, No. 1, pp. 47-68, 1989.

69. Incropera, F.P., Bennon, W.D., Christenson, M.S., Neilson, D.G., and Prescott, P.J., "Solidification of Binary Liquids: Physical Phenomena and Consequences," Proceedings of the XXII ICHMT International Symposium on Manufacturing and Materials Processing, Dubrovnik, Yugoslavia, August 27-31, 1990 (in press).

70. S.V. Patankar, *Numerical Heat Transfer and Fluid Flow,* Hemisphere Publishing Company, 1980.

71. Van Doormaal, J.P. and Raithby, G.D., "Enhancement of the SIMPLE Method for Predicting Incompressible Fluid Flows," *Numerical Heat Transfer*, Vol. 7, pp. 147-163, 1984.

72. Hopkins, J.A., "CAST Notes: Undercooling of NH_4Cl-H_2O," Internal note, University of Tennessee Space Institute, November 30, 1989.

73. CRC, Handbook of Chemistry and Physics, 64th Ed., 1984.

74. American Institute of Physics Handbook, 3rd Ed., McGraw-Hill Book Company, New York, 1964.

75. International Critical Tables of Numerical Data, NRC, McGraw-Hill Book Company, New York, 1926.

76. *JANAF Thermo Tables,* National Standard Reference Data Service-National Bureau of Standards, June 1971.

77. Inaba, H. and Fukuda, T. "Natural Convection in an Inclined Square Cavity in Regions of Density Inversion of Water," *J. Fluid Mech.*, Vol. 142, pp. 363-381, 1984.

78. Lin, D.S. and Nansteel, M.W. "Natural Convection Heat Transfer in a Square Enclosure Containing Water Near Its Density Maximum," *Int. J. Heat Mass Transfer,* Vol. 30., No. 11, pp. 2319-2329, 1987.

79. Kreith, F. and Bohn, M.S. *Principles of Heat Transfer,* Harper and Row Publishers, New York, 1986.

VITA

Samuel A. Lowry was born in South Weymouth, Massachusetts, on September 17, 1952. He subsequently moved to and grew up in Cincinnati, Ohio, attending high school at The Cincinnati Country Day School and graduating in June 1971. He attended Harvard College in Cambridge, Massachusetts from the Fall of 1971 to the Spring of 1975 and earned an A.B. degree in Engineering and Applied Physics. Following college, he served on active duty as a Lieutenant in the United States Marine Corps until April 1978 after which he attended Case Western Reserve University in Cleveland, Ohio, receiving an Master of Science degree in Mechanical Engineering in the Fall of 1980. He subsequently worked on a year's grant in the Crystal Growth Branch in the Space Science Laboratory at the Marshall Space Flight Center in Huntsville, Alabama, and then worked as a NASA engineer in the Structures and Propulsion Laboratory at the Marshall Space Flight Center from September 1981 to September 1986. In the Fall of 1986 he returned to school at the University of Tennessee Space Institute in Tullahoma, Tennessee. While at the University of Tennessee he married Katherine Pella and their son, Matthew, was born on August 20, 1989. He received his Doctor of Philosophy in Engineering Science in May 1991.